Title
Thermal Transport and Light Transmission in Anisotropic Nano/Micro-Grained Materials for High Power Laser Applications

Permalink
https://escholarship.org/uc/item/4x68063t

Author
Mishra, Vivek

Publication Date
2017

Peer reviewed|Thesis/dissertation

Thermal Transport and Light Transmission in Anisotropic Nano/Micro-Grained Materials
for High Power Laser Applications

By

Vivek Mishra

A dissertation submitted in partial satisfaction of the

requirements for the degree of

Doctor of Philosophy

in

Engineering − Mechanical Engineering

in the

Graduate Division

of the

University of California, Berkeley

Committee in charge:

Professor Christopher Dames, Chair
Professor Costas Grigoropoulos
Professor Phillip Geissler

Fall 2017

Thermal Transport and Light Transmission in Anisotropic Nano/Micro-Grained Materials
for High Power Laser Applications

©2017

by

Vivek Mishra

Abstract

Thermal Transport and Light Transmission in Anisotropic Nano/Micro-Grained Materials
for High Power Laser Applications

by

Vivek Mishra

Doctor of Philosophy in Engineering – Mechanical Engineering

University of California, Berkeley

Professor Christopher Dames, Chair

Rare earth (RE)-doped solid state lasers have helped push the boundaries of high power lasers. Since lasing was first demonstrated in polycrystalline ceramic lasers, the possibility to dope higher concentrations of RE elements using non-equilibrium processes has enabled larger laser slope efficiencies. The limits in power densities in high power lasers are often due to thermal rollover caused by losses due to thermal lensing and depolarization effects, while catastrophic failures can be caused by thermal stress fracture. In such systems, a higher thermal conductivity of the lasing media lowers the thermal gradients in the lasing media, thus allowing higher lasing powers. Ceramics with twice the thermal conductivity of state of the art Nd:YAG lasers have been developed to work towards this goal, while recently visible photoluminescence was demonstrated in a Tb:AlN ceramic.

In the above polycrystalline ceramics, additional scattering caused by reflection of the heat carrying phonons at the grain boundaries can lead to a thermal conductivity which is smaller than that for single crystals by more than an order of magnitude. The mean free path of phonons in this boundary scattering regime is typically directly proportional to the grain sizes. On the other hand, the slight anisotropy of the unit cell of AlN leads to the birefringence effect. Light propagating through grains with misaligned orientation see a slightly different refractive index ($\Delta\eta_{max} \sim 0.05$ for red light). For small birefringence and grain sizes, when the Rayleigh-Gans-Debye approximation holds, the extinction coefficient of light due to scattering decreases with decreasing grain sizes. Thus, light transmission and thermal conductivity of these sintered ceramics scale oppositely with increasing grain sizes.

This thesis is divided into three parts. First, we investigate the effect of anisotropic grains on light transmission and thermal conductivity for active ion doped AlN and Al_2O_3 ceramics. Models to predict the transport properties are developed and verified, following which we use material properties from literature to predict the expected properties as a function of grain sizes and anisotropy. A figure of merit is proposed which can be used to select the microstructure that helps maximize the lasing power.

The anisotropic microstructure of the materials is expected to result in anisotropic transport properties of the bulk material. To measure the anisotropic thermal conductivity tensor of such materials, we developed a technique based on the electrothermal 3ω method. This method had been previously been used to measure the thermal conductivity

of materials with the principal thermal conductivity directions aligned along the obvious surfaces of the sample. In this work, we found the solution for the general case where the principle axes may be aligned in any arbitrary direction. This method was verified against numerical FEM simulations and were demonstrated with experiments on a naturally occurring anisotropic mineral, mica.

Finally, we developed easily accessible and cheap methods to measure the light scattering properties of thin scatterers. Three different methods were developed. Two of the approaches require the use of an USAF 1951 target to measure the modulation transfer function, MTF. Here, the MTF of the image is obtained with the sample of interest and the USAF target placed in between the image plane and the light source. The third method uses the edge spread function following very similar ideas as the MTF method. Two of the methods use a collimated light source while one of the MTF methods uses a diffuse light source. We show experimental demonstration of the methods involving collimated light sources while numerical ray tracing is used to verify the method involving a diffuse light source.

Table of Contents

List of Figures

List of Tables

Acknowledgements

First and foremost, I would like to thank my advisor, Professor Chris Dames, whose constant support created an ideal environment in which to pursue my intellectual development. Chris' persistence for completeness, attention to detail, vast experience, thirst for new knowledge, and dedication to his students has been extremely inspiring. He has been an ideal role model over the last five years. My gratitude also extends to my collaborator, Professor Javier Garay, who was a constant source of disruptive high potential ideas. It was a pleasure planning out the future of my research with him and Chris.

I am grateful to my colleagues, Zhen Chen, Fan (Peter) Yang, Sean Lubner, Imran Khan, Wyatt Hodges, Geoff Wehmeyer, Jake Kilbane, Andrea Pickel, Christian Monachon, Josh Wilber, Menglong Hao, and Jason Wu for sharing several helpful discussions during grad school. In particular, I would especially like to thank Peter for showing me the ropes to help me transition from being a mathematical modeling guy to a hands-on experimentalist, and Christian for helping me start up on optical experiments. Special thanks to Jake and Andrea for feeding and supporting my climbing needs over the last three years.

I would like to thank my friends Somil Bansal, Spencer Frank, Abdulrahman Jbaily, David Fernández-Gutiérrez, Raj Shekhar Singh, Claire Funke, Rachael Hager, Rishi Ganeriwala, Maribel Jaquez, Andreas Hansen, Dusan Coso, Korok Chatterjee, Prashanth Selvaraj and Chris Warner for keeping me entertained over the years spent at Berkeley. I will cherish the memories of five years of playing intramural soccer, outdoor adventures and the moments I shared with them all.

Finally, I would like to thank my family for unfailing support and guidance along my academic path. My mother, Madhusmita Mishra, who was the first from my extended family to have a Ph.D., has constantly inspired me to strive for more knowledge. My father, Pradip Kumar Mishra, for instilling in me the belief that understanding the subject and the methodology is more crucial than the result itself. My brother, Varun, my perennial study and sports partner, has been instrumental in getting me to where I am. I will forever be grateful to them.

Chapter 1 - Introduction

Their compactness, efficiency, reliability and often low cost have made diode pumped solid state (DPSS) lasers prevalent in high power density applications.[1,2] In DPSS lasers, typically transparent crystalline or amorphous glass-like materials doped with active ions are used as the laser gain media. Often the lasing medium size and dopant density in the case of crystalline hosts are limited by the synthesis method and the solubility of dopants.[3] For example, the doping density in single crystal Nd:YAG lasers is typically restricted to ~1at%. More recently, polycrystalline ceramic lasing media have helped push the lasing powers up by allowing faster synthesis of large active lasing media with a higher density of active dopants.[4]

However, the power scaling in such lasers becomes challenging because of the large heat generation within the active medium due to the inherent quantum defect of the lasing process. Unlike gas lasers, where convection by the gas flow can enhance heat dissipation ability, heat dissipation within the active medium in DPSS lasers is limited to conduction only. With inadequate heat dissipation, large thermal gradients can cause losses due to thermal lensing and depolarization effects, while thermal stress can cause catastrophic thermal stress fracture. Various methods have been used to maximize heat dissipation, which can be roughly divided into 3 broad groups:

i. Implementing new lasing geometry design such as thin slab lasers[5–7] with orthogonal pumping and heat dissipation/cooling directions.
ii. Using novel high thermal conductivity (k) host materials such as sesquioxides,[7] which offer a 50% increase in thermal conductivity compared to Nd:YAG lasers.
iii. By host material microstructure design.[8] Lasing has been demonstrated in polycrystalline anisotropic/birefringent ceramics by increasing orientation control of grains.

In Chapter 2, we take advantage of all of the above approaches to design high power lasing media made of polycrystalline ceramics. The ability to orient the grains in polycrystalline ceramics[8,9] allows for excellent light transmission in ceramics made of birefringent materials, which paves the way for higher thermal conductivity large bandgap materials such as Al_2O_3[10] and AlN[11] to be considered as host material candidates. Visible photoluminescence and lasing has already been demonstrated in rare earth and transition metal doped AlN[12–14] and Al_2O_3[15–17] ceramics and single crystals.

In polycrystalline ceramics, an additional challenge arises due to the opposite scaling laws obeyed by the desirable thermal conductivity and light transmissivity of the birefringent polycrystalline materials as a function of the characteristic grain size. The grain boundaries within the polycrystals scatter the heat carrying phonons, which can result in an order of magnitude decrease[18,19] in thermal conductivity with decreasing grain size. On the other hand, for high light transmission, the scattering of light at the grain boundaries needs to be minimized. For the small sub-10μm grain sizes that are typical in polycrystalline ceramics synthesized by the highly non-equilibrium spark plasma sintering process, the light transmission has been shown to increase with decreasing grain sizes.[20] Thus, the grain size has opposite effects on the heat

dissipation ability (thermal conductivity) and beam quality (light transmission) for transport through polycrystalline birefringent material.

The above challenge can be tackled by synthesizing ceramics with anisotropic properties that exploit the possibility to decouple the lasing direction from the cooling direction. In such an arrangement, it is essential to have good thermal transport primarily in the cooling direction, while excellent light transmission is required in the lasing and pumping direction. This is schematically shown in Figure 1-1 for a slab laser configuration.
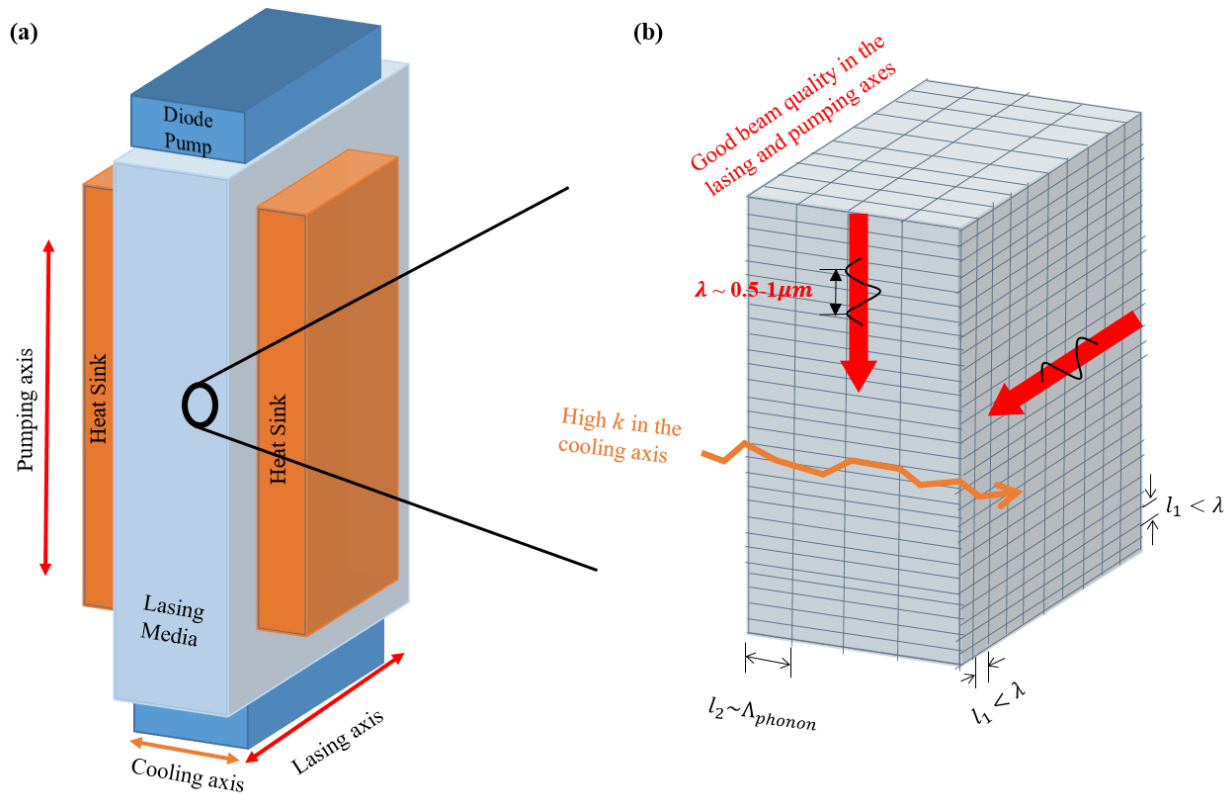
Figure 1-1 (a) Schematic of a side-pumped slab laser with orthogonal lasing and cooling directions. (b) An anisotropic microstructure where grain sizes along the lasing/pumping directions are small while that in the cooling direction are large can help achieve high lasing powers.

As shown in Figure 1-1(b), we expect that it is possible to achieve higher laser power densities if the grain sizes in the direction of thermal transport, l_2, are close to the intrinsic mean free paths for phonons, Λ_{phonon}, while the other 2 dimensions, l_1 are similar or smaller than the wavelength of transmitting light. We verify this assumption by utilizing multiple modeling techniques in the second chapter of this thesis. A figure of merit is introduced, which was optimized to find the best combination of grain sizes and shapes, and directions for thermal and light power transport.

In Chapters 3 and 4 of the thesis, we develop methods to measure both thermal transport and light transmission properties of anisotropic ceramics. We first talk about thermal conductivity measurement. With the general assumption that the crystallographic orientation is unknown, the complete thermal conductivity tensor can be described by

$$\overset{=}{k} = \begin{bmatrix} k_{xx} & k_{xy} & k_{xz} \\ k_{yx} & k_{yy} & k_{yz} \\ k_{zx} & k_{zy} & k_{zz} \end{bmatrix},$$

(1-1)

where $\overset{=}{k}$ has 6 independent elements since $k_{ij} = k_{ji}$ from Onsager's reciprocity relations.[21] The typically nickel-sized samples are only ~1 mm thick[12] and are expected to have thermal conductivities up to 100 W/m·K, which makes traditional steady state techniques unsuitable for measuring the thermal conductivity tensor. To measure the thermal conductivity of thin isotropic materials, periodic heating techniques have been used to bound the heat spreading within a frequency dependent thermal penetration depth.[22–24] This also reduces unwanted parasitic losses due to convection and radiation to less than a percent of the total heat spreading.[22] Recently, a laser based technique, time-domain thermoreflectance (TDTR) was used to measure an arbitrarily aligned thermal conductivity tensor.[25] The necessity to use specialized ultrafast lasers and time-consuming iterative process, make the above measurement method challenging and expensive.

Instead, in this work, we developed solutions for the electrothermal-based 3ω method, where an alternating current source creates a fluctuating temperature field in the substrate due to Joule heating. This temperature fluctuation can be inferred from the change in resistance of the heater, and is a function of the thermal conductivity of the substrate. While there have been previous attempts to measure the thermal conductivity of anisotropic materials with the principal conductivities aligned along the sample's orthogonal surfaces,[26–28] they lack a closed form solution and do not consider the case of arbitrary principal axes orientation. In Chapter 3, we developed solutions for the 3ω problem on a substrate with an arbitrary anisotropy. Following this, the method was demonstrated with experiments on mica, which was machined in an off-axis direction to create off-diagonal elements of the *k*-tensor.

Finally, in Chapter 4, we develop cheap, easily accessible and high throughput methods to measure the light transmission properties of thin samples. For non-absorbing material, the exclusive source of light attenuation is by elastic scattering of light. The light scattering property of a material is defined using two terms: (i) the scattering coefficient, β_{sca}, and (ii) the angle dependent scattering phase function, $\Phi(\theta_i, \theta_s)$, where Φ is a function of the incident and the scattered angles, θ_i and θ_s respectively. The typical methods for characterizing the above properties include the use of specialized and possibly expensive optical equipment such as a laser source, integrating sphere, and high precision goniometer.[20,29]

The methods developed in this work require inexpensive optical elements such as LEDs or light tables, simple scientific cameras, and resolution targets. The methods use either a collimated or a diffuse light source, where the light scattering properties can be inferred from comparing the blurriness of an imaged target with and without the presence of the sample-of-interest in the imaging path. These methods are sensitive to the light scattering properties over a large area of the sample (~10 mm^2), and thus is a non-local measurement unlike laser-based technique. For each method, as a first step, we first calculate the point spread function as a function of the light scattering parameters and geometry, following which the methods are validated by experiments with a surface scatterer and numerical simulations with ray tracing software.

1.1 Organization of the Dissertation

This thesis is divided into 3 big topics:

Chapter 2 - Optimizing Thermal Transport and Light Transmission in Anisotropically Micro-Structured Materials for High Power Laser Applications

Ceramic lasers have helped push the limits of lasing powers, while still maintaining high beam quality and cost effectiveness. Power densities can be pushed up even further by reducing operational thermal gradients in the lasing media, achievable by synthesizing higher thermal conductivity (k) materials. Grain boundaries, ever-present in the typically sintered ceramics, scatter the heat carrying phonons, thus decreasing k. On the other hand, smaller grain sizes enables higher light transmission in the Rayleigh scattering regime. An optimization challenge arises from the opposite scaling laws governing the effect of grain boundaries on k and light transmission.

In this work, we tackle this optimization problem by modeling heat transfer and light transmission through anisotropically microstructured columnar grained materials. Larger characteristic dimensions help maintain high–k in the c-axis direction for good heat dissipation, while preserving light transmission properties in the orthogonal lasing and pumping directions. Monte Carlo ray tracing simulations are carried out to model the anisotropic thermal conductivity in these structures. Light transmission is modeled using exact numerical simulations as well as approximate Rayleigh-Gans-Debye models. This will guide the synthesis of future state of the art high power lasers.

Chapter 3 - A 3 Omega Method to Measure an Arbitrary Anisotropic Thermal Conductivity Tensor

Previous use of the 3 omega method has been limited to materials with thermal conductivity tensors that are either isotropic or have their principal axes aligned with the natural cartesian coordinate system defined by the heater line and sample surface. Here we consider the more general case of an anisotropic thermal conductivity tensor with finite off-diagonal terms in this coordinate system. An exact closed form solution for surface temperature has been found for the case of an ideal 3 omega heater line of finite width and infinite length, and verified numerically. We find that the common slope method of data processing yields the determinant of the thermal conductivity tensor, which is invariant upon rotation about the heater line's axis. Following this analytic result, an experimental scheme is proposed to isolate the thermal conductivity tensor elements. Using two heater lines and a known volumetric heat capacity, the arbitrary 2-dimensional anisotropic thermal conductivity tensor can be measured with a low frequency sweep. Four heater lines would be required to extend this method to measure all 6 unknown tensor elements in 3 dimensions. Experiments with anisotropic layered mica are carried out to demonstrate the analytical results.

Chapter 4 - Easily accessible, low cost approaches to measure the scattering phase function of optically thin samples

Cheap and easily accessible methods to measure the light scattering phase function of thin samples are developed using image resolution techniques. The methods can be distributed into two broad groups determined by the nature of the light source, (1) collimated and (2) diffuse. The effect of the sample on either the edge spread function (ESF) or the modulation transfer

function (MTF) is used to quantify its light scattering properties. For each method, first the point spread function is derived, following which the methods are validated with numerical simulations and experiments with a surface scatterer.

Chapter 5 -Dissertation Summary and Conclusions

This chapter offers a summary of all modeling and experimental results from the thesis, potential future work and their implications.

Chapter 2 - Optimizing Thermal Transport and Light Transmission in Anisotropically Micro-Structured Materials for High Power Laser Applications

2.1 Introduction

Diode pumped solid state lasers[30] have helped push the boundaries of high power lasers. Since lasing was first demonstrated in a polycrystalline ceramic laser,[31] the ability to dope higher concentrations of active elements, which are rare earth elements or transition metals, into polycrystalline, powder-densified samples by using non-equilibrium processes has enabled larger laser slope efficiencies.[4] The limits in power densities in high power lasers are often due to thermal rollover[32] from thermal lensing and depolarization effects, while catastrophic failures can be caused by thermal stress fracture.[33] A higher thermal conductivity, k, of the lasing media reduces the peak temperature and thermal gradients in the lasing media, thus allowing higher lasing powers.[34]

There is an ongoing effort in the ceramic community to develop laser media with thermal conductivities higher than that of the current start of the art Nd:YAG lasers ($k \sim 6$ - 14 W/m-K)[35]. Ceramic sesquioxides[7] with twice the thermal conductivity of Nd:YAG have been developed towards achieving this goal. Ceramics of lighter elements,[36] such as Al_2O_3 and AlN, have the potential to achieve much higher thermal conductivities. Single crystal thermal conductivity of AlN[37] and Al_2O_3[38] are more than 30 times and 4 times higher than that of Nd:YAG respectively. Lasing action has already been observed in Ti and Fe doped AlN,[13,14] while Ti:sapphire (Ti doped single crystal Al_2O_3) lasers are ubiquitous in ultra-fast lasing applications.[15,16] More recently, visible photoluminescence was observed in a Tb:AlN ceramic[39] with a measured thermal conductivity of more than 80 W/m-K at 300 K. Thus AlN and Al_2O_3 ceramics hold great promise as the host material for high power laser media.

In the above polycrystalline ceramics, the grain boundaries cause additional scattering of the heat carrying phonons, which can reduce the thermal conductivity by more than an order of magnitude compared to a single crystal.[40,41] Maintaining high thermal conductivity therefore calls for increasing the grain size, at least to the extent compatible with the non-equilibrium RE doping process[17]. On the other hand, the promising high-k materials AlN and Al_2O_3 are birefringent, so that light propagating through a polycrystal with grains of misaligned orientation sees a slightly different refractive index from grain to grain (e.g., the maximum refractive index variation is $\Delta\eta \sim 0.05$[42] for red light in AlN). This birefringence effect is the primary source of light scattering in highly dense ceramics,[20] and is therefore crucial for determining the beam quality of the laser.

When the refractive index variation and the grain size are both small, such that,

$$\Delta \eta \ll 1$$
$$and \ \ {}^{2\pi\Delta\eta d_g}\!\big/\!{}_{\lambda} < 1,$$

<div align="right">(2-1)</div>

which shall turn out to be the case for nearly all of the present work, the Rayleigh-Gans-Debye (RGD) scattering approximation can be invoked. Here, d_g is the effective diameter of the grains in the polycrystal and λ is the lasing wavelength. Under the RGD approximation, the extinction coefficient of light due to grain boundary scattering decreases with decreasing grain size, which enables higher transmission. Thus, light transmission and thermal conductivity of these sintered ceramics scale oppositely with increasing grain sizes. One way to reduce the scattering of light at grain boundaries is by controlling the crystallographic orientation of the grains. This has been achieved by applying large magnetic fields to magnetically anisotropic powders[8] or by sintering together nanocrystals[9] with large shape anisotropy. Here, we focus on ceramics synthesized using the later scheme.

In this work, we investigate the potential lasing peformance of polycrystals with anisotropic grains by modeling the thermal conductivity and light transmission in such materials. This work has been divided into 3 sections. In each section, we carry out calculations on AlN (wurtzite structure) and Al_2O_3 (corundum structure) as candidates for the host material. We chose Ti as the dopant which substitutes the Al^{3+} cation, because it has been used to demonstrate lasing in both host materials.

First, we first develop approximate analytical models to predict the effect of grain boundaries on the thermal conductivity of polycrystalline materials with anisotropically shaped grains. These approximate models were verified using Monte Carlo ray tracing simulations. In the next section, we apply the RGD scattering approach to calculate the light transmission properties, and verified it with numerical simulations using FEM software (COMSOL). Finally, we propose a figure of merit to quantify the applicability of the anisotropic polycrystals as high power laser media. We calculate the figure of merit as a function of anisotropic grain shapes and sizes and discuss the parameters that affect it.

2.2 Thermal Conductivity

In large bandgap dielectric materials such as sapphire (Al_2O_3) and aluminum nitride (AlN), phonons are the primary carriers of heat. The phonon thermal conductivity can be calculated as

$$k = \frac{1}{3}\sum_{pol}\int C_\omega v_\omega \Lambda_\omega d\omega,$$

<div align="right">(2-2)</div>

where C_ω, v_ω, and Λ_ω are the volumetric heat capacity, group velocity, and the mean free path of each phonon mode, and the sum is over all three phonon polarizations (2 transverse and 1 longitudinal modes). In pure single crystals, the intrinsic phonon-phonon (umklapp) interaction is the primary scatterer of phonons at room temperature. In contrast, as illustrated in Figure 2-1(a), in RE-doped polycrystals, extrinsic scattering by grain boundaries, pores, the RE dopants, and phase inclusions are the dominant scatterers of both the phonons and photons. Even in the

<div align="center">7</div>

best case of fully dense homogenous materials, in which the effect of pores and phase inclusions can be ignored, scattering by grain boundaries and RE dopant are still significant.

When multiple scattering mechanisms are important, typically Mathiessen's rule[43] is used to sum up the effects of the various scattering mechanisms in parallel,

$$\Lambda_{eff,\omega}^{-1} = \Lambda_{umkl,\omega}^{-1} + \Lambda_{imp,\omega}^{-1} + \Lambda_{bdy,\omega}^{-1} + \Lambda_{MD,\omega}^{-1},$$

(2-3)

where Λ_{umkl}, Λ_{imp}, Λ_{bdy} and Λ_{MD} are the mean free paths due to umklapp, impurity, grain boundary, and mass defect scattering due to active dopants. The intrinsic mean free paths, $\Lambda_{umkl,\omega}$ and $\Lambda_{imp,\omega}$, can be inferred from single crystal thermal conductivity vs. temperature data from literature[36] (See Appendix 2.6.2.1 for details). The extrinsic mean free paths, Λ_{bdy} and Λ_{MD}, can vary significantly due to the properties of the sintered polycrystal, such as the quality and shape of the grain boundaries, and the species and density of RE dopant. We will discuss this in more detail in the following subsections.

2.2.1 Grain Boundary Scattering Mean Free Path

To calculate the grain boundary scattering mean free path, Λ_{bdy}, the transmission probability of phonons at grain boundaries has to be known. Previous molecular dynamics simulations[44–46] suggest that the transmission probability varies inversely with the phonon frequency. Following this, a frequency dependent transmission probability,[19,47,48]

$$t_\omega = \frac{1}{\gamma_{bdy} \dfrac{\omega}{\omega_o} + 1},$$

(2-4)

has been used to explain the thermal conductivity of isotropic nano-grained materials.
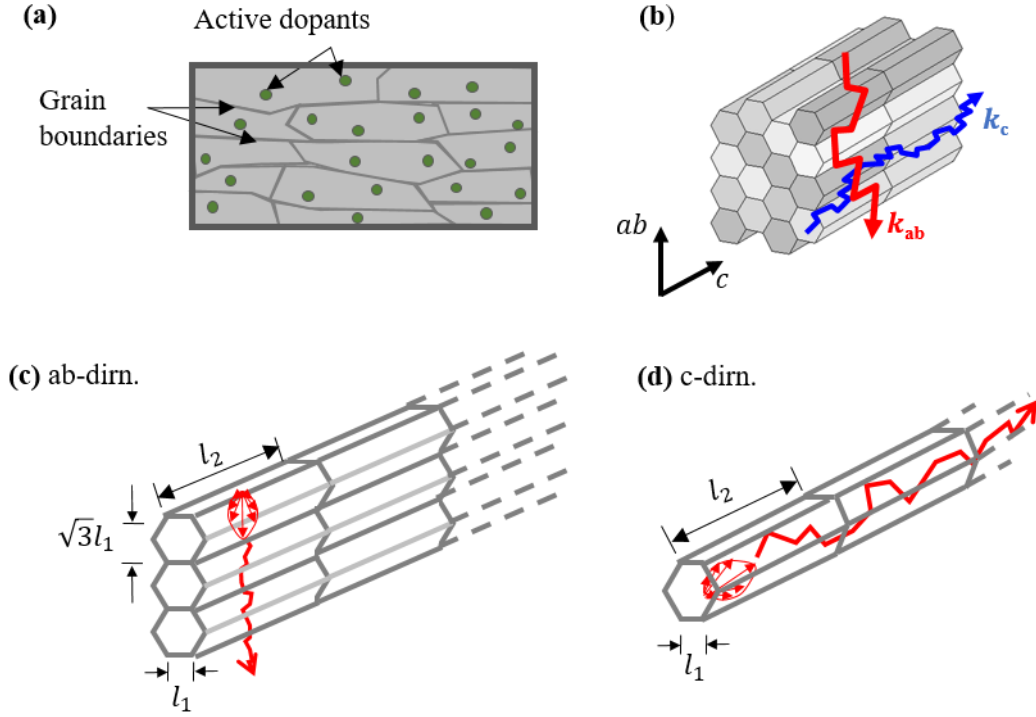
Figure 2-1 (a) The two primary scattering mechanisms affecting heat transport in the polycrystalline AlN and Al₂O₃ ceramics of present interest are grain boundaries and the active dopants. (b) We study the thermal transport properties of a more simplified microstructure comprising aligned hexagonal columnar grains. The aim is to calculate the thermal conductivity tensor elements, k_{ab} and k_c. Phonon ray tracing and models are used to find the boundary scattering phonon mean free path for (c) ab-direction, and (d) c-direction transport.

When the grain sizes are small compared to the phonon mean free paths, grain boundary scattering in the anisotropic nano/micro-structures studied in this work would result in a direction dependent thermal conductivity. Due to the incoherent nature of phonon transport at the length scales and temperatures of interest, the grain boundary contribution to the mean free path for phonon transport in such materials can be modeled by simplifying the structure into a more ordered form[49] (see Appendix 2.6.1).

Table 2-1: Mean free path due to scattering of phonons by grains oriented parallel and perpendicular to the transport direction. $r = l_2/l_1$

Scattering type	Boundary scattering mean free paths	
	$\Lambda_{bdy, ab}$ (Figure 2-1(c))	$\Lambda_{bdy, c}$ (Figure 2-1(d))
Λ_{SL}: Grain boundaries ⊥ to phonon transport direction	$\dfrac{3}{4}\sqrt{3}l_1\dfrac{t(\omega)}{1-t(\omega)}$	$\dfrac{3}{4}l_2\dfrac{t(\omega)}{1-t(\omega)}$
Λ_{NW}: Grain boundaries ∥ to phonon transport direction	$r>1$: $\dfrac{3}{4}l_1\left[\ln(2r)+\dfrac{1}{3r}+\dfrac{1}{2}\right]\left(\dfrac{1+p}{1-p}\right)$ $r<1$:　　　 Eq (2-5)	$1.82l_1\dfrac{1+p}{1-p}$

9

Similarly, for phonon transport along the ab-direction (Fig. 1c), the nano-grained structure simplifies to a superlattice nanowire with a rectangular cross-section (αl_1 x l_2), where α is a correction to capture the presence of the sawtooth boundaries. It was recently shown that the exact analytical solution[50] for the boundary scattering mean free path of a rectangular nanowire can be approximated to within 3% by a simple logarithmic function,[49] which we use here in the bottom-left entry of Table 2-1. The effect of specularity is included for Λ_{NW} calculations, by multiplying the corresponding diffuse value with $(1+p)/(1-p)$, where p is the specularity parameter.[43,51] When the aspect ratio, r, is less than 1, we use the the exact solution of McCurdy *et al.*[50]

$$\Lambda_{NW,ab} = \frac{1}{4}l_1 r^{\frac{1}{2}} \left[\begin{array}{c} 3r^{\frac{1}{2}}\ln\left(r^{-1} + \left(r^{-2}+1\right)^{\frac{1}{2}}\right) + 3r^{-\frac{1}{2}}\ln\left(r + \left(r^{-2}+1\right)^{\frac{1}{2}}\right) \\ -\left(r+r^3\right)^{\frac{1}{2}} + r^{\frac{3}{2}} - \left(r^{-1}+r^{-3}\right)^{\frac{1}{2}} + r^{-\frac{3}{2}} \end{array} \right] \left(\frac{1+p}{1-p}\right) \quad (2\text{-}5)$$

Referring to Fig. 1c, when approximating the microscrutructure along the ab direction as a nanowire of rectangular cross section, the long side of the grain, l_2, directly gives one side length of the rectangle, while defining the other length requires some thought due to the faceted structure.[52] In the limit of perfectly diffuse boundaries, which typically holds true for grain boundaries,[48] the sides of the rectangular nanowire can be reduced to the dimensions bounded by the sawtooth sides, i.e. (l_1 x l_2) for the case of hexagonal grains. In the following sub-section, we will numerically show that this assumption for the geometry gives an acceptable prediction (<25% error), even when the boundaries are highly specular.

The mean free path contributions due to the nanowire and superlattice effects for ab and c-directions are summarized in Table 2-1. The total boundary scattering mean free path for each direction can be calculated by invoking Matheissen's rule, $\Lambda_{bdy}^{-1} = \Lambda_{NW}^{-1} + \Lambda_{SL}^{-1}$. These models are validated with ray tracing simulations in the following sub-section.

2.2.2 Validation of Boundary MFP models with Monte Carlo Ray Tracing
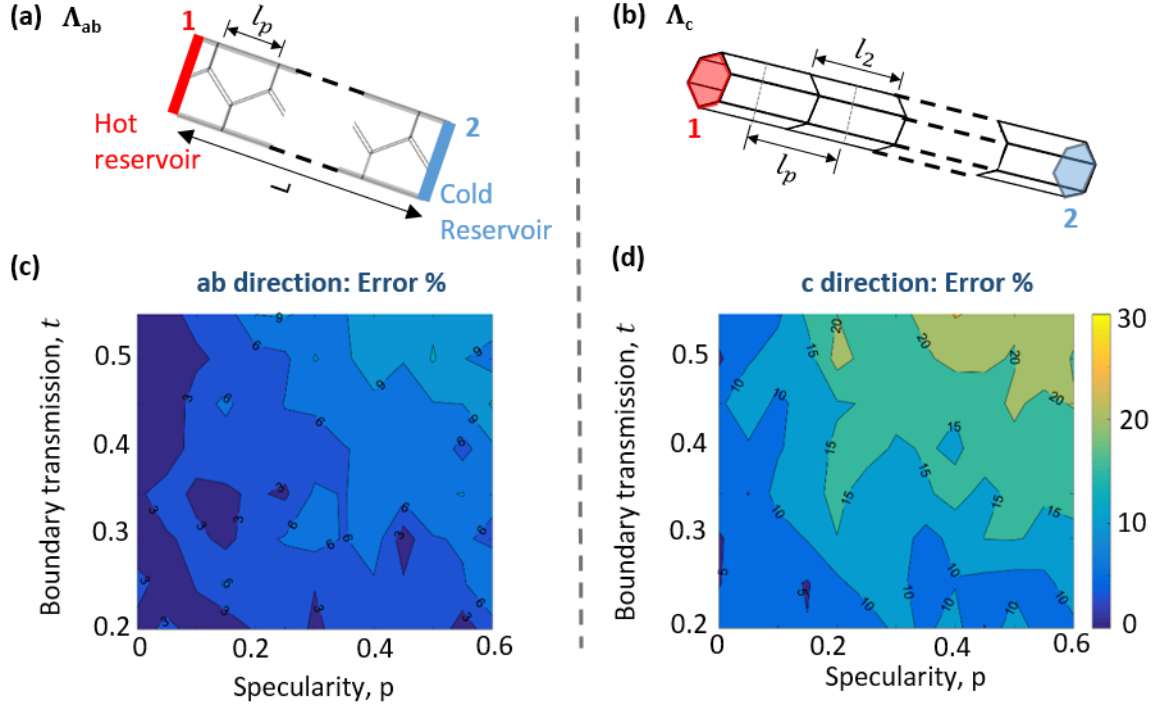
Figure 2-2 (a) and (b) show simulation domains for Monte Carlo ray tracing simulations, for transport along the ab- and c-directions of the microstructure, respectively. Multiple ray tracing simulations (not shown) were carried out with increasing number of periods of period length, l_p shown above, to determine the boundary scattering mean free path. Contour plots for error % between mean free paths predicted by ray tracing simulations and the model of Table 1 are shown for (c) ab-direction and (d) c-direction, as functions of the grain boundary specularity and transmissivity. These results are for an aspect ratio $r = l_2/l_1 = 5$.

To check the approximate analytical expressions of Table 2-1 we used a Monte Carlo ray tracing code[49,53] to calculate the boundary scattering mean free path for selected microstructures. Two different geometries (Figure 2-2(a)) were used to calculate the grain boundary mean free path in the orthogonal ab and c-directions. These reduced geometries exploit periodic boundary conditions and symmetry boundary conditions to reduce the computation time. Therefore we make a distinction between external surfaces (surfaces that bound the simulation domain) compared to internal boundaries (surfaces/interfaces bounded within the geometry). The specularity of the external surfaces can either be completely specular ($p=1$) if they are reflection symmetry planes, as is the case for ab-direction in Figure 2-2(a), or have the same specularity as the grain boundaries they represent, which is true for c-direction transport.

In each of these structures, over 500,000 phonons are launched from the hot surface of the simulation domain. For each phonon, the position and azimuthal angle are randomly chosen with uniform weighting over the hot surface and from 0 to 2π respectively, while the polar angle is randomly chosen from 0 to $\pi/2$ with a weight proportional to its emission probability, $cos\theta sin\theta$. When the phonon hits an external surface, if the value of a generated random number is less than the specified specularity of the boundary, the phonon is specularly reflected. Otherwise the

phonon is diffusely reflected with polar angle and azimuthal angle randomized in a way similar to the emission process. At the grain boundaries, a frequency dependent transmission function, t_ω (Eq. (2-4)) determines the probability with which phonons transmit through the boundary.

With the results of the ray tracing simulations for 500,000 phonons on a single geometry described above, the transmission coefficient, $\langle \tau \rangle$, is calculated as the fraction of the phonons that make it through to the cold lead in the simulated geometry. The standard deviation of $\langle \tau \rangle$ is calculated by analyzing 10 subsamples in a process similar to Lee et al.[49] To calculate the mean free path for a given set of geometry conditions (l_1, l_2) and grain boundary parameters (t, p), we first calculate $\langle \tau \rangle$ for a range of simulation domain lengths, L, where increasing L implies increasing number of periods (period length, l_p shown in Figure 2-2 (a) and (b)). For each length L, following the Landauer formalism[54] the mean free path is calculated as

$$\Lambda_L = \frac{3}{4} L \langle \tau \rangle .$$

(2-6)

Λ_L is not an intrinsic property for a given microstructure unless the simulation domain L is more than an order of magnitude[49] larger than the mean free path value. To keep the computation times small, Λ_L can be calculated for a range of shorter L values, such that the simulation domain has about 5 to 10 periods. Then the boundary scattering mean free path can be calculated as[49,55]

$$\Lambda_{bdy}{}^{-1} = \frac{\partial \left(\dfrac{L}{\Lambda_L} \right)}{\partial \Lambda_L} .$$

(2-7)

Now, we can quantify the error percentage between the mean free path values predicted by the analytical model in Table 2-1 and ray tracing calculations by the formula,

$$Error\% = \left| \frac{\Lambda_{model} - \Lambda_{ray\,tracing}}{\Lambda_{ray\,tracing}} \right| \times 100 ,$$

(2-8)

The error percentages are shown in Figure 2-2(b) for a microstructure with moderate anisotropy, $l_2/l_1=5$. Over a wide range of specularity and boundary transmission fractions, the errors are less than 10% for transport in the ab-direction and below 25% for the c-direction. This is an acceptably small variability considering that the value of $\Lambda_{ray\,tracing}$ itself varies by a factor of 3 over this range of parameters. Similar MC simulations were performed for $l_2/l_1=10$ and 20, and in all cases, the errors due to the approximations of Table 2-1 were found to be below 25%. Thus, for the remainder of this study we use the highly computationally efficient models of Table 2-1.

2.2.3 Thermal conductivity of doped AlN and Al₂O₃

A typical ceramic laser gain media is doped with heavy rare earth or transition metals which are required for the lasing action. Because these dissimilar dopant atoms represent defects in the periodic lattice of the host media, they also cause Rayleigh-like scattering[56,57] of phonons. Such mass-defect (MD) scattering can be described by a quadratic dependence on phonon frequency,

$$\Lambda_{MD}^{-1} = \frac{A_{MD}\omega^4}{v_\omega},$$
(2-9)

where v_ω is the phonon group velocity and the coefficient A_{MD} depends on the mass difference between the active dopant and the ceramic host material, which we calculate using the formula proposed by Slack.[58] More details are included in Appendix 2.6.2.1. As discussed in the introduction, we use Ti with 1at% concentration as the dopant.

Finally, we find the effective mean free path by combining all the major scattering mean free paths using Mathiessen's rule, Eq. (2-3). The thermal conductivity is calculated using Eq. (2-2) for ab- and c-direction by using the respective effective mean free paths. The details for this calculation are included in Appendix 2.6.2. We calculate k for two different strengths of boundary scattering, $\gamma_{bdy} = 1$ and 5, corresponding to good and bad grain boundary transmission respectively. The results are compiled in the contour plots of Figure 2-3.
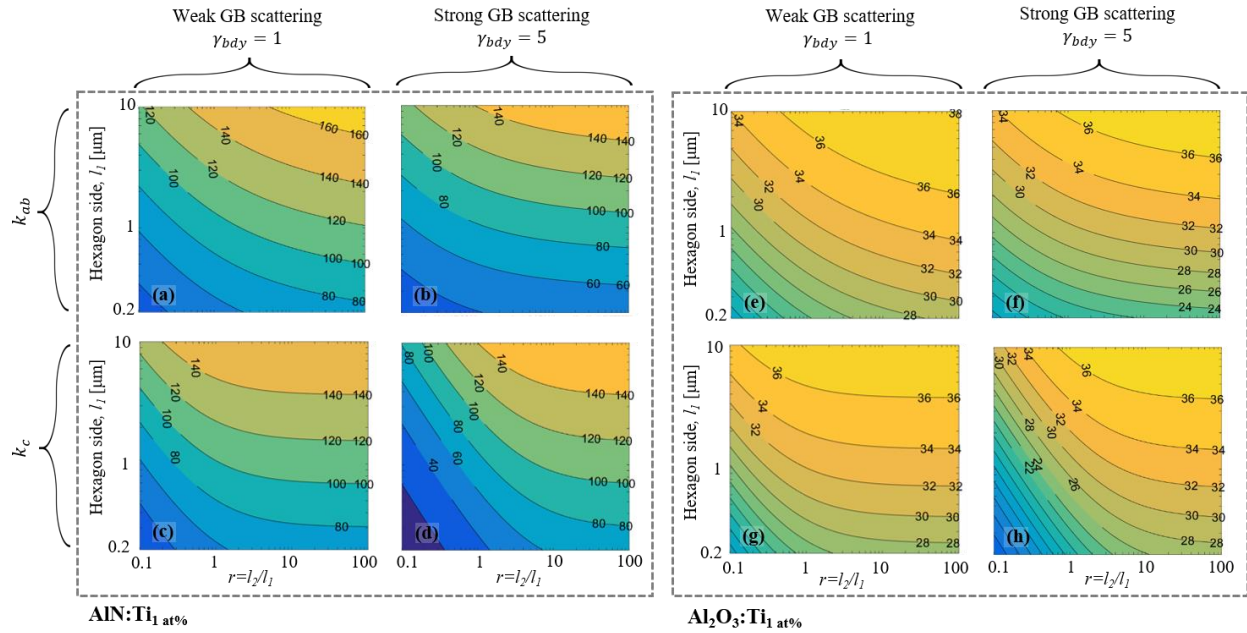
Figure 2-3 Calculated ab- and c-direction thermal conductivity (colored contour levels) for 1at%Ti doped AlN (left) and Al₂O₃ (right). Each plot is a function of the same sweep of aspect ratios $r = l_2/l_1$ from 0.1 to 100 and the transverse grain length parameter l_1 (200 nm to 10 μm). $r<1$ and $r>1$ corresponds to disk-like and columnar grains respectively. Two values of grain boundary scattering parameters are shown: (i) weak boundary scattering, $\gamma_{bdy} = 1$ and (ii) strong boundary scattering, $\gamma_{bdy} = 5$.

We have carried out calculations for a wide range of aspect ratios ranging from r =0.1 to 100, where $r<1$ corresponds to disk-like grains. Since AlN has much longer mean free paths (see Figure 2-8(b)) than the grain sizes considered in this study, the strength of grain boundary scattering, γ_{bdy}, is expected to have a significant effect on its thermal conductivity. This is easily observed upon comparing Figure 2-3(a) and (b), where k_{ab} reduces by 25% for the smallest grain sizes upon increasing γ_{bdy} from 1 to 5. On the other hand, the corresponding change in k_c from Figure 2-3(c) to (d) is less than 5%, which shows that grain boundary scattering affects k_{ab} much more severely compared to k_c for large aspect ratio grains. Even with poor grain boundary transmission, it is possible to achieve high thermal conductivity in the c-direction.

On the other hand, both grain boundaries and active dopants have a very small effect on the thermal conductivity of Al$_2$O$_3$ because of the small intrinsic mean free paths. From the mean free path accumulation functions in Figure 2-8(b), we expect that Λ_{bdy} of 200 nm would cause only a 30% decrease in k of Al$_2$O$_3$, compared to a 70% decrease in AlN. We observe a similar effect when comparing Figure 2-3 panel (b) with (f) for $r = 10$. As the grain sizes decrease from 10μm to 200nm, k_{ab} decreases by more than 60% for AlN, while the corresponding decrease in Al$_2$O$_3$ is only 20%.

In addition, in Appendix 2.6.2.1, we note that the lasing dopants can be a dominant phonon scattering mechanism due to the large mass difference between the typically heavy active dopants and the lighter atoms of AlN or Al$_2$O$_3$. It is critical to think deeply about the choice of the host material and active dopants to minimize the reduction in thermal conductivity.

2.3 Light Transmission

2.3.1 Light Scattering at Grain Boundaries

It is essential to reduce energy loss due to extinction of light within a lasing media to enable high power lasing.[59] In highly pure, dense, polycrystals composed of anisotropic large bandgap materials, birefringence scattering at the grain boundary interfaces[20] is the primary source of intrinsic attenuation. The overall transparency of a slab of sintered ceramic of thickness l is often quantified by its real inline transmission,[20]

$$RIT = (1-R)^2 e^{-\beta_{sca} l} , \qquad (2\text{-}10)$$

where R is the reflectivity at an air-ceramic interface which can be easily calculated using the Fresnel relations and β_{sca} is the extinction coefficient due to scattering. We will lay out the path to calculating β_{sca} in this section. Hexagonal materials such as AlN and Al$_2$O$_3$ are birefringent, which implies a slightly different refractive index for the ordinary, η_o and the extraordinary rays, η_e.[20,42] The refractive indices for AlN and Al$_2$O$_3$ are listed in Table 2-2. Light propagating through a polycrystalline ceramic with perfectly crystallographically aligned grains does not see any change in refractive index when crossing a grain boundary. Thus there is no light scattering.

Table 2-2: The refractive indices used for the scattering cross-section calculations for light with λ=400nm [20,42]

Host Material	η_e	η_o
AlN	2.12	2.16
Al$_2$O$_3$	1.760	1.768

However, the misalignment of grains in a real polycrystalline material causes light scattering as shown in Figure 2-4(a). In this work, we define misalignment as the average angle χ between the c-axes of the underlying hexagonal crystal structure of individual grains in the polycrystal. Since misalignments of less than 20^0 has been achieved by various methods such as magnetic alignment[60] and using crystallites with shape anisotropy,[9] we will limit our study to small misalignments. For a given misalignment χ, the change in refractive index at grain boundary interfaces can be calculated as[61]

$$\Delta\eta(\chi) = \sqrt{\frac{\eta_o^2 \eta_e^2}{\eta_o^2 \sin^2 \chi + \eta_e^2 \cos^2 \chi}} - \eta_o \tag{2-11}$$

where χ is the angle between the polarization and the c-axis, and η_e and η_o are the refractive indices for the extraordinary and the ordinary rays. This change in refractive index is independent of the light propagation direction because of the typically small birefringence ($\Delta\eta_{max} = |\eta_e - \eta_o|$) in these materials.
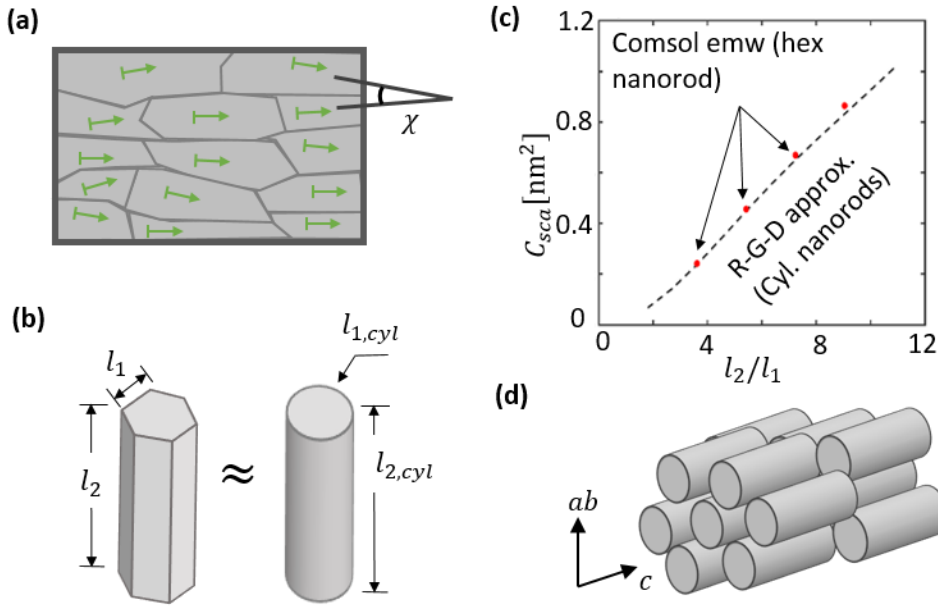
Figure 2-4 (a) In realistic ceramics, slight differences in refractive index, $\Delta\eta$, due to the misalignment χ between columnar grains cause light scattering . Here the green arrows represent the c-axis of the hexagonal crystal structure of AlN or Al$_2$O$_3$ (b) Faceted hexagonal shaped columnar grain structures are represented by cylinders of the same volume (Eq. (2-12)). (c) RGD calculation (dashed line) for representative cylinders agrees very well with computationally expensive Comsol simulations (red points) on hexagonal scatterers. Modeling parameters: λ=1μm, $\Delta\eta$=0.0025 and l_1=110.5nm (d) 3D view of the effective medium model comprising representative cylinders dispersed in a matrix with refractive index contrast, $\Delta\eta(\chi)$. The volume fraction of the scattering cylinders is 0.5.

To calculate the extinction coefficient, we build on the approach of Apetz, et al.[20] by approximating the polycrystal as an effective medium where cylinders of refractive index η are distributed within a matrix of slightly different index $\eta + \Delta\eta(\chi)$, with a volume fraction of 0.5 (Figure 2-4(c)). Each hexagonal crystallite is approximated as a cylinder with the same length and volume, corresponding to

$$l_{1,cyl} = 1.82 l_1 \text{ and } l_{2,cyl} = l_2. \tag{2-12}$$

To calculate the scattering coefficient, β_{sca}, first we need to calculate the scattering cross-section of each individual scatterer. Since we focus on grain sizes small enough such that Eq. (2-1) is satisfied, the RGD approximation can be applied. Then the scattered intensity due to a single cylinder at a large distance, ρ, can be calculated in the RGD approximation following van de Hulst[62] as

$$I(\theta,\phi) = I_0 \frac{(1 + \cos^2\theta)}{2} \frac{2\pi^2 V^2 |\Delta\eta|^2}{\rho^2 \lambda^4} |R(\theta,\phi)|^2, \tag{2-13}$$

where V is the volume of the scattering cylinder, and the shape factor,

$$R(\theta,\phi) = \frac{1}{V} \int e^{i\delta} dV. \tag{2-14}$$

The phase δ is the phase difference between light scattered by each point in the scatterer and a reference point. Then the scattering cross-section is calculated by integrating the scattered intensity over the entire sphere surrounding the scatterer:

$$C_{sca} = \frac{1}{I_0} \int_{\theta=0}^{\pi} \int_{\phi=0}^{2\pi} I(\theta,\phi) \rho^2 \sin\theta d\theta d\phi. \tag{2-15}$$

Note that I_0 and ρ were arbitrary and therefore drop out after substituting Eq. (2-13) into Eq. (2-15).

We first check the validity of the hexagon-to-cylindrical approximation (Eq. (2-12)) by comparing the scattering cross-section of a single cylinder calculated with the RGD approximation (Eq. (2-15)) against numerical simulation results for a corresponding hexagonal nanorod using the emw module of COMSOL Multiphysics. Following the simulation scheme of Yushanov et al.[63] we calculated the scattering cross-section for unpolarized light incident on a hexagonal nanorod. Figure 2-4(c) shows that the scattering cross-sections calculated by the two methods agree very well for a sweep of aspect ratios, thus demonstrating the validity of the cylindrical grain approximation.

2.3.2 Effective Medium – Independent Scattering

Now that the scattering cross-section of individual scatterers is known, the next step is to combine the effects of the multiple grains in a polycrystal using the effective medium model described before. Due to the sub-micron size and high volume fraction (0.5) of scatterers in the current study, the effective single scattering cross-section of each particle can be different than that of individual isolated particles because of coherent interference of the scattered waves. For packed systems, generally when the minimum inter-particle distance, either l_1 or l_2, is larger than half a wavelength,[64–66] then the scattering from each particle is independent, and the effect of the large number of scatterers is simply additive. In this limit, the product of the number density and the scattering cross-section of the scattering centers in the propation medium gives the extinction coefficient. To ensure the validity of independent scattering, a lasing wavelength of 400 nm (typical minimum wavelength accessible in a Ti-sapphire laser, ref: https://cohrcdn.azureedge.net/assets/pdf/Chameleon-OPO-Vis-Data-Sheet.pdf) implies that the minimum distance between scatterers, here l_1, is restricted to be at least *200* nm. Further analysis in this section will be limited to these sizes. We discuss the possibility to extend the analysis for even smaller grain sizes in Appendix 2.6.4.

We first consider the effects of the grain packing and alignment on the optical properties of the effective medium. The misalignment of crystallites can influence the scattering cross-section for a fixed refractive index contrast $\Delta\eta$, the refractive index contrast itself along the transport direction (Eq. (2-11)), and the packing of the grains within the ceramic. Since RGD scattering assumes that each infitesmally small volume element acts as a Rayleigh scatterer,[62] the scattering cross-section for each scattering cylinder is proportional to the square of the refractive index contrast, $\Delta\eta$. On the other hand, the density of scatterers in the two orthogonal directions for light transmission is related to the projections of the grains in those directions, i.e., $\cos\chi$ and $\sin\chi$. In Appendix 2.6.3, we show that the relative changes in the above projections are negligible in comparison to changes in the refractive index contrast at the small χ values considered in this study. Thus we ignore the changes in packing fraction as a higher order correction in this work.

With the above approximations, and considering the density of scatterers in the effective medium representation of Figure 2-4(d), the extinction coefficients in the orthogonal directions are calculated as

$$\beta_{sca,ab} = C_{sca,ab}(\Delta\eta(\chi))\frac{0.5}{\pi d_{1,cyl}^2 l_2 \big/ 4} \ and \ \gamma_{sca,c} = C_{sca,c}(\Delta\eta(\chi))\frac{0.5}{\pi d_{1,cyl}^2 l_2 \big/ 4}, \tag{2-16}$$

where $\beta_{sca,ab}$ and $\beta_{sca,c}$ are the extinction coefficients for light propagating in the ab and c directions. $C_{sca,ab}$ and $C_{sca,c}$ are the scattering cross-sections for plane unpolarized light incident broadside and end-on respectively on the scattering cylinders.
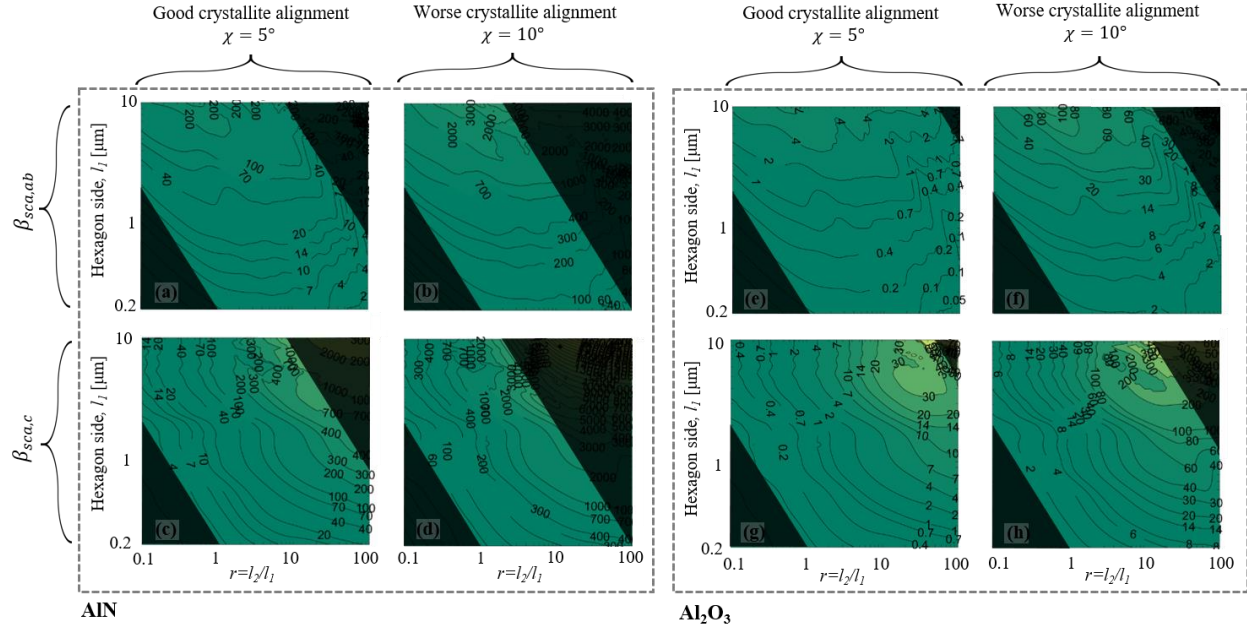
Figure 2-5 Calculated extinction coefficients for (left) AlN and (right) Al₂O₃ ceramics in the ab and c directions using the RGD approximation in the independent scattering limit for two values of the average grain misalignment, $\chi = 5°$ and $10°$ with an incident wavelength, $\lambda = 400$nm. The transparent black shaded region in each panel do not satisfy the criteria for RGD approximation ($2\pi\Delta\eta l_2/\lambda < 0.5$ and $2\pi\Delta\eta(1.81l_1)/\lambda < 0.5$)[67] and/or independent scattering approximation ($\min(l_1, l_2)/\lambda > 0.5$). We observe that the smallest $\beta_{sca,ab}$ is achieved when $r > 1$, while smallest $\beta_{sca,c}$ is achieved when $r < 1$.

With the above information, contour plots of scattering coefficients for anisotropic polycrystalline AlN and Al₂O₃ ceramics are plotted in Figure 2-5. The extinction coefficients in Al₂O₃ ceramics are smaller by more than an order of magnitude because of the small birefringence, $\Delta\eta_{max}$[20,42]. In addition, for both materials the preferred small scattering coefficients are in the ab-direction (compare Figure 2-5 panel (a) with panel (c) and panel (e) with panel (h)) when $r > 1$, even though the interface density is actually higher. On the other hand, $\beta_{sca,ab}$ is smaller when $r < 1$, i.e, for disk-like grains, because the propagation direction with shorter grain dimensions switches. This is in contrast to the trends we observed for thermal conductivity in Figure 2-3, where a preferred higher k was observed in the direction with the greater spacing between grain boundaries. It is also notable that increased misalignment can lead to big amplifications of the extinction coefficient because of the $C_{sca} \propto \Delta\eta(\chi)^2$ scaling.

2.4 Discussion: Optimizing Microstructure for Maximal Lasing Power

In the previous two sections, we found that in polycrystalline ceramics, both thermal conductivity, k (Figure 2-3) and light scattering coefficients, β_{sca} (Figure 2-5) are severely affected by the size and aspect ratio of the grains. Generally smaller grains lead to a decrease in thermal conductivity but with better light transmission properties. We also found that the transport properties of heat and light are functions of direction as well. This suggests that there is an optimum of sizes and aspect ratios of grains, as well as the directions for heat dissipation and light propagation. To find this optimum, we first introduce a figure of merit, FOM, by considering the effects of the grain sizes on the laser's slope efficiency and heat dissipation capabilities.

For diode pumped solid state lasers in steady state operation, the output power can often be described by [59,68]

$$P_{out} = \sigma_S \left(P_{in} - P_{th} \right),$$
(2-17)

where σ_S is the slope efficiency, P_{in} the input pump power, and P_{th} is the threshold power for the lasing media. It is easily seen that a small threshold power and a large slope efficiency enable high lasing powers. It is well-known[59,68] that this is achievable by minimizing the threshold gain or the optical losses within the laser,

$$g_{th} = \frac{1}{2l} \ln \left(R_1 R_2 \right) + \beta_{ext},$$
(2-18)

where R_1 and R_2 are the reflectivity values for the 2 mirrors bounding the lasing cavity, and β_{ext} is the total extinction coefficient due to absorption in the gain media and scattering losses. When the lasing cavity is long, which is typical in high power lasers, [3,69] the scattering coefficient is the dominating loss term. In large bandgap materials like AlN, scattering is the primary source of losses within the media, and thus, β_{ext} can be replaced by β_{sca}.

On the other hand, the thermal load is distributed throughout the laser due to quantum defect heating, which is a fraction of pumping power,[70] leads to thermal gradients during laser operation. These thermal gradients are inversely proportional to the thermal conductivity of a uniformly doped lasing media,[34,71]

$$\nabla T \propto \frac{P_{in}}{k}.$$
(2-19)

For a given lasing media, thermal rollover occurs when thermal lensing and depolarization losses, caused due to thermal gradients[34,72,73] within the lasing media, become significant compared[74] to the output power. Similarly, thermal stress fracture also limits the maximum thermal gradient in the cavity.[71] From Eq. (2-19), we know that the maximum input power is limited by the maximum allowable thermal gradient, and is directly proportional to k. Then, by invoking Eq. (2-17), we find that the maximum lasing output power,

$$P_{out,\max} \propto \frac{k \nabla T_{\max}}{g_{th}}.$$
(2-20)

Often, the pumping and the heat dissipation direction can be different depending on the lasing geometry.[75] Here, by assuming flexibility in the choice for the above 2 directions, we define a figure of merit that needs to be maximized for high output powers,

$$FOM_{i,j} = \frac{k_i}{g_{th,j}} = \frac{k_i}{-\dfrac{1}{2l} \ln \left(R_1 R_2 \right) + \beta_{sca,j}},$$
(2-21)

where i and j determine the directions (ab or c) for thermal transport and light transmission respectively.

In Figure 2-6, we show the resulting FOM values for anisotropic polycrystalline AlN and Al_2O_3. We use a typical output mirror reflectivity, R_2 of 0.9,[59] high R_1 of 1, and a long lasing cavity length of more than 10 cm, which is common for high power lasers.[3,69] A conservative misalignment of $\chi=10°$ is assumed for the scattering cross-section calculations. The thermal conductivity values are the same as that calculated in Figure 2-3 with $\gamma_{bdy}=5$.
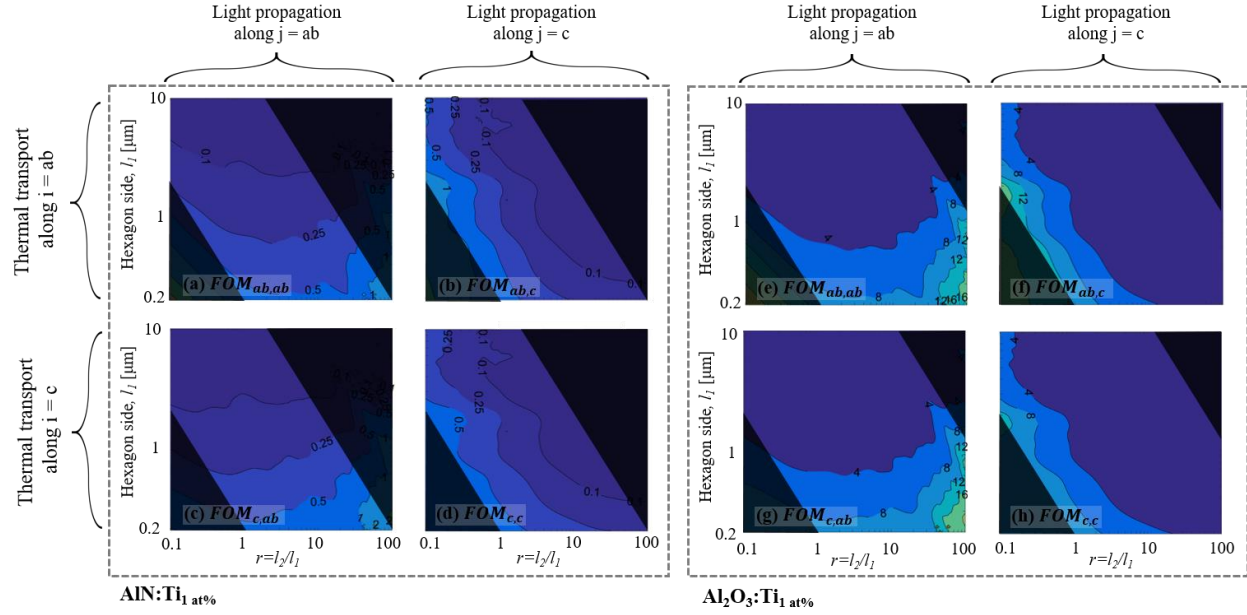
Figure 2-6 Calculated $FOM_{i,j}$ for AlN and Al_2O_3, from evaluating Eq. (2-21) with thermal conductivity and scattering coefficient results from Figure 2-3 and Figure 2-5. The thermal conductivity calculations are carried out assuming a 1at% Ti doping and strong boundary scattering, $\gamma_{bdy}=5$ (Figure 2-3 b, d, f and h). The scattering coefficient calculations are carried out in the independent scattering regime assuming a misalignment, $\chi = 10°$ for light transmission calculations (Figure 2-5 (b, d, f and h)). An output mirror reflectivity, $R_2=0.9$ and high $R_1=1$ is chosen. Note that the plots use different color scales for their FOM. Similar to Figure 2-5, the opaque shaded region in each panel do not satisfy the criteria for RGD approximation $(2\pi\Delta\eta l_2/\lambda<0.5$ and $2\pi\Delta\eta(1.81 l_1)/\lambda<0)$[67] and/or independent scattering approximation $(\min(l_1,l_2)/\lambda > 0.5)$.

It is easily seen that the right bottom quadrant ($l_1<\lambda$ and $r>1$) for ab-direction light transmission and c-direction thermal transport have the best performance, with $FOM_{c,ab}$ values exceeding 1 W/K in AlN and 10 W/K in Al_2O_3 for the range of parameters considered. High $FOM_{ab,c}$ values are achieved also when $r<1$, since we expect higher k_{ab} compared to k_c for disk-like grains, while the scattering coefficient stays small in c-direction because of the small thickness of the grains. Thus, an anisotropic microstructure comprising hexagonal columnar grains with small cross-section and long lengths, or disk-like grains with large cross-section and small thickness, helps optimize for the maximum lasing powers.

In Al_2O_3, due to its small bulk mean free paths, as discussed earlier there is a smaller difference between k_{ab} and k_c (compare panels Figure 2-3 (f) and (h)). Thus, the calculated $FOM_{ab,ab}$

20

(Figure 2-6 (e)) and $FOM_{c,ab}$ (Figure 2-6 (g)) are very similar. This can be an important consideration when the choice of heat dissipation direction is not flexible. Hence, it is also crucial to know the spread in mean free path accumulation for the developed ceramics to predict the effect of grain boundaries on thermal transport.

Even though doped polycrystalline Al_2O_3 has a smaller thermal conductivity than AlN, the achievable FOM values in Figure 2-6 can be an order of magnitude higher than AlN. This is because of the smaller birefringence in Al_2O_3, which helps maintain a high light transmission even at large misalignments between grains. For AlN, it is much more crucial to reduce the misalignment between the anisotropically shaped grains to enable high lasing power lasing.

2.5 Conclusion

In this paper, we have explored the advantages of anisotropic micro-structured materials towards developing higher power lasers. The thermal conductivity was calculated using Eq. (2-2), where the effect of grain boundaries and active dopants were included in addition to intrinsic scattering. For light transmission, the RGD approximation was invoked and the extinction coefficient was calculated assuming independent scattering. The contour plots of Figure 2-3 and Figure 2-5 show the importance of the dimensions, orientation, and quality of the grain boundaries for both light transmission and thermal conductivity. We proposed a figure of merit, $FOM_{i,j}$, that needs to be maximized to achieve high lasing powers. From the results of Figure 2-6, we found that an anisotropic micro/nano-structure can indeed be a means to increase lasing power. We also showed that it is crucial to consider the phonon mean free paths, maximum birefringence, and the mass of the dopants in selecting the lasing media.

2.6 Appendices

2.6.1 Similar mean free paths for staggered vs aligned structures
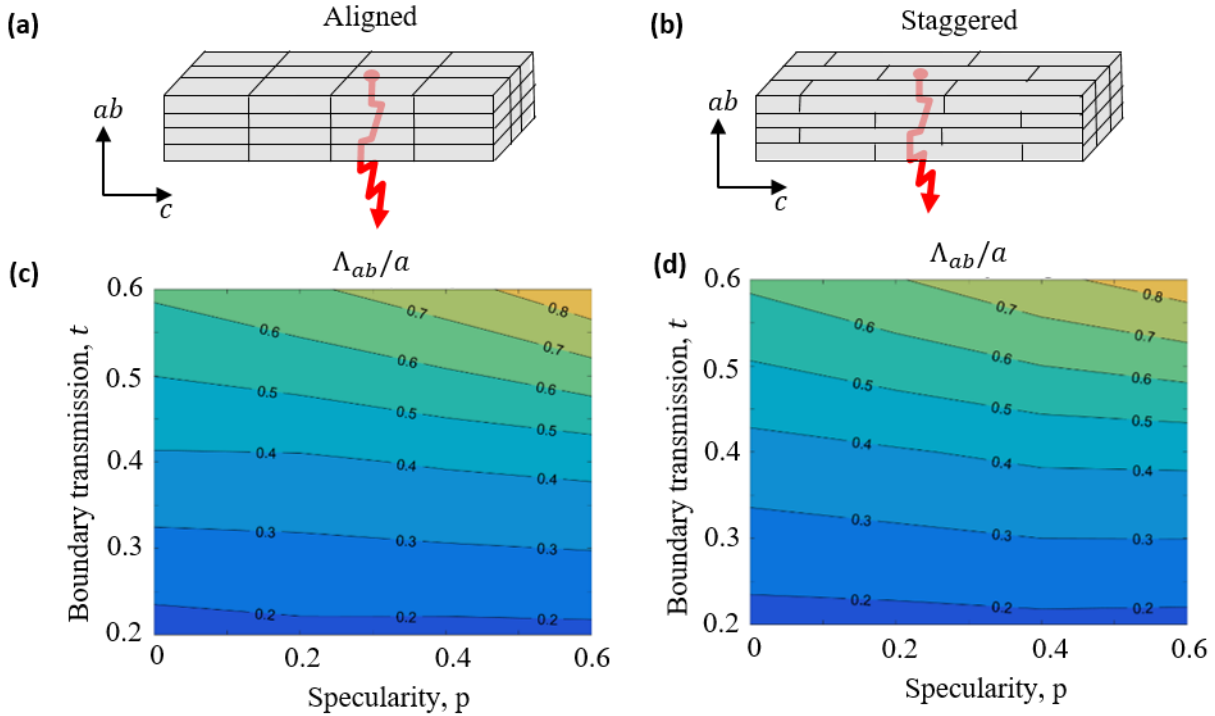
Figure 2-7 Calculated mean free paths, Λ_{ab} for an aligned and staggered structure using Monte Carlo ray tracing. The grains are cuboidal of size (250 nm, 50 nm, 50 nm)

In Figure 2-1(b-d), we had proposed a simplified ordered structure to represent realistic nanostructured polycrystalline materials for thermal conductivity modeling. In this section, we show the validity of this approximation by calculating the mean free path for grain boundary scattering, Λ_{bdy}, for an aligned and an staggered structure for through plane transport. The grain structure is cuboidal with a square cross-section of side l_{1sq}=50nm and length l_2=250nm. Two kinds of geometries are studied here: 1) The grains are aligned such that the boundaries are aligned right on top of each other as shown in the schematic of Figure 2-7(a), and 2) alternate grains are perfectly staggered (Figure 2-7(b)). We see that the results for the two cases, i.e., Figure 2-7(c) and (d)), are very similar for the same range of boundary transmission and specularity values considered in the main text (Figure 2-2). This is expected because of the incoherent nature of phonon transport. Thus it is possible to find the appropriate boundary mean free path models by studying the simpler aligned structure of Figure 2-1(b)

2.6.2 Modeling the mean free paths and thermal conductivity of bulk AlN and Al₂O₃

To predict the thermal conductivity of nano-grained ceramics, it is essential to know the intrinsic mean free paths for phonons in the corresponding bulk single crystal. In these dielectric single crystals around room temperature and above, there are mean free paths associated with three primary scattering mechanisms[54,76]: (i) Umklapp scattering,

$$\Lambda_{umkl}^{-1} = \frac{B_1\omega^2 T \exp\left(-\frac{B_2}{T}\right)}{v_\omega}, \tag{2-22}$$

(ii) impurity scattering,

$$\Lambda_{imp}^{-1} = \frac{A_1\omega^4}{v_\omega}, \tag{2-23}$$

and (iii) physical boundary scattering, D. The fitting parameters, B_1, B_2, A, and D are obtained by fitting literature data for $k(T)$ of single crystals of AlN[11] and Al_2O_3.[38] Broadly speaking, it is well-known that umklapp scattering is most important at high temperatures (room temperature and above), boundary scattering at low temperatures (cryogenic), and impurity scattering near the peak in the bulk k(T) curve.

In the integration of Eq. (2-2), we first apply the common approximation of lumping[76–78] the three acoustic branches into a single triply degenerate branch. The common sound velocity, v_s for the branch is

$$\frac{1}{v_s^2} = \frac{1}{3}\left(\frac{1}{v_{sL}^2} + \frac{2}{v_{sT}^2}\right), \tag{2-24}$$

where v_{sL} and v_{sT} are the longitudinal and transverse sound velocities values from literature. We use an isotropic Born-von Karman (BvK) model for the dispersion relation,

$$\omega = \omega_0 \sin\left(\frac{\pi k}{2k_0}\right), \tag{2-25}$$

where k is the phonon wave vector and k_0 is the Debye cutoff wave vector given by

$$k_0 = \left(6\pi^2 N_{atoms}\right)^{1/3}. \tag{2-26}$$

N_{atoms} is the number density of atoms, which we calculate from known density and atomic masses of the constituent elements. ω_0 is calculated by matching the small wave-vector group velocity with v_s. By using the average number density for all atoms instead of the number density of primitive unit cells, we can take the contribution of the optical phonon modes with non-negligible group velocities[79,80] in AlN and Al_2O_3 into account. The values of the fitted parameters are listed in Table 2-3.
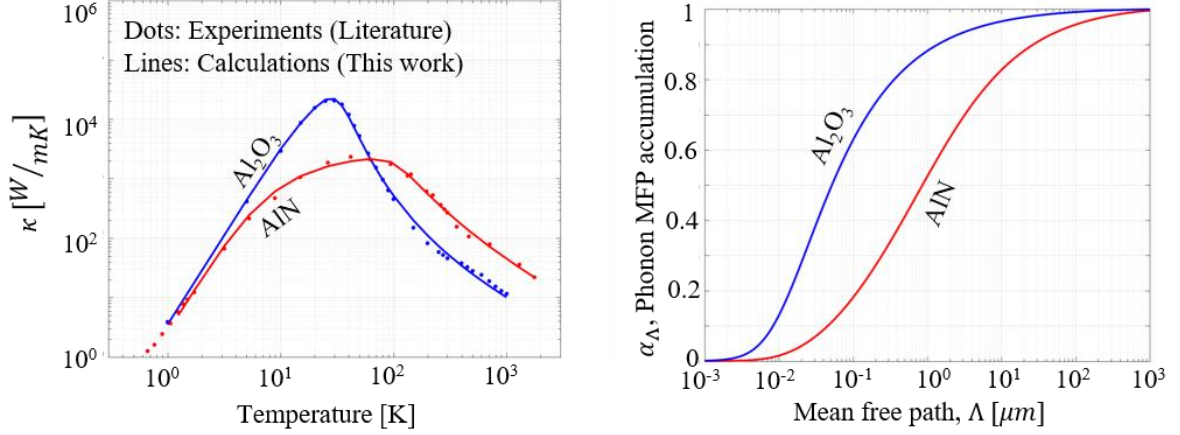
Figure 2-8 Fitted results for thermal conductivity (left), and resulting mean free path accumulation functions (right) for (red) AlN and (blue) Al₂O₃. Phonons in single crystal AlN have mean free paths more than an order of magnitude longer than that of Al₂O₃.

In the right panel of Figure 2-8, we have also plotted the mean free path (MFP) accumulation functions, α_Λ, which is the cumulative fraction of heat carried by phonons with mean free path less than Λ. This makes it intuitive to infer the grain sizes that can significantly affect the thermal conductivity. In AlN, the mean free paths are relatively longer, with about 50% of the heat carried by phonons with mean free paths longer than 1 μm, compared to less than 10% for Al₂O₃. From these mean free path accumulation plots, we expect that the sub-micron sized grain boundaries will have more significant effects on the thermal conductivity of AlN than Al₂O₃, which is confirmed in Figure 2-3. For example, with strong grain boundary scattering, $\gamma_{bdy}=5$, the ab-direction thermal conductivity of AlN decreases by 70% as l_1 is reduced from 0.5 μm to 0.05 μm, in comparison to a 50% decrease in the case of Al2O3.

2.6.2.1 *Point Defect Scattering due to active Dopants*

We calculate the effect of active dopants, here Ti, on thermal conductivity following Slack.[58] The mass defect parameter of Eq. (2-9), A_{MD}, is

$$A_{MD} = \frac{V_o \Gamma}{4\pi v_s^3},$$
(2-27)

where

$$\Gamma = \sum_i f_i \left(1 - \left(\frac{M_i}{M_{avg}}\right)\right)^2,$$
(2-28)

V_o is the average volume of the primitive unit cell, v_s is the effective sound velocity of Eq. (2-24), f_i is the fraction of the primitive unit cells with impurity i, M_i is the mass of the primitive unit cell with impurity i, and M_{avg} is the average total mass of the primitive unit cells in the RE-doped polycrystal. Both AlN and Al₂O₃ have 2 compounds in the primitive unit cell. Thus 1at% RE doping implies that $f_i = 0.020$ in AlN and $f_i = 0.040$ in Al₂O₃. A_{MD} values for 1 at% Ti doped

24

in AlN and Al_2O_3 are listed in Table 2-3, which is used for the thermal conductivity calculations in Figure 2-3 and Figure 2-6.

Because A_{MD} scales with the square of the mass difference (Eq. (2-28)), the mass of the RE dopant becomes an important consideration. For example, 1at% Tb, which has an atomic mass more than 5 times that of the Al atom it substitutes, results in A_{MD} values of 6.87×10^{-43} s^3 and 27.7×10^{-43} s^3 in AlN and Al_2O_3 respectively. This is more than 30 times the values reported in Table 2-3 for 1at% Ti, and can lead to close to an order of magnitude decrease in the calculated thermal conductivities.

Table 2-3 Summary of calculated (ω_0, v_s, and A_{MD}) and best-fit parameters (A_1, B_1, and B_2) used for thermal conductivity calculations

Host Material	$\omega_0/2\pi$ [THz]	v_s [m/s]	A_1 [10^{-45} s^3]	B_1 [10^{-19} s/K]	B_2 [K]	A_{MD} [10^{-45} s^3]
AlN	10.99	6084	12.53	2.23	470	18.2
Al_2O_3	9.19	4753	0.10	9.24	225	72.3

2.6.3 Effect of misalignment on packing compared to C_{sca}
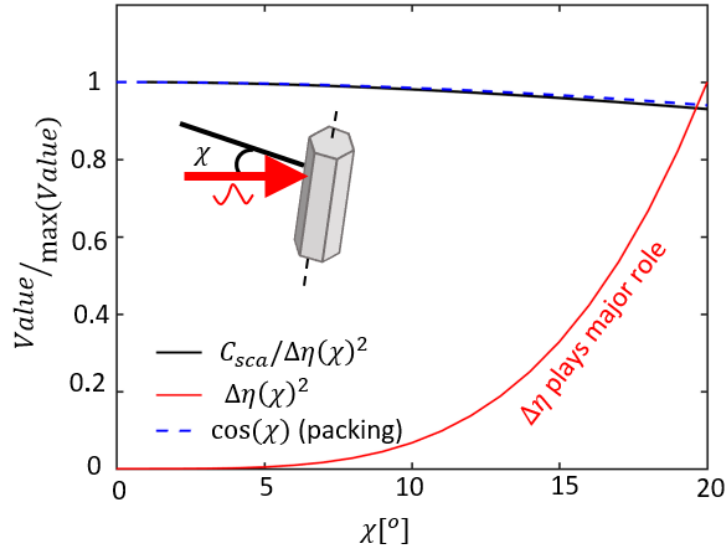
Figure 2-9 Relative changes in normalized scattering cross-section, refractive index contrast, and trigonometric identities representing packing as a function of misalignment. Changes in refractive index dominates over changes in packing. Geometry parameters: $2\pi l_1/\lambda = 0.63$, $r = l_2/l_1 = 6$.

Plots of normalized values of the scattering cross-section divided by $\Delta\eta(\chi)^2$, $\Delta\eta(\chi)^2$, and $cos(\chi)$ show that there is only considerable change in the refractive index contrast, $\Delta\eta(\chi)$ for misalignments within $20°$. Thus, changes in the packing fraction, which is described by $cos(\chi)$ can be ignored. Hence, the relation in Eq. (2-16) between C_{sca} and β_{sca} holds true for small misalignments.

2.6.4 Dependent scattering
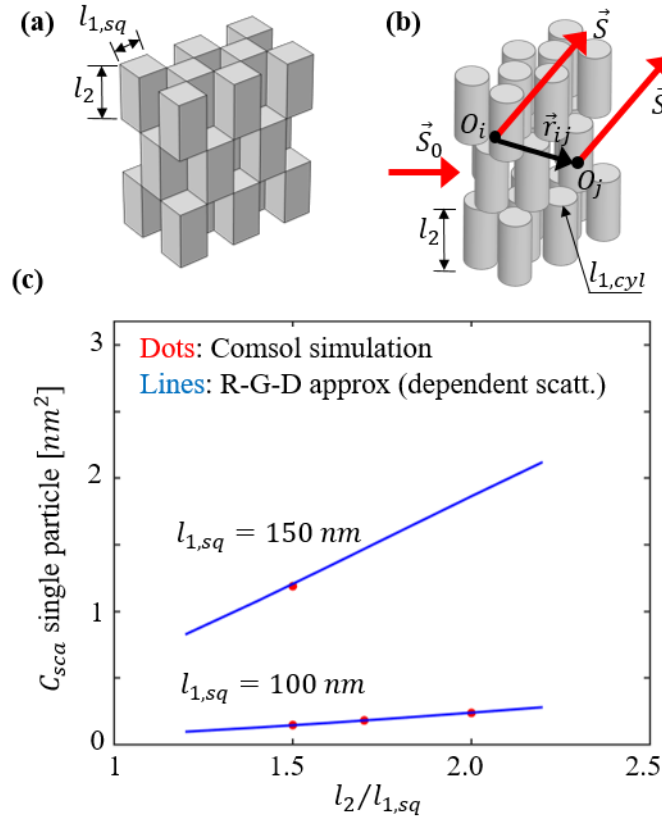
Figure 2-10 (a) COMSOL setup for calculating scattering strength for an array of 23 scatterers in a 3D checkerboard arrangement. (b) Distances and vectors used to calculate the dependent scattering cross-section for the 23 scatterers in (a). $l_{1,cyl} = 1.12 l_{1,sq}$. (c) Effective single scattering cross-sections (total scattering cross-section/23) calculated by COMSOL simulations match very well with calculations with RGD approximation carried out with modification due to dependent scattering (Eq. 2-30). λ =1000nm, $\Delta \eta$ =0.0025.

As the starting powders for the sintering process get smaller, dependent scattering is expected to become non-negligible when the effective distance between two scatterers in the sintered polycrystal is smaller than half the wavelength of incident light.[65,81] In this regime, it is crucial to understand the effects of destructive and constructive interference among waves scattered by each scatterer. This is accounted for by multiplying an additional scatter-angle-dependent factor with the scattered intensity, which was earlier calculated for an individual scatterer using the RGD approximation. Following Prasher[82] the contribution of each of N discrete grains is added up using

$$H(\theta,\phi)=1+\frac{1}{N}\sum_{i=1,i\neq j}^{N}\sum_{j=1}^{N}\cos\left(2\pi\vec{r}_{ij}\cdot\left(\vec{S}-\vec{S}_0\right)\right)$$

(2-29)

where $\vec{r}_{ij}$ is the displacement vector between the scatterers, N is the total number of scatterers, (θ, ϕ) are the angles of the outgoing wave in direction $\vec{S}$, and $\vec{S} - \vec{S}_0$ is the difference between the unit vectors along the incident and the scattered wave as shown in Figure 2-10(b). This angle modifier multiplies the angle dependent scattered intensity $I(\theta, \phi)$ of Eq. (2-13), and the resulting scattering cross-section is calculated as

$$C_{sca} = \frac{1}{I_0} \int_{\theta=0}^{\pi} \int_{\phi=0}^{2\pi} I(\theta, \phi) H(\theta, \phi) r^2 \sin\theta d\theta d\phi \, . \qquad (2\text{-}30)$$

We show the validity of the dependent scattering approach with a calculation for a lattice of 23 cuboids (Figure 2-10(a)) against COMSOL emw simulations in Figure 2-10(c). The two calculations are shown to match very well for two different values of $l_{1,sq}$ and a sweep of aspect ratios. The calculations were limited to small scatterer sizes because of the large aspect ratio. Further discussion of dependent scattering is beyond the scope of this paper. The foundation of dependent scattering calculations laid out in this paper can be used to calculate the expected cross-section when particles with characteristic smallest dimension of less than half a wavelength are used as the starting powders.

Chapter 3 - A 3 Omega Method to Measure an Arbitrary Anisotropic Thermal Conductivity Tensor

This chapter is very closely based on our recent publication[83]

3.1 Introduction

Anisotropic materials are relevant for a wide range of applications such as thermoelectrics,[84–86] high-temperature superconductors,[87] and lightweight heat spreaders.[88] Often the crystallographic orientation of these anisotropic materials can be controlled depending on the material synthesis process,[89–92] while in other cases the orientation is unknown or may vary. However, the vast majority of thermal conductivity measurement techniques are restricted to isotropic materials, or anisotropic materials with principal conductivities aligned parallel with a sample's orthogonal surfaces. Very recently, Feser et al.[25] developed a time-domain thermoreflectance (TDTR) method which can measure an arbitrarily aligned thermal conductivity tensor using offset pump and probe beams, although the absence of a closed form analytic solution necessitates a time-consuming iterative fitting process. No analogous scheme has been developed for the electrothermal-based 3ω method,[22,93] which uses simpler hardware than thermoreflectance-based techniques. Also, the two methods have fundamentally different heating geometries (spot vs. line) making it non-trivial to adapt solutions from the TDTR method.

The 3ω method[22,93] has been extensively used to measure the thermal conductivity in bulk substrates as well as thin films. Briefly, an alternating current source at an angular frequency ω is applied along a heater line deposited on top of the substrate of interest. The resulting Joule heating causes a temperature field fluctuating at the 2nd harmonic. The temperature effect on heater line resistance combined with the 1ω current results in a voltage at 3ω. For semi-infinite substrates in the low frequency limit, the slope of this 3ω voltage with respect to the logarithm of frequency is inversely proportional to the thermal conductivity of the substrate (the "slope method"). The 3ω method has been extended to find the thermal conductivity of thin films using the differential 3ω method.[94,95]

For multi-layered anisotropic substrates with the materials' principal axes aligned with the heater line and free substrate surface, Borca-Tasciuc et al.[26] developed a general solution using integral Fourier transforms.[96,97] They proposed an experimental scheme with multiple heater line widths to extract the thermal conductivity tensor elements for aligned anisotropic layers. They showed that the slope of temperature versus logarithm of frequency is related to the geometric mean of the 2 principal thermal conductivities characteristic to the plane being probed by the 3ω line. Tong & Majumdar[98] developed a data reduction scheme to determine the aligned anisotropy ratio

of thermal conductivity and the interfacial thermal conductance in film on substrate systems. Ramu & Bowers[99] gave a closed form solution for surface temperature in 3ω experiments on an aligned anisotropic substrate with small anisotropy ratios. Finite element method (FEM) simulations and a parallel offset thermometer line were used together to find the cross and in-plane thermal conductivity using an iterative approach in a later work[100].

Thus, all of these previous anisotropic 3ω techniques have been restricted to the aligned case: samples with principal thermal conductivities aligned parallel and perpendicular to the sample surface and heater line. This restriction eliminates the off-diagonal terms from the thermal conductivity tensor and thus simplifies the analysis, but limits the scope of applicability. An experimental procedure which can also identify any off-diagonal terms can also give insight into the orientation and symmetries of the crystal structure as a consequence of the Neumann's Principle, which states that the physical properties of a material are at least as symmetric as its underlying atomic structure.[101]

In this work, we solve the 3ω heating problem for the general case of a substrate with an anisotropic thermal conductivity tensor, which may be arbitrarily oriented with respect to the natural cartesian coordinate system defined by the heater line and free substrate face. We obtain the solution in closed form rather than in an integral form, thereby avoiding the need for time–intensive and potentially non-intuitive numerical fitting to extract the thermal conductivity tensor.

We first derive a closed form solution for the surface temperature profile in the case of an infinitesimally narrow line heater on an arbitrary anisotropic substrate, and show it to be of similar form as that for an isotropic substrate. The solution is extended for a finite-width heater line, and verified using FEM software. Experimental schemes are devised to use measurements of the heater line temperature in the low frequency regime to recover the complete non-diagonal thermal conductivity tensor. We demonstrate these predictions with measurements on mica, a layered anisotropic material.

3.2 The Model Setup

In a cartesian coordinate system, the heat flux vector $\mathbf{Q}$ is related to the thermal gradient vector by Fourier's Law,

$$Q_i = -\sum_j k_{ij} \frac{\partial T}{\partial x_j}$$ (3-1)

and the most general anisotropic thermal conductivity tensor is

$$\mathbf{k} = \begin{bmatrix} k_{xx} & k_{xy} & k_{xz} \\ k_{yx} & k_{yy} & k_{yz} \\ k_{zx} & k_{zy} & k_{zz} \end{bmatrix}.$$ (3-2)

$\mathbf{k}$ is real and symmetric, and it is known[21] that $k_{ii} > 0$ and $k_{ii}k_{jj} > k_{ij}^2$. Thus there are at most 6 independent elements for the most general anisotropic $\mathbf{k}$. We express $\mathbf{k}$ in cartesian coordinates

and require it to be independent of position, so that the analysis applies to layered materials like graphite, but not curved Swiss-roll topologies like a tree trunk.

The basic 3ω setup is depicted in Figure 3-1(a). We define the z axis to lie along the centerline of the heater line, and the x axis as orthogonal to both the heater line and the plane of the sample surface. The alternating current flowing through the heater line causes sinusoidal joule heating at the second harmonic, which is uniform over the heater line length and width. The magnitude of this heater power per unit length is defined as P'. With the usual assumption of an infinitely long heater line, there cannot be any temperature gradients in the z direction which simplifies the problem to the 2-d cross-section shown in Figure 3-1(b). While it is possible to use Feldman's algorithm[96,97] to solve for this heating problem on a multi-layered substrate in a complicated integral form, following a process similar to that used by Feser et al,[25] the focus here is instead on achieving a closed form solution for an arbitrarily anisotropic substrate.

(a)   (b)
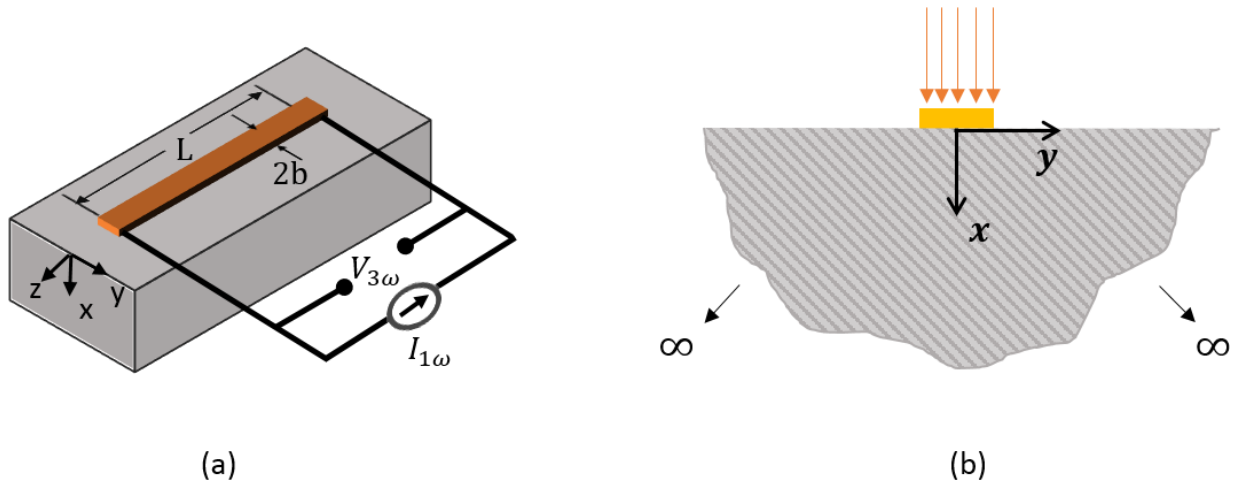
Figure 3-1 a) The 3ω setup and (b) 3ω heater line on an anisotropic semi-infinite substrate. The cross-hatching in (b) is meant to suggest angled layers of an anisotropic material such as graphite or mica.

We first find the solution for an infinitesimally-narrow line heater deposited on such a substrate by using integral transform techniques. This infinitesimal line source is represented as a δ−function heat generation at $x = 0, y = 0$. The time-periodic heat generation is represented using complex Euler notation, whereby the real and imaginary parts of T represent the in-phase and out-of-phase temperature respectively.[102]

The governing equation is

$$k_{xx} \frac{\partial^2 T}{\partial^2 x} + 2k_{xy} \frac{\partial^2 T}{\partial x \partial y} + k_{yy} \frac{\partial^2 T}{\partial^2 y} + P' e^{i2\omega t} \delta(x, y) = CT , \tag{3-3}$$

where C is the volumetric heat capacity. Since the sample is very large in the $\pm y$-direction, suitable boundary conditions are

$$\frac{\partial T}{\partial y} = 0 \text{ and } T = 0 \text{ @ } y \to \pm\infty . \tag{3-4}$$

In the x-direction, the top surface $(x=0)$ is insulated while the bottom surface is far away from the heater line, and thus

$$k_{xx}\frac{\partial T}{\partial x}+k_{xy}\frac{\partial T}{\partial y}=0 \ @\ x=0, \tag{3-5}$$

$$\frac{\partial T}{\partial x}=0 \ \text{and}\ T=0 \ @\ x\to\infty. \tag{3-6}$$

Exploiting the known 2ω forcing of this linear system, the time dependence of the governing equation can be removed by introducing $\overline{T}$ such that

$$T(x,y,t)=\overline{T}(x,y)e^{i2\omega t}, \tag{3-7}$$

where $i=\sqrt{-1}$. The factor of 2 arises because we follow the usual convention of defining ω as the frequency of the electrical current, so that 2ω represents the joule heating. A series of integral and Fourier transforms[103] are used to remove x and y derivatives from the governing equation. Deferring the mathematical details to Appendix 3.7.1, Eqs. (3-28) to (3-37), the solution for $\overline{T}$ is

$$\overline{T}(x,y)=\frac{P'}{\pi\sqrt{k_{xx}k_{yy}-k_{xy}^2}}K_0\left(\frac{q_{xx}\sqrt{k_{xx}k_{yy}x^2+k_{xx}^2y^2-2k_{xx}k_{xy}xy}}{\sqrt{k_{xx}k_{yy}-k_{xy}^2}}\right), \tag{3-8}$$

where K_0 is the modified Bessel function of the second kind and

$$q_{xx}=\sqrt{i2\omega C/k_{xx}} \tag{3-9}$$

Where $|q_{xx}|$ represents the inverse of the penetration depth in the x-direction. As a check, when $k_{xx}=k_{yy}$ and $k_{xy}=0$, the familiar isotropic solution from Cahill[22] is correctly recovered.

Figure 3-2 shows an example of the temperature field resulting from a δ-function line heater, calculated with Eq. (3-8). The argument of Eq. (3-8) also shows that all isotherms are elliptical in shape and obey the relation

$$\sqrt{k_{xx}k_{yy}x^2+k_{xx}^2y^2-2k_{xx}k_{xy}xy}=const, \tag{3-10}$$

where $const$ is a constant determining the temperature of the isotherm. It can be shown that the major and minor axes of these ellipses are aligned along the two principal thermal conductivity directions (proof in Appendix 3.7.2). This result is intuitive since the isotherms are stretched in the direction of least resistance or maximum thermal conductivity. It is also interesting to note that the δ-function line heater is a center of inversion symmetry in the $x-y$ coordinate system. This can also be confirmed mathematically by replacing (x,y) by $(-x,-y)$ in the governing equation and the boundary conditions, which shows that the surface temperature along $x=0$ is symmetric about the line heater even with the presence of cross terms in the thermal conductivity tensor.

31
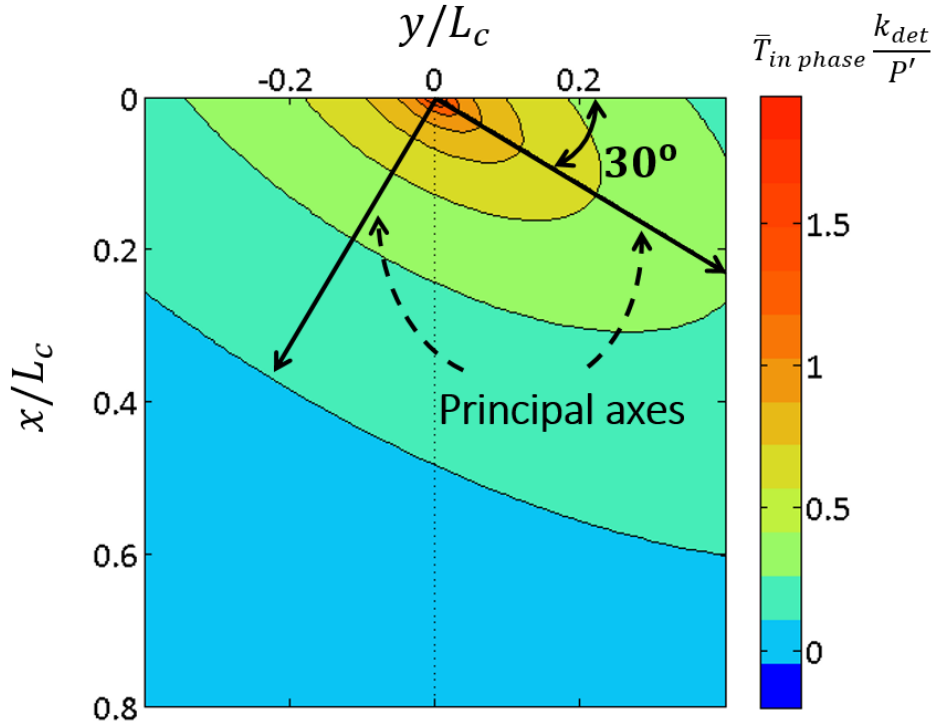
Figure 3-2 Isothermal contours for the in-phase temperature response to a δ−function line heater on an anisotropic substrate. This example uses an anisotropic material with principal thermal conductivities 1 $W/m-K$ and 5 $W/m-K$, rotated by 30° in the clockwise direction so that $\mathbf{k} = \begin{bmatrix} 2 & -\sqrt{3} \\ -\sqrt{3} & 4 \end{bmatrix} W/m-K$ **in the** $x-y$ **coordinate system. We define an effective thermal conductivity,** $k_{\det} = \sqrt{k_{xx}k_{yy} - k_{xy}^2}$, **with its characteristic thermal penetration depth,** $L_c = \sqrt{k_{\det}/2\omega C}$ **which contains the only ω dependence.** $k_{\det}$ **is the square root of the determinant of** $\mathbf{k}$. **A generic heat capacity of** $C = 2\times 10^6$ $J/m^3 - K$ **is also used.**

3.2.1 Finite Heater Width and Average Heater Temperature

The next step in this analysis is to find the surface temperature profile, $T_{surf}(y)$, caused by a finite width heater, as well as the average temperature of this heater line which is what the 3ω voltage measures. The finite width heater is represented as a superposition of δ-function line heaters over the heater line width, leading to a convolution integral,

$$T_{surf}(y) = \frac{1}{2b}\int_{-b}^{b}\overline{T}(0, y-y')dy' = \frac{1}{2b}\int_{-b}^{b}\frac{P'}{\pi\sqrt{k_{xx}k_{yy} - k_{xy}^2}}K_0\left(\frac{q_{xx}k_{xx}|y-y'|}{\sqrt{k_{xx}k_{yy} - k_{xy}^2}}\right)dy', \quad (3\text{-}11)$$

where the latter form follows from Eq. (3-8) after setting x=0 to represent the surface. As mentioned after Eq. (3-8), for a δ-function line heater the temperature solutions for anisotropic and isotropic substrates have very similar forms. It turns out that one can map the integral in Eq. (3-11) onto the corresponding integral for an isotropic substrate using a change of variables. As detailed in Appendix 3.7.1, Eqs. (3-38) to (3-39), in this way we can obtain the surface

temperature for an anisotropic substrate analogous to isotropic solutions found by Duquesne et al.[104] The result here is

$$T_{surf}(y) = \frac{P'}{4\sqrt{k_{xx}k_{yy} - k_{xy}^2}}\left[(1-Y)\Xi\left(\sqrt{i\Omega(1-Y)^2}\right) + (1+Y)\Xi\left(\sqrt{i\Omega(1+Y)^2}\right)\right], \qquad (3\text{-}12)$$

where $\Omega = \dfrac{b^2 2\omega C}{\sqrt{k_{xx}k_{yy} - k_{xy}^2}}$, $Y = \dfrac{y}{b}$, and $\Xi(y) = K_0(y)L_{-1}(y) + K_1(y)L_0(y)$ where K_n and L_n are

the nth order modified Bessel function of the second kind and Struve function[105] respectively. Similarly, the average of T_{surf} over the heater line width, $\langle T \rangle$, can also be found by using a change of variables to adapt the known isotropic solution[104] for this anisotropic problem (Appendix 3.7.1, Eqs. (3-40) to (3-41)). The solution can be represented in terms of the Meijer-G function G_{24}^{22} as[104,106]

$$\langle T \rangle = \frac{-iP'}{4\pi\Omega\sqrt{k_{xx}k_{yy} - k_{xy}^2}} G_{24}^{22}\left(i\Omega \,|_{1,1,1/2,0}^{1,3/2}\right). \qquad (3\text{-}13)$$

Equation (13) is plotted in Figure 3-3, along with low- and high-frequency asymptotic forms. The high-frequency limit of Eq. (3-13) is

$$\langle T \rangle = \frac{P'}{2k_{xx}bq_{xx}}, \qquad (3\text{-}14)$$

which is the well known 1-D planar heating result where temperature gradients are present only in the x-direction.

Of particular importance is the low frequency limit, because the simplicity and accuracy of the low-frequency slope method of 3ω data analysis is already well established for isotropic and aligned aniostropic substrates. Using the small argument approximation $K_0(z) \approx -\ln(z) - \gamma + \ln(2)$, we find the low-frequency limit of Eq. (3-13) as

$$\langle T \rangle = \frac{P'}{\pi\sqrt{k_{xx}k_{yy} - k_{xy}^2}}\left\{-\frac{1}{2}\ln\left(\frac{b^2 2\omega Ck_{xx}}{k_{xx}k_{yy} - k_{xy}^2}\right) + \frac{3}{2} - \gamma - i\frac{\pi}{4}\right\}, \qquad (3\text{-}15)$$

where $\gamma \approx 0.5772$ is the Euler constant.
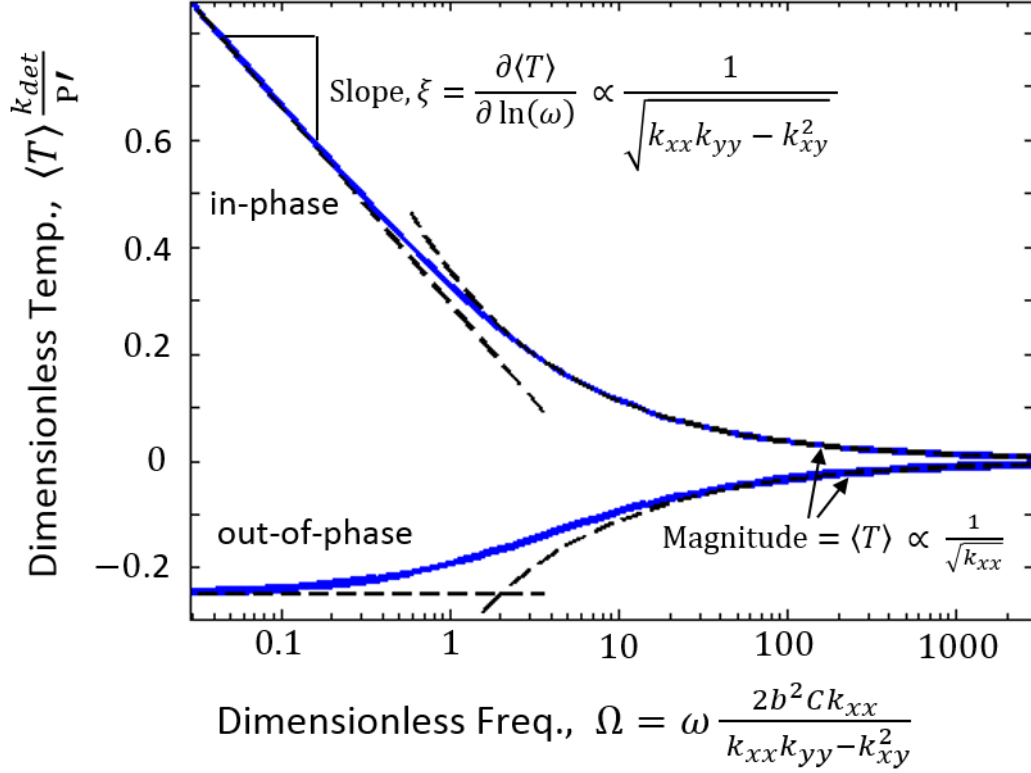
Figure 3-3 Amplitude of in-phase and out-of-phase temperature oscillations of a finite-width heater line, as a function of heating current frequency (Eq. (3-13)). $k_{det} = \sqrt{\det(\mathbf{k})} = \sqrt{k_{xx}k_{yy} - k_{xy}^2}$. **In the low frequency limit, the slope ξ of the in-phase temperature rise is inversely proportional to k_{det}.** **In the high frequency limit, the magnitude of both in-phase and out-of-phase temperature rise is inversely proportional to $\sqrt{k_{xx}}$. The dashed lines depict the asymptotic forms given in the main text (Eqs. (3-14) and (3-15)).**

Equation (15) is one of the major results of this paper and is used extensively in the experimental section below. Its slope, $\xi = \partial \langle T \rangle / \partial \ln(\omega)$, is inversely proportional to

$$k_{det} = \sqrt{k_{xx}k_{yy} - k_{xy}^2} = \sqrt{\det(\mathbf{k})}, \qquad (3\text{-}16)$$

with the proportionality constant $-P'/2\pi$. Importantly, we recognize k_{det} as the square root of the determinant of this 2-d thermal conductivity tensor, and as such it is invariant under rotation in the xy plane. Hence, changing the orientation of heater line by rotating it around its longitudinal (z) axis must always give the same slope value, and thus cannot not yield any additional information to separate out the values of k_{xx}, k_{yy} and k_{xy}. On the other hand, Eq. (3-15) shows that the magnitude of temperature fluctuations does depend on the orientation of heater line. This fact will be exploited later to extract the individual thermal conductivity tensor elements.

Finally, the RMS 3ω voltage is related to the 2ω temperature oscillation by[22,93]

$$V_{3\omega} = -\frac{1}{4}\alpha R I_{1\omega} \langle T \rangle. \tag{3-17}$$

Here $I_{1\omega}$ is the RMS value of the AC source, R is the heater line resistance at zero current, and α is the temperature cofficient of resistance, all of which are easily determined experimentally making it straightforward to switch between $V_{3\omega}$ and $\langle T \rangle$.

3.3 Numerical Validation

To numerically validate our key analytical results, Eqs. (3-12), (3-13) and (3-15), simulations of a 3ω heating problem in 2-d were carried out using a commercial FEM package (COMSOL). To set up the heat conduction equations in the frequency domain, we used user-defined equations in the Coefficient Form PDE module. As a test case we use the same **k** and *C* described in the caption of Figure 3-2, with additional simulation paramters $b = 5\mu m$ and $P' = 3W/m$. For these parameters, the low frequency regime $(|q_{xx}|b << 1)$ and the high frequency regime $(|q_{xx}|b >> 1)$ correspond approximately to $\omega < 10^3 \, rad/s$ and $\omega > 4 \times 10^5 \, rad/s$, respectively.
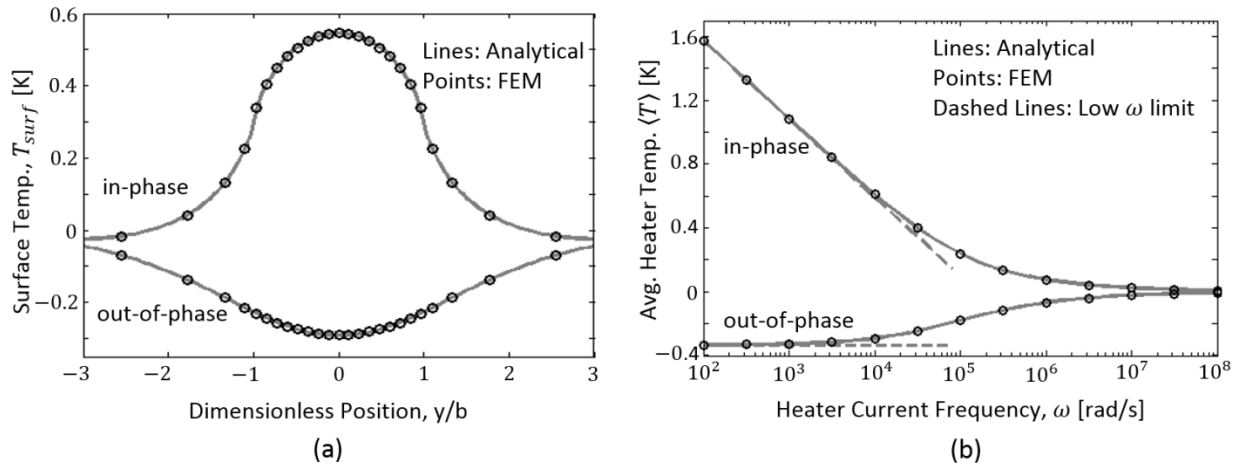
Figure 3-4 FEM validation of closed form analytic solutions (Eqs. (3-12), (3-13) and (3-15)) for a general anisotropic sample. The figures compare analytical (lines) and FEM (points) results for (a) surface temperature at an intermediate frequency, $\omega = 2 \times 10^4 \, rad/s$ **, and (b) average heater line temperature over a wide frequency range. The dashed lines in (b) represent the low frequency limit of Eq. (3-13). Joule heating frequency is** 2ω **. k and C as in Figure 3-2, with other parameters** $b = 5\mu m$ **and** $P' = 3W/m$ **.**

The validation is carried out in two steps. First, to check Eq. (3-12) in the most general case, we choose a mid-frequency regime (penetration depth comparable to heater line width: $|q_{xx}|b = 1$, corresponding to $\omega = 2 \times 10^4 \, rad/s$ and Ω=0.8), rather than either extreme frequency limit. To eliminate the effects of the far-field boundary conditions of the original semi-infinite problem in a finite-sized FEM domain, care is taken to ensure the sample extents in $+x$ and $\pm y$ directions are much larger than the thermal wavelengths, confirmed by verifying that the same simulation results are obtained for both adiabatic and isothermal far-field boundary conditions. Figure 3-4(a) shows the comparison of surface temperatures obtained from our analytical solution (Eq.

(3-12): lines) and FEM simulations (points). The agreement is excellent, including the detailed profile near and within the heater line itself.

Second, to validate our solutions for $\langle T \rangle$ at arbitrary frequency, Eq. (3-13), and in the low frequency limit, Eq. (3-15), we performed FEM simulations spanning a wide frequency range. As shown in Figure 3-4(b), the results from FEM simulations (points) again agree very well with both analytical results (solid and dashed lines), thus further validating the analytical solutions.

3.4 Experimental Schemes and Proof-of-Concept

In this section we present two experimental schemes to use the low frequency solution of Eq. (3-15) to measure the thermal conductivity tensor of a substrate. The underlying focus is on the closed form solution to avoid nonlinear numerical fitting processes. Both approaches begin using the slope method (Eq. (3-15), Figure 3-3) to find the thermal conductivity determinant in the natural $x-y$ coordinate system defined by the heater line and sample surface. Since rotation of the heater line around its longitudinal axis will give exactly the same measured slope, the schemes described below also use the magnitude of $\langle T \rangle$ to separate out the components of k_{ij}.

(a)   (b)
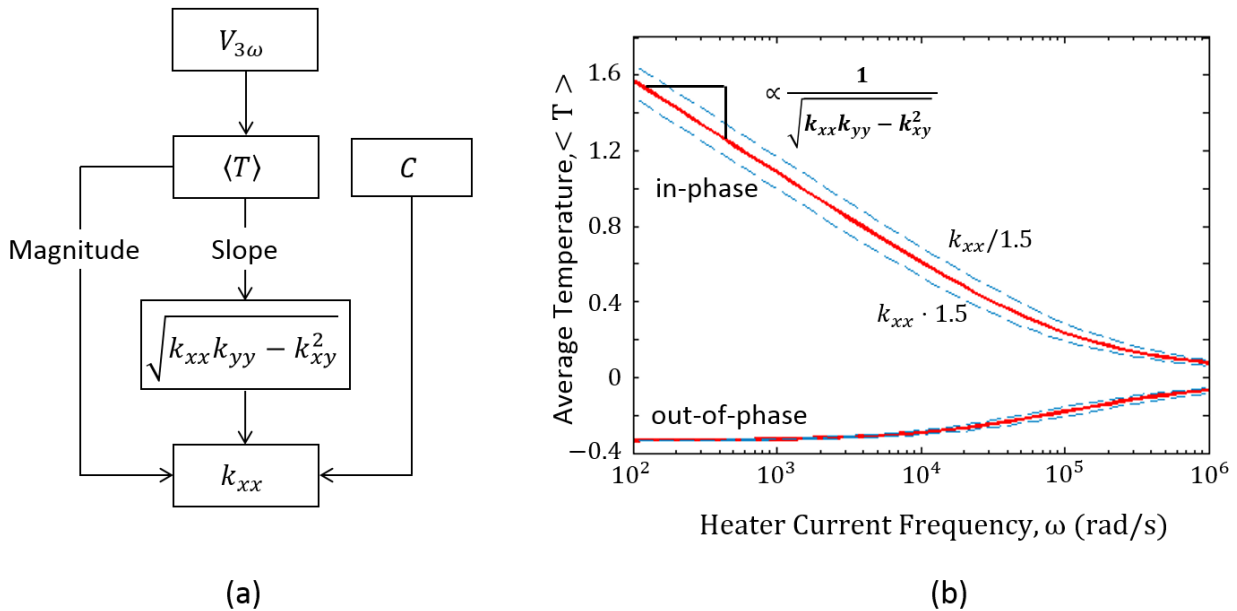
Figure 3-5 (a) Process to determine k_{xx} **from the in-phase 3ω voltage measurements in the low frequency regime. The slope method gives** $k_{\text{det}} = \sqrt{k_{xx}k_{yy} - k_{xy}^2}$ **, which is used along with the in-phase magnitude and the sample's heat capacity to determine** k_{xx}**. (b) Effect of changing** k_{xx} **while keeping** k_{det} **constant. For the in-phase curve at low frequency, the fixed determinant ensures constant slope while the magnitude depends on** k_{xx}**. Simulation parameters as in Figure 3-4.**

Scheme 1

36

Thus k_{det} from the slope method can be used with C to calculate k_{xx} from the low frequency temperature response. This relationship is further clarified in Figure 3-5 (b): if k_{xx} is varied while keeping the determinant constant, then the magnitude of the in-phase $\langle T \rangle$ varies while its low-frequency slope remains constant.

Figure 6 shows an example layout of heater lines to determine the elements of $\mathbf{k}$. Heater lines 1 and 2 can be used to characterize the $x-y$ plane. In the low frequency limit, $\langle T \rangle$ for both heater lines will give the same slope value (determinant) but different magnitudes. Combining this information with C allows k_{xx} and k_{yy} to be calculated. It is then possible to extract the magnitude of the off-diagonal term, $|k_{xy}|$ from the determinant.

(a)   (b)
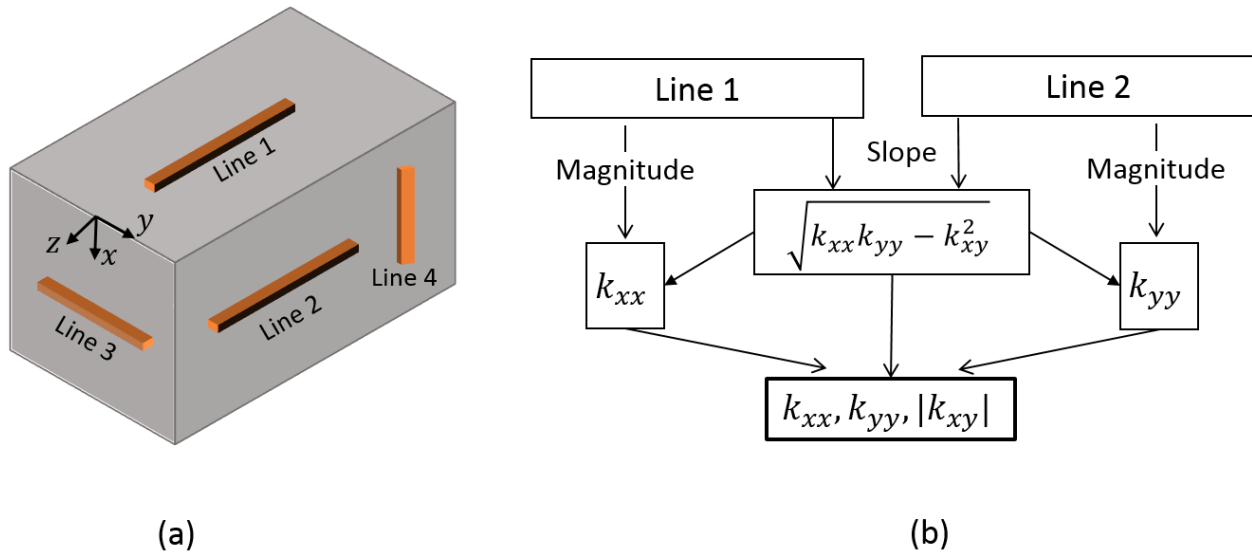
Figure 3-6 (a) To measure the thermal conductivity tensor for the $x-y$ **plane of a given substrate, low frequency measurements from heater lines 1 and 2 can be used. (b) As shown in the flowchart, both lines will give the same slope** $\partial\langle T \rangle / \partial \ln(\omega)$**, while their** $\langle T \rangle$ **magnitudes depend on the orientation of the heater line as well as** *C***. Similarly, low frequency 3ω measurements from heater lines 1-4 on orthogonal faces in (a) can give the full 3-d thermal conductivity tensor. These approaches determine the magnitude though not sign of the off-diagonal terms such as k$_{xy}$ (see text).**

To determine the sign of k_{xy}, a third non-co-planar heater line can be used. Such a line is labeled γ in Figure 3-7, deposited on a face tilted by some angle θ with respect to face 1. Low frequency 3ω measurements from line γ will yield $k_{x'x'}$, which can be related to the tensor elements in the $x-y$ coordinate system through standard tensor rotation rules ,

$$k_{x'x'} = k_{xx} \cos^2(\theta) + k_{xy} \sin(2\theta) + k_{yy} \sin^2(\theta). \tag{3-18}$$

Using Eq. (3-18), k_{xy} now can be determined from the values of k_{xx}, k_{yy}, and $k_{x'x'}$ which are known from heater lines 1, 2, and γ respectively. Note that lines 1 and 2 need not be on orthogonal faces for this method. Any set of parallel (z-oriented) heater lines on 3 non-co-planar surfaces will give a complete set of equations to solve for the 3 elements of the 2-d **k** tensor. A line at $\theta = 45^o$ would maximize the sensitivity to k_{xy}. Finally, multiple heater lines 1-4 on orthogonal faces will be required to find the full 3-d thermal conductivity tensor (Figure 3-6(a)) if only the magnitudes of the off-diagonal terms are needed, while additional heater lines on non-co-planar surfaces similar to line γ in Figure 3-7 can be used to determine their signs.
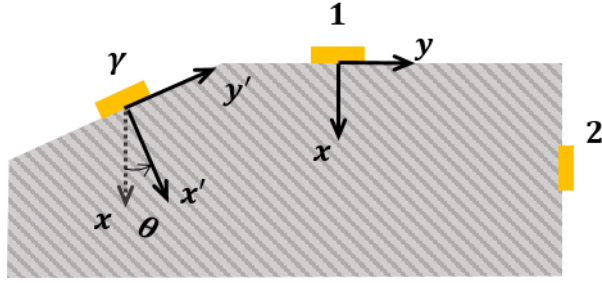
Figure 3-7 To fix the sign of k_{xy} after determining $\left|k_{xy}\right|$ from Figure 3-6, an additional heater line γ is required on a surface at some other angle. θ is defined as the angle between the x' and x axes, measured in the counter-clockwise direction as shown. Using transformation rules (Eq. (3-18)), the effect of k_{xy} is seen in $k_{x'x'}$ in the new $x'-y'$ coordinate system. $k_{x'x'}$ can be measured using this new heater line, following the approach outlined in Figure 3-5.

Scheme 2

The second scheme is differential and eliminates the heater line width and substrate heat capacity from the calculation, as long as their values are identical from sample to sample. Manipulating Eq. (3-15) and taking b and C as constant gives

$$\frac{\langle T\rangle_{line2}(\omega_2)}{\xi_2} - \frac{\langle T\rangle_{line1}(\omega_1)}{\xi_1} = \ln\left(\frac{\omega_2}{\omega_1} \times \frac{k_{yy}}{k_{xx}}\right) \tag{3-19}$$

and

$$\frac{\langle T\rangle_{line3}(\omega_3)}{\xi_3} - \frac{\langle T\rangle_{line1}(\omega_1)}{\xi_1} = \ln\left(\frac{\omega_3}{\omega_1} \times \frac{k_{zz}}{k_{xx}} \times \frac{k_{xx}k_{yy} - k_{xy}^2}{k_{zz}k_{xx} - k_{zx}^2}\right), \tag{3-20}$$

where $\xi_n = \dfrac{\partial\langle T\rangle_{line-n}}{\partial\ln(\omega)}$, with n identifying the heater line orientation as per Figure 3-6. Here ω_n refers to any particular frequency used for the corresponding heater line's voltage, and for convenience one might use $\omega_1 = \omega_2 = \omega_3$. Since the thermal conductivity determinants in Eq.

(3-20) are already known from slope measurements, it is now a direct calculation to find the ratio k_{xx}/k_{yy} using lines 1 & 2, and k_{xx}/k_{zz} using lines 1 & 3.

Note that this second scheme does not directly yield the off-diagonal elements of **k**, but they can be found using additional heater lines at different orientations. For example, using the differential scheme between heater lines 1 and γ in Figure 3-7 measures the ratio

$$\frac{k_{x'x'}}{k_{xx}} = \cos^2(\theta) + \frac{k_{xy}}{k_{xx}}\sin(2\theta) + \frac{k_{yy}}{k_{xx}}\sin^2(\theta). \qquad (3-21)$$

Combining this additional information with the known values of k_{det} and k_{yy}/k_{xx}, it is straightforward algebra to obtain all three of k_{xx}, k_{yy}, and k_{xy}.

3.5 Experiments with Mica

3.5.1 Concept
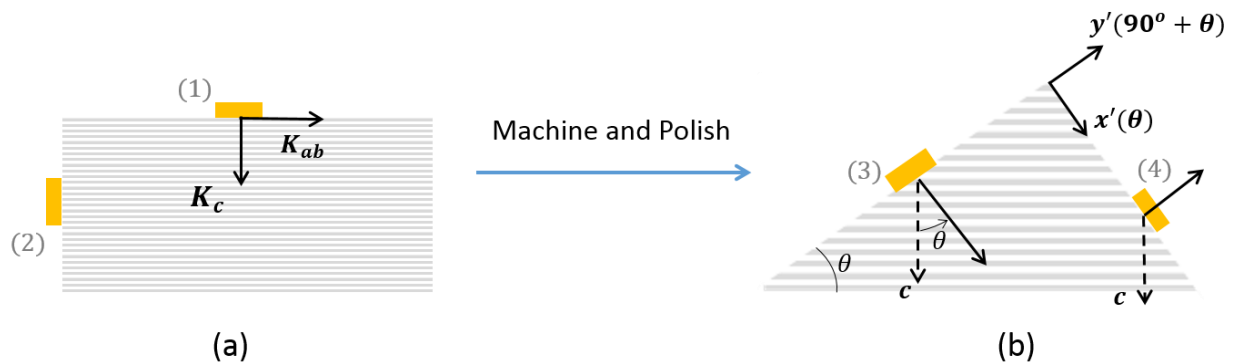
Figure 3-8 Schematics of the (a) aligned and (b) angled samples used for experiments. k_θ **is an effective thermal conductivity normal to the heater line, as defined in (Eq. (3-22)). In our experiments, the four different heater line orientations are:** $\left(1 \to 0^0, 2 \to 90^0, 3 \to 30^0, 4 \to 120^0\right)$.

To demonstrate the major analytical results above, a self-consistency check was carried out with experiments on muscovite mica sheets, which was chosen for its moderate thermal conductivity anisotropy ratio at room temperature.[107] To facilitate sample fabrication we chose 0.25" thick sheets (McMaster-Carr, product ID 8779K52). According to the vendor, the mica layers used to make these sheets are shaved directly from the natural mineral, layered horizontally, and then pressed into the required thickness. Mica is a silicate with a monoclinic crystal structure that is characterized by layered basal planes stacked in the c-axis direction of the unit cell. Thermal conductivity experiments[107,108] on muscovite mica sheets usually presume an isotropic thermal conductivity in the ab plane, which is consistent with elastic moduli[109–111] measurements that show a very weak or non-existent anisotropy in the ab plane of the silicate layers. Therefore, we assume the principal thermal conductivities K_{ab}, K_{ab}, and K_c, along the *a*-, *b*-, and *c*-axis directions, respectively. As shown in Figure 3-8, we aim to characterize a cross-section of the layered material, and prepare two samples accordingly. The first sample is the aligned case

(Figure 3-8(a)), with K_c and K_{ab} aligned perpendicular and parallel to the surface, and the 3ω experiments involve measuring these two principal values.

The second sample is angled, to represent an arbitrary orientation rotated around the z axis. We introduce off-diagonal elements by machining orthogonal faces at angles θ and $90^o + \theta$ to the c direction (Figure 3-8 (b)). For simplicity in presenting results from multiple orientations, for the rest of this section it shall prove convenient to refer to the new coordinate system (x', y') as $(\theta, 90^0 + \theta)$. Since θ is measured with respect to the c-axis of the material, for a surface of any θ the corresponding $k_{x'x'}$ value is given straightforwardly by Eq. (3-18) with $k_{xy}=0$. In the notation of the present section we denote $k_{x'x'}$ by k_θ and have

$$k_\theta = K_c \cos^2 \theta + K_{ab} \sin^2 \theta. \tag{3-22}$$

Similarly, we shall denote the off-diagonal term $k_{x'y'}$ as $k_{\theta\, 90^o + \theta}$, which is easily shown to be

$$k_{\theta\, 90^o + \theta} = \left(K_{ab} - K_c\right) \cdot \sin \theta \cos \theta. \tag{3-23}$$

Thus for any rotated (x', y') coordinate system, the new $\mathbf{k}$ tensor is expressed as $\begin{bmatrix} k_\theta & k_{\theta\, 90^o + \theta} \\ k_{\theta\, 90^o + \theta} & k_{90^o + \theta} \end{bmatrix}$. The measured k_{ij} values in this coordinate system should match those calculated from Eqs. (3-22) and (3-23). In our experiments $\theta = 30^o$. To determine the off-diagonal term in the $(\theta, 90^0 + \theta)$ coordinate system, we exploit the heater lines in the aligned configuration of Figure 3-8(a) by following the scheme described in Figure 3-7. The heater lines 1 and 2 in Figure 3-8(a) now correspond to parallel but non-co-planar heater lines at angles -30º and 60º in the (x', y') system of Figure 3-8(b). We can use either of these 2 lines now to measure the full thermal conductivity tensor in the (x', y') or $(\theta, 90^0 + \theta)$ coordinate system.

3.5.2 Results

All mica surfaces were polished using diamond lapping tools. A total of 16 heater lines were then deposited on several different samples, always at one of the four angles indicated in Figure 3-8, with the labeling $\left(1 \rightarrow 0^0, 2 \rightarrow 90^0, 3 \rightarrow 30^0, 4 \rightarrow 120^0\right)$. Gold heater lines nominally $1.5\,mm$ long, $60\,\mu m$ wide, and $200\,nm$ thick, with a $10\,nm$ chromium adhesion layer, were patterned by evaporation through a shadow mask. The temperature coefficient of resistance was calibrated separately for every line. The 3ω measurements were performed in ambient air at a temperature of 27 ± 3 ºC.

Invariance of the determinant. We first check the major theoretical prediction from (Eq. (3-15)) that the slope method for all heater lines should give the square root of the thermal conductivity determinant, k_{det}, which is expected to be a constant for all heater orientations since determinants are invariant upon rotation. This prediction is verified in Figure 3-9. For each orientation we measured between 3 and 5 independent heater lines, with the resulting slope-

values of thermal conductivity shown by the gray columns. The average for each orientation is indicated by the four blue solid lines. These averages indeed give nearly the same value, with a range from 0.79 to 0.86 W/m-K, in good agreement with the average from all 16 independent experiments (dashed line) of 0.81 W/m-K. This confirms the determinant is independent of heater line rotations about its axis. We also note that the overall standard deviation of ±0.10 W/m-K, and standard error of the mean of ±0.02 W/m-K (where SEM = SD/$\sqrt{N}$), are much smaller than the observed differences between K_{ab} and K_c as discussed later and shown in Figure 3-10.
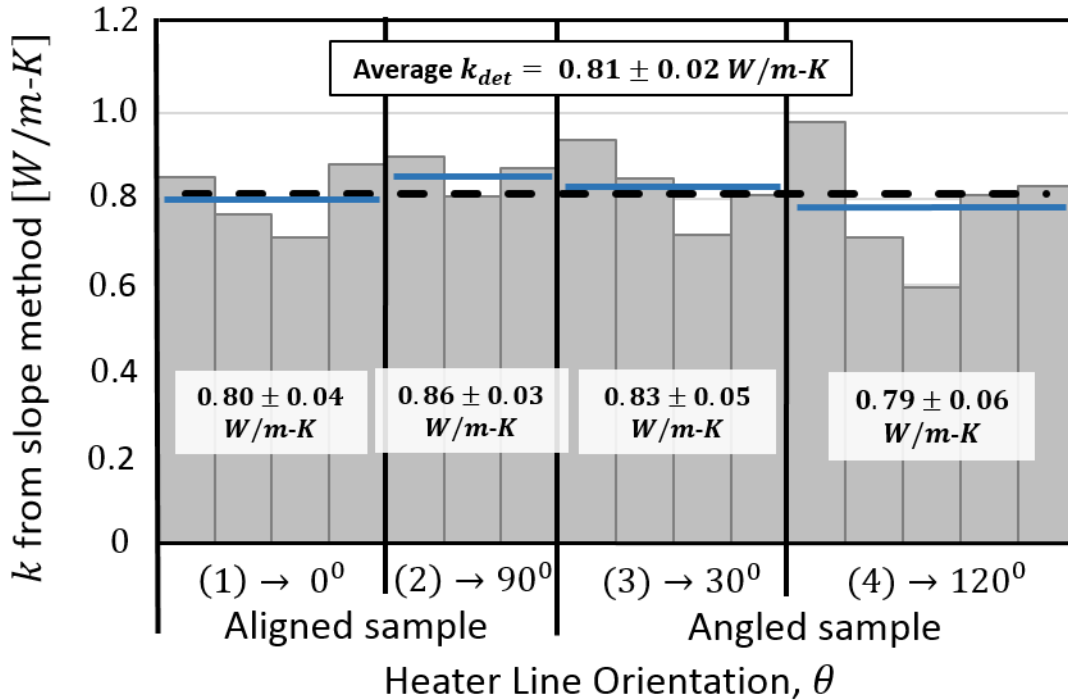
Figure 3-9 Experimental confirmation of the invariance of thermal conductivity determinant, obtained using the slope method. Each column represents the measured k_{det} of a different microfabricated heater line (N=16 total), grouped into four heater orientations. The aligned sample had $\theta = 0^{o}$ and 90° while the angled sample which exercises an arbitrary anisotropy had $\theta = 30^{o}$ and 120°. The average value for each orientation is depicted by the solid blue line, with the mean ± SE-Mean values given on the plot. Finally, the average of all 16 measurements is given by the dashed black line. The agreement between the four orientations (range 0.79 - 0.86 W/m-K) is within the overall scatter of ±0.10 W/m-K (S.D.), confirming the constancy of the determinant to within noise.

Scheme 1: k elements. We now evaluate the individual tensor elements for both the aligned and angled samples. The first scheme (depicted in Figure 3-5 and Figure 3-6) requires the volumetric heat capacity $C = \rho c$, which was calculated using the measured gravimetric c (using differential scanning calorimetry: TA Instruments, Model Q20) and density ρ (using a geometric calculation of volume, confirmed by a water displacement method). The measured ρ of $2200\ kg/m^3 \pm 1.5\%$ is 18% lower than literature[112], which may be due to imperfect pressing of the individual shaved layers in these industrial samples. The measured c is $804\ J/kg - K \pm 2.2\%$ (average of 5 samples

± SE-Mean), which is around 8% lower than reported for a single crystal specimen[113] ($876\ J/kg - K$); since we see no reason why c should have been affected by the sample manufacturing process, we use the average of these two values. The resulting volumetric C is $1.85 \times 10^6\ J/m^3 - K$ at room temperature, which is around 20-25% lower than reported previously for a single crystal specimen[112–114] due mainly to the lower density. The low-frequency 3ω voltage data gives the thermal conductivity perpendicular to the heater line, k_θ. The resulting measurements are shown in Figure 3-10.
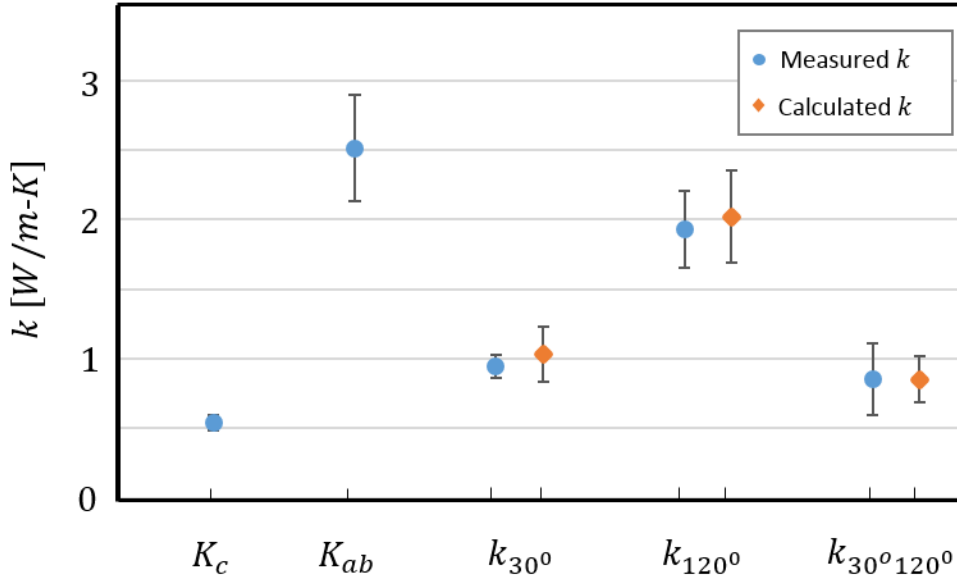
Figure 3-10 Effective thermal conductivity as a function of direction in mica samples. Blue circles show directly measured $\mathbf{k}$ -tensor elements. K_c and K_{ab} are the principal values measured in the aligned samples, while k_{30^0}, k_{120^0} and $k_{30^0 120^0}$ are measured in the angled samples. The calculated values (orange diamonds) for the angled sample are found by applying the tensor transformation rules of Eqs. (3-22) and (3-23) to the measured K_c and K_{ab}. Error bars represent standard error of the mean, evaluated using measurements from multiple heater lines.

The first two values in Figure 3-10 are the measured principal thermal conductivities, K_c and K_{ab}, extracted from heater line orientations 1 and 2, respectively. Using these principal values and the transformation rules of Eqs. (3-22) and (3-23), the tensor elements for the angled sample can be estimated, as shown by the orange diamonds. These are checked against direct measurements using heater lines 3 and 4 which give the diagonal elements, k_{30^o} and k_{120^o}, respectively (blue circles). Lines 3 and 4 can only measure $\left| k_{30^o 120^0} \right|$ following the flowchart in Figure 3-6(b), and removing the sign ambiguity requires another additional line as noted in Figure 3-7. Here we report the average of values obtained from the 2 sets of 3 non-co-planar heater line configurations, namely {1,3,4} and {2,3,4} of Figure 3-8. Figure 3-10 shows that the

calculated values of all three tensor elements for the angled sample are in good agreement with the directly measured elements, well within the standard errors of the means.

We see significant scatter in the thermal conductivity values reported in Figure 3-10. One obvious potential source of uncertainty is sample-to-sample variability since these are industrial grade samples synthesized from the natural mineral. We also note some more fundamental sensitivity issues which are intrinsic to this method, where the sensitivity of $V_{3\omega}$ to a parameter β is defined following Gundrum et al.,[115]

$$S_\beta = \frac{\partial \ln(V_{3\omega})}{\partial \ln(\beta)} . \tag{3-24}$$

Consider this sensitivity to the various experimental parameters in the low frequency regime. Evaluation of Eq. (3-15) shows that $V_{3\omega}$ is just as sensitive to C as it is to k_θ, and twice as sensitive to b as to k_θ. These samples exhibit a b variation of around $\pm 10\%$ which may be attributed to the simple shadow masked patterning process. We also note that the sensitivity of the slope to k_{det} is always 1, but over the frequency range of interest the sensitivity of $V_{3\omega}$ to k_θ is only around 0.2; therefore it would not be surprising if the scatter (SE-Mean) in Figure 3-10 were up to ~5 times larger than in Figure 3-9.

Scheme 2: Ratios. Finally, to bypass the uncertainties in heater line width and heat capacity, we consider the second experimental scheme which uses a differential approach and deals in conductivity ratios. From the 7 lines deposited on the 2 aligned surfaces (heater line orientations 1 and 2), Eq. (3-20) gives $K_{ab}/K_c = 4.64 \pm 0.48$. Following this, we do two consistency checks. We first compare k_{120^o}/k_{30^o} measured directly by the differential method on the angled sample (Figure 3-8(b)) with the expected value of k_{120^o}/k_{30^o} from applying tensor transformation rules to K_{ab}/K_c which gives

$$k_{120^o}/k_{30^o} = \frac{\cos^2 120^o + (K_{ab}/K_c)\sin^2 120^o}{\cos^2 30^o + (K_{ab}/K_c)\sin^2 30^o} , \tag{3-25}$$

yielding the estimate $k_{120^o}/k_{30^o} = 1.95 \pm 0.07$. This compares favorably (14% difference) with the ratio measured directly by the differential method (Eq. (3-20)) on heater lines 3 and 4, which is $k_{120^o}/k_{30^o} = 2.22 \pm 0.25$.

Similarly, for the off-diagonal element of the angled sample, tensor algebra gives

$$k_{30^o 120^o}/k_{30^o} = \frac{\cos 30^o \sin 30^o ((K_{ab}/K_c)-1)}{\cos^2 30^o + (K_{ab}/K_c)\sin^2 30^o} , \tag{3-26}$$

which using the measured K_{ab}/K_c predicts $k_{30^o120^o}/k_{30^o} = 0.82 \pm 0.06$. This again compares favorably with the directly measured value $k_{30^o120^o}/k_{30^o} = 0.81 \pm 0.21$, which is the average value obtained by applying Eq. (3-21) to the set of lines {1,3,4} and {2,3,4}.

Lastly, using the measured $k_{30^o120^o}/k_{30^o}$ and k_{120^o}/k_{30^o} from the differential scheme, and the average k_{det} from Figure 3-9, we can evaluate the complete thermal conductivity tensor in the $(30^o,120^o)$ coordinate system:

$$\mathbf{k} = \begin{bmatrix} 0.65 & 0.53 \\ 0.53 & 1.45 \end{bmatrix} W/m - K \tag{3-27}$$

These tensor elements are systematically smaller than those obtained from the first scheme (last 3 blue circles of Figure 3-10). The square root of the thermal conductivity tensor determinant, $k_{det} = \sqrt{k_{30^o}k_{120^o} - k_{30^o120^o}^2}$ in Figure 3-10 is $1.05 \pm 0.29 \, W/m - K$, which is higher than k_{det} predicted from the slope method in Figure 3-9. This indicates possible errors in b and C, and the relatively low sensitivity to the thermal conductivity tensor elements in the first scheme as compared to the sensitivity to k_{det} in the slope method. On the other hand, the differential scheme which is independent of b and C works around uncertainties in measurements, thus confirming its advantage over the first scheme. This leads to a tighter scatter in the ratios reported by the differential method, which has inherently better sensitivity. Measuring k_{det} from the slope method, and the $\mathbf{k}$-tensor element ratios from the differential scheme, ensures good sensitivity at each step, and should yield the most accurate final results for the individual k_{ij}.

3.6 Summary

We report an analytic closed form solution for the 3ω heating problem on a substrate with arbitrary anisotropy in cartesian coordinates. The major analytical results are Eq. (3-13) and especially its low-frequency limit, Eq. (3-15). The extension of the familiar slope method gives the square root of the determinant of the thermal conductivity tensor, which is invariant upon rotation around the axis of the heater line. The magnitude of the in-phase temperature rise depends on this determinant as well as the effective thermal conductivity perpendicular to heater line, k_{xx} in Figure 3-1 or k_θ in Figure 3-8(b). The analytical solutions have been validated using FEM.

Two experimental schemes were devised to isolate the thermal conductivity tensor elements using multiple heater lines on orthogonal faces, and demonstrated with experiments on industrial mica sheets. The first scheme can measure all the tensor elements, though it requires the volumetric heat capacity and gives only the absolute value of the off-diagonal elements. The second scheme is differential and does not need the heat capacity or heater line width, and gives

anisotropy ratios. One additional heater line deposited on a non-orthogonal face (as in Figure 3-7) is required to fix the sign of the off-diagonal elements in the first scheme, and the specific tensor values rather than ratios in the second scheme. For our data set of 16 heater lines at 4 orientations, the first scheme over-predicts the thermal conductivity tensor elements, attributed to uncertainties in C and b values, while the differential scheme works around these issues.

To best combine the strengths and sensitivities of the various schemes, we recommend using the slope method to measure k_{det} and the differential scheme to measure k_{ij} ratios, information which can be combined to specify the complete and arbitrary tensor **k**.

3.7 Appendices

3.7.1 Closed form solution for the 3ω problem on an anisotropic substrate

Delta-Function heater line

We present the details of the derivation beginning from Eq. (3-7). The equations are simplified by introducing the ratios $\varepsilon_{yy} = k_{yy}/k_{xx}$ and $\varepsilon_{xy} = k_{xy}/k_{xx}$. Following a standard approach,[103] we remove the y derivative by using the Fourier transform pairs $\tilde{T}(x,\gamma) = \int_{-\infty}^{\infty} e^{i\gamma y'}\overline{T}(x,y')dy'$ and $\overline{T}(x,y) = \frac{1}{2\pi}\int_{-\infty}^{\infty} e^{-i\gamma y}\tilde{T}(x,\gamma)d\gamma$. After applying this transform and Eq. (3-7) to the governing Eq. (3-3) we have

$$\frac{\partial^2 \tilde{T}}{\partial^2 x} - 2i\gamma\varepsilon_{xy}\frac{\partial \tilde{T}}{\partial x} - \gamma^2\varepsilon_{yy}\tilde{T} + \int_{-\infty}^{\infty}\frac{P'}{k_{xx}}e^{i\gamma y'}\delta(x,y')dy' = \frac{i2\omega}{\alpha_{xx}}\tilde{T} \tag{3-28}$$

where $\alpha_{xx} = k_{xx}/C$ is the thermal diffusivity in the $x-$ direction. Next, the first-order x-derivative in Eq. (3-28) can be removed by introducing

$$\tilde{T}(x,\gamma) = w(x,\gamma)e^{i\gamma\varepsilon_{xy}x}, \tag{3-29}$$

leading to

$$\frac{\partial^2 w}{\partial^2 x} - \gamma^2(\varepsilon_{yy} - \varepsilon_{xy}^2)w + e^{-i\gamma\varepsilon_{xy}x}\int_{-\infty}^{\infty}\frac{P'}{k_{xx}}e^{i\gamma y'}\delta(x,y')dy' = \frac{i2\omega}{\alpha_{xx}}w. \tag{3-30}$$

Similarly transforming the boundary conditions leads to

$$\frac{\partial w}{\partial x} = 0 \ @ \ x = 0 \tag{3-31}$$

$$\frac{\partial w}{\partial x} = 0 \text{ and } w = 0 \ @ \ x = \infty. \tag{3-32}$$

Note that for the boundary condition at $x = 0$ for this transformed temperature, the eigenfunction for the homogenous heat conduction problem is $\cos(\beta x)$.

The next step is to remove the x-derivatives using another pair of integral transforms: $\zeta(\beta, \gamma) = \int_0^\infty \cos(\beta x') w(x', \gamma) dx'$ and $w(x, \gamma) = \frac{2}{\pi} \int_0^\infty \cos(\beta x) \zeta(\beta, \gamma) d\beta$. Thus the solution in terms of transform variables is

$$\zeta(\beta, \gamma) = \frac{P'/k_{xx}}{i2\omega/\alpha_{xx} + \beta^2 + \gamma^2(\varepsilon_{yy} - \varepsilon_{xy}^2)}. \tag{3-33}$$

After performing the required inverse transforms, the integral form in terms of x and y is

$$\overline{T}(x, y) = \frac{2P'}{\pi^2 k_{xx}} \int_o^\infty \int_0^\infty \frac{\cos(\beta x)\cos(\gamma(y - \varepsilon_{xy}x))}{q_{xx}^2 + \beta^2 + \gamma^2(\varepsilon_{yy} - \varepsilon_{xy}^2)} d\beta d\gamma, \tag{3-34}$$

with $q_{xx} = \sqrt{i2\omega C/k_{xx}}$ defined in Eq. (3-9).

An important check of Eq. (3-34) is to simplify it for an isotropic sample and verify it recovers the well-known closed-form solution given by Cahill in 1990.[22] Setting $\varepsilon_{yy} = 1$ and $\varepsilon_{xy} = 0$, we see that this is indeed true,

$$\overline{T}(x, y) = \frac{2P'}{\pi^2 k} \int_o^\infty \int_0^\infty \frac{\cos(\beta x)\cos(\gamma y)}{q^2 + \beta^2 + \gamma^2} d\beta d\gamma$$

$$= \frac{P'}{\pi k} K_0\left(q\sqrt{x^2 + y^2}\right) \tag{3-35}$$

where K_0 is the modified Bessel function of the second kind, and the integrals were evaluated using symbolic math software (MAPLE).

Returning to the full solution of Eq. (3-34), it is fruitful to make the substitutions $\gamma'^2 = \gamma^2(\varepsilon_{yy} - \varepsilon_{xy}^2)$ and $y' = \frac{y - \varepsilon_{xy}x}{\sqrt{\varepsilon_{yy} - \varepsilon_{xy}^2}}$. We have:

$$\overline{T}(x, y) = \frac{2P'}{\pi^2 k_{xx}\sqrt{\varepsilon_{yy} - \varepsilon_{xy}^2}} \int_o^\infty \int_0^\infty \frac{\cos(\beta x)\cos(\gamma' y')}{q_{xx}^2 + \beta^2 + \gamma'^2} d\beta d\gamma' \tag{3-36}$$

Thus, after this transformation the *anisotropic* problem's integral of Eq. (3-36) is now formally equivalent to the *isotropic* problem's integral of Eq. (3-35). Therefore the solution to Eq. (3-36)

follows immediately, and returning to the original (untransformed) variables, we have the solution for the δ-function line heater as

$$\bar{T}(x,y) = \frac{P'}{\pi k_{xx}\sqrt{\varepsilon_{yy} - \varepsilon_{xy}^2}} K_0\left(\frac{q_{xx}\sqrt{\varepsilon_{yy}x^2 + y^2 - 2\varepsilon_{xy}xy}}{\sqrt{\varepsilon_{yy} - \varepsilon_{xy}^2}}\right) \tag{3-37}$$

which is equivalent to Eq. (3-8) in the main text.

Finite-width heater line

We now obtain solutions for the finite heater-width case, including the surface temperature field and average temperature of the heater line. Through suitable substitutions, we can again transform the anisotropic problem into an equivalent isotropic one, thereby exploiting the exact analytical solutions obtained by Duquesne et al.[104] for the isotropic case.

We begin here from Eq. (3-11) of the main text. Scale b, y, and y' such that for any variable η, its scaled counterpart is

$$\tilde{\eta} = \eta\frac{k_{xx}}{k_{det}}, \tag{3-38}$$

resulting in

$$T_{surf}(\tilde{y}) = \frac{P'}{2\tilde{b}\,\pi\sqrt{k_{xx}k_{yy} - k_{xy}^2}} \int_{-\tilde{b}}^{\tilde{b}} K_0\left(q_{xx}|\tilde{y} - \tilde{y}'|\right)d\tilde{y}'. \tag{3-39}$$

We have again succeeded in converting the relevant integral from an anisotropic to isotropic formulation. An equivalent isotropic integral was formulated in Fourier space by Cahill in 1990,[22] though it was 20 years before the analytical solution was first obtained by Duquesne et al.[104] We can adapt their isotropic solutions directly. Thus, the closed form solution for surface temperature caused by a finite -width heater line on an *anisotropic* substrate is written down directly as Eq. (3-12).

Proceeding similarly for the average temperature of the heater line on the anisotropic substrate, we write

$$\langle T \rangle = \frac{P'}{4b^2\pi\sqrt{k_{xx}k_{yy} - k_{xy}^2}} \int_0^{2b}\int_0^{2b} K_0\left(\frac{q_{xx}k_{xx}(u-v)}{\sqrt{k_{xx}k_{yy} - k_{xy}^2}}\right)dudv. \tag{3-40}$$

After scaling u, v and b using Eq. (3-38), we again obtain an integral formally identical to one solved by Duquesne et al.,[104]

$$\langle T \rangle = \frac{P'}{4\tilde{b}^2 \pi \sqrt{k_{xx} k_{yy} - k_{xy}^2}} \int_0^{2\tilde{b}} \int_0^{2\tilde{b}} K_0\left(q_{xx}(\tilde{u} - \tilde{v})\right) d\tilde{u}\, d\tilde{v} . \qquad (3\text{-}41)$$

Finally, after suitably rewriting the isotropic result,[104] the average heater line temperature for our anisotropic substrate can be expressed in terms of the Meijer-G function, resulting in Eq. (3-13) of the main text.

3.7.2 Major axes orientation of elliptical isotherms

We consider the temperature field caused by a δ-line heater on an arbitrarily anisotropic substrate, given by Eq. (3-37). The locus for isothermal lines was recognized in Eq. (3-10), which is reminiscent of the general form of an ellipse inclined at an angle ϕ from the x axis, given by

$$\frac{(x\cos(\phi) + y\sin(\phi))^2}{a^2} + \frac{(x\sin(\phi) - y\cos(\phi))^2}{b^2} = const \qquad (3\text{-}39)$$

Matching the coefficients of x^2, y^2, and xy in Eqs. (3-10) and (3-39) gives 3 equations,

$$\frac{\cos^2(\phi)}{a^2} + \frac{\sin^2(\phi)}{b^2} = \varepsilon_{yy} \qquad (3\text{-}40)$$

$$\frac{\sin^2(\phi)}{a^2} + \frac{\cos^2(\phi)}{b^2} = 1, \qquad (3\text{-}41)$$

$$2\cos(\phi)\sin(\phi)\left(\frac{1}{a^2} - \frac{1}{b^2}\right) = -2\varepsilon_{xy} \qquad (3\text{-}42)$$

which can be solved for a, b and ϕ:

$$a^2 = \frac{\cos^4(\phi) - \sin^4(\phi)}{\varepsilon_{yy}\cos^2(\phi) - \sin^2(\phi)} \qquad (3\text{-}43)$$

$$b^2 = \frac{\cos^4(\phi) - \sin^4(\phi)}{\cos^2(\phi) - \varepsilon_{yy}\sin^2(\phi)} \qquad (3\text{-}44)$$

$$\tan(2\phi) = \frac{-2\varepsilon_{xy}}{\varepsilon_{yy} - 1} = \frac{-2k_{xy}}{k_{yy} - k_{xx}} \qquad (3\text{-}45)$$

This expression for ϕ is exactly the same as the known result[116] for the angle between the principal conductivity of a material and the surface normal (the $x-$ direction in Figure 3-1). Thus, this result proves that the isotherms for a δ-line heater on a semi-infinite substrate are

ellipses whose major and minor axes are exactly aligned with the principal thermal conductivities of the material, regardless of the rotation of the free surface around the z axis.

Chapter 4 - Easily accessible, low cost approaches to measure the scattering phase function of optically thin samples

4.1 Introduction

The light scattering phase function of a material is a crucial performance metric in various applications such as transparent ceramics,[20] photography,[117] and water turbidity.[118] The optical and geometric thickness of the scattering media can range from large, such as underwater photography, to thin scatterers, such as lasing media and papers.[119] Newly developed ceramic lasing materials, which need to be screened for their optical properties, are often thin when manufactured by sintering. Usual methods for characterizing the light transmission include the use of specialized and possibly expensive optical equipment such as a laser source, integrating spheres, and high precision goniometers.[20,29] The need for such measurements in a large array of research and engineering topics necessitates a high throughput and cost effective method to do so. In view of this, image resolution-based techniques have been used to measure the scatter function of imaging media for photography applications and water quality detection[118].

Most of the resolution-based techniques use a metric called the modulation transfer function, MTF, which describes the contrast observed while imaging a target with periodic lines of dark and white/ transparent stripes. The MTF is defined as

$$MTF = \frac{I_{max} - I_{min}}{I_{max} + I_{min}},$$
(4-1)

where I_{max} and I_{min} are the maximum and minimum intensities in the image captured. An MTF of 1 indicates that the lines are perfectly resolvable, and vice versa for 0 MTF. The change in MTF, in the presence of a sample-of-interest in the imaging path, can be related to its scattering properties. Such techniques have been developed for optically thick media[118,120] and for thin scatterers[117] with highly anisotropic scattering properties.

Similar to the MTF, the edge spread function, ESF, in the presence of thin scatterers has also been used to find the optical properties of photographic papers,[119] using computationally intensive Monte Carlo approaches, and in human tissues,[121–123] using analytical methods that do not consider effects of refraction and reflection. In the ESF based methods, the scattering sample is placed in between an illuminated knife edge and a detector screen. The spread of illumination into the region of the detector screen obscured by a knife edge is a function of the scattering phase function and the fraction of the rays transmitted unscattered through the sample.

In this work, we focus on measuring the forward scattering property of thin samples using both MTF and ESF approaches. Two kinds of setups are studied here with the primary difference being the nature of the source, i.e. collimated vs a diffuse source. Both methods require the thin scatterer assumption, which implies that:

    i.   most of the light suffers at most one scattering event while traversing through the material, and

    ii.   the thickness of the sample is much smaller than the other dimensions in the model.

We develop semi-analytical solutions for the ESF and MTF within the thin scatterer approximation for both setups. Then, experiments are carried out to demonstrate the above techniques for a surface scatterer. Finally, we compare the strengths, weaknesses, and the scope of applicability for the proposed methods.

Methods

4.2 Collimated Light source

We first discuss two methods that require a collimated light source. Both methods require the following four sequentially placed optical elements, as shown in Figure 4-1:

    i.   a collimated light source,
    ii.   resolution test target: (a) Knife edge for edge spread function, or (b) USAF 1951 target for modulation transfer function,
    iii.   the scattering sample, and
    iv.   detector screen.
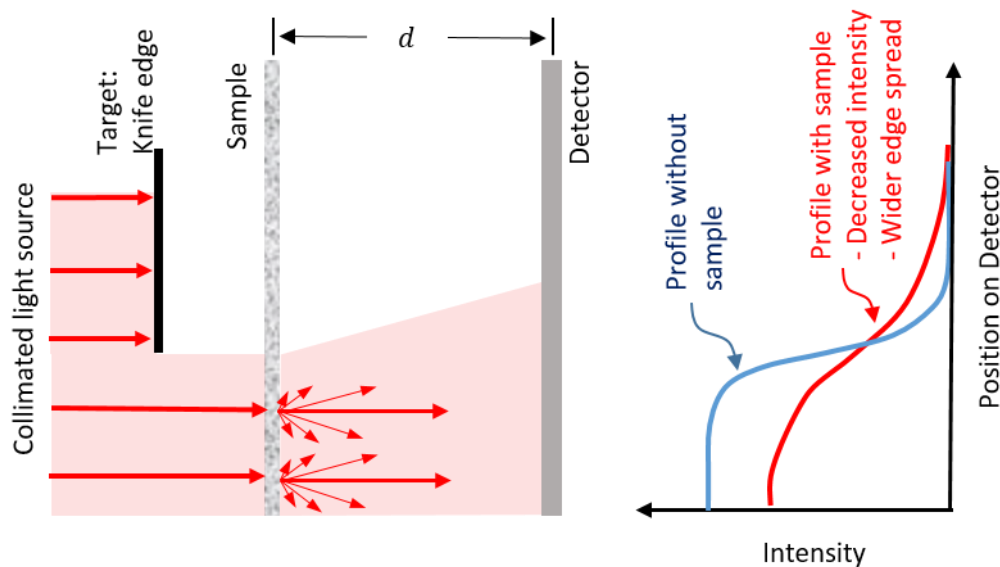
Figure 4-1 The setup for measuring scattering properties with a collimated light source. A knife edge is used as the target for the ESF approach, while a USAF 1951 target (not shown) is used for the MTF approach.

All the above optical elements need not be specialized scientific equipment and are easily procured. For example, a LED light source placed far away from the experimental setup can serve as a collimated source. A fine paper (here card stock) functions as the detector screen, which is imaged by a camera. It is helpful if the camera sensor has a linear response to the incident intensity. Otherwise, proper care should be taken to calibrate for the camera sensor's non-linear response.

In the setup, collimated light is incident on the target which selectively lets light pass through either through alternating strips (MTF-based method) or like a Heaviside step function (ESF-based method). Two different sets of measurements are taken at this point. One set of measurements omits the scattering sample in between the target and the detector screen, while the other set of measurements includes the scattering sample, located at a variable distance d from the detector screen. Since the light source is collimated, the distance between the target and the sample does not matter for the analysis. A comparison of the detected pattern with and without the presence of the scattering sample will be used to find the scattering properties of the sample in this study.

As demonstrated in the schematic of Figure 4-1, the scattering sample scatters and spreads a fraction of the incident light, while another fraction transmits through unscattered. The total forward transmitted light (forward scatter + unscattered transmission) is also reduced due to front and backside reflection at the surfaces of the sample and back-scatter within the sample. For either ESF or MTF-based approaches, the first step to finding the effect of scattering on the detected pattern is to find the point spread function, PSF, of the system. The relation between this point spread function and the scattering properties of the sample is described in the following subsection.

4.2.1 Theory

The scattering property of the sample is defined using two terms: (i) the scattering coefficient, β_{sca}, and (ii) the angle dependent scattering phase function, $\Phi(\theta_i, \theta_s)$, which is defined as follows: When a ray of light of power P is incident on a scattering medium of thickness ds at polar angle θ_i (measured from the normal of the scattering surface) the power scattered into a differential solid angle $d\Omega$ in direction θ_s is given by:

$$dP_{scatt} = P \frac{\beta_{sca} ds}{\cos(\theta_i)} \Phi(\theta_i, \theta_s) \frac{d\Omega}{4\pi} . \tag{4-2}$$

Equation 4-2 holds true when the product $\beta_{sca} ds \ll 1$. While the scattering phase function can be a function of azimuthal angles ϕ in general, for clarity this work is limited to axisymmetric samples. Removing this assumption is straightforward in principle, but can be computationally expensive. Now that the scattering properties of the sample are defined, we can proceed to finding the scattering PSF for the setup of Figure 4-1.
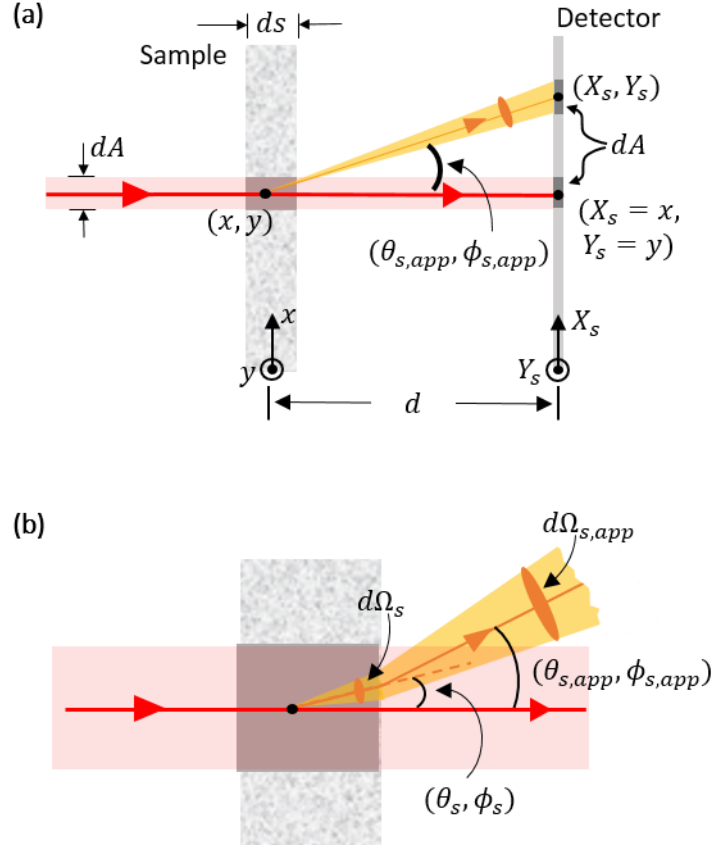
Figure 4-2: Detailed view of the scattering process. (a) Zoomed out view where effects of refraction are excluded. (b) Refraction changes the apparent scattering angle visible outside the medium, while also altering the solid angle subtended by the differential area *dA* from a point (*x,y*) on the sample.

Figure 4-2(a) shows a more detailed view of the scattering phenomena without including the effects of refraction. It will be easier to include the effects of refraction when we are further along in the derivation. Consider the incident collimated light carrying a power per unit area P'' [W/m^2] incident on an area dA on the sample at co-ordinate (*x,y*). After reflection at the front surface, a fraction of the power,

$$(1 - R_1(0°))P''dA, \tag{4-3}$$

continues into the sample. $R_1(\theta)$ is the reflection loss for incidence angle θ (here, $\theta=0°$) that can be calculated from the well-known Fresnel relations. As the light propagates through the sample, a fraction of the light transmits through unscattered and unabsorbed, and is incident on the detector at a point ($X_s=x, Y_s=y$) after suffering another reflection loss ($R_2(0°)$) at the sample's backside. The power thus incident at point (*x,y*) on an area dA in the detector is given by

$$dP_0(X_s = x, Y_s = y) = (1 - R_1(0))(1 - R_2(0))(\exp(-(\beta_{sca} + \alpha)ds))P''dA, \tag{4-4}$$

where β_{sca} and α are the scattering and absorption coefficients of the sample, and *ds* is its thickness. The subscript 0 indicates this is due to unscattered rays.

Next, we consider the effects of scattering of light within the sample, which redistributes a fraction of the incident power. By invoking Eq. (4-2), we find that the power scattered to the point (X_s, Y_s) on an area dA is

$$dP_s(X_s, Y_s) = (1 - R_1(0))(1 - R_2(\theta_{s,app})) \frac{\beta_{sca}}{\beta_{sca} + \alpha} (1 - \exp(-(\beta_{sca} + \alpha)ds)) \times$$
$$\frac{\Phi(0, \theta_{s,app})}{4\pi} \frac{dA \cos^3 \theta_{s,app}}{d^2} P'' dA,$$

(4-5)

where the term $dA \cos^3\theta/d^2$ is the solid angle, $d\Omega_{s,app}$ subtended by the area dA at point (X_s, Y_s) to the point (x,y). Also $R_2(\theta_{s,app})$ is the loss due to reflection calculated again using Fresnel relations, and

$$\theta_{s,app} = \tan^{-1}\left(\frac{\sqrt{(X_s - x)^2 + (Y_s - y)^2}}{d}\right).$$

(4-6)

We have used the subscript, *app*, implying apparent for the angle $\theta_{s,app}$, since $\theta_{s,app}$ represents the apparent scatter angle without taking refraction effects into account (see Figure 4-2(b)). In actuality, the ray has to be scattered at an angle,

$$\theta_s = \sin^{-1}\left(\frac{\sin \theta_{s,app}}{\eta}\right),$$

(4-7)

within the sample, so that after refraction, the rays land at the point (X_s, Y_s). η is the refractive index of the sample. In addition, due to refraction, the solid angle subtended by the area dA, in the region within the sample $d\Omega_s$, can be calculated with respect to the solid angle outside the sample, $d\Omega_{s,app}$, by conserving etendue at the backside surface,[29]

$$d\Omega_s = d\Omega_{s,app} \frac{\cos \theta_{s,app}}{\eta^2 \cos \theta_s}.$$

(4-8)

After including the effects of refraction, Eq. (4-5) becomes

$$dP_s = (1 - R_1(0°))(1 - R_2(\theta_s)) \frac{\beta_{sca}}{\beta_{sca} + \alpha} (1 - \exp(-(\beta_{sca} + \alpha)ds))$$
$$\frac{\Phi(0, \theta_s)}{4\pi} \frac{dA \cos^3 \theta_{s,app}}{d^2} \frac{\cos \theta_{s,app}}{\eta^2 \cos \theta_s} P'' dA,$$

(4-9)

where the angles θ_s have replaced $\theta_{s,app}$ in two of the terms and the subtended solid angle has been modified.

At this stage we can define the point spread function: $PSF(x,y{:}X_s,Y_s)$ iss the detected intensity at position (X_s,Y_s) on the detector screen in response to a δ-function point source incident at a point (x,y) on the sample. This is found by dividing the incident powers in Eqs. (4-4) and (4-9) by $P''(dA)^2$, yielding

$$PSF(x, y : X_s, Y_s) = (\exp(-(\beta_{sca} + \alpha)ds))(1 - R_1(0))(1 - R_2(0))\delta(X - x)\delta(Y - y)$$

$$+ \frac{\beta_{sca}}{\beta_{sca} + \alpha}(1 - \exp(-(\beta_{sca} + \alpha)ds))(1 - R_1(0))(1 - R_2(\theta_s))\frac{\Phi(\theta_s)\cos^3\theta_{s,app}}{4\pi d^2}\frac{\cos\theta_{s,app}}{\eta^2\cos\theta_s},$$

$$(4\text{-}10)$$

where the first and second terms represent the contributions due to unscattered and scattered light respectively. Since the analysis of Figure 4-2 is translationally invariant in the x and y directions, the $PSF(x,y{:}X_s,Y_s)$ is a function of only the relative displacement between the incident point and the detector point, $(\Delta X = |x - X_s|)$ and $(\Delta Y = |y - Y_s|)$. We will henceforth use the notation, $PSF(\Delta X, \Delta Y)$.

4.2.1.1 *Modulation Transfer Function and Edge Spread Function*

Finally to get to the MTF or the ESF, first the line spread function, LSF, is calculated by integrating the point spread function over a line source,

$$LSF(\Delta X) = \int_{-\infty}^{\infty} PSF(\Delta X, \Delta Y')d(\Delta Y'), \qquad (4\text{-}11)$$

Then the MTF is the spatial Fourier transform of the normalized LSF,

$$MTF(f) = F\{LSF(\Delta X_s)\}. \qquad (4\text{-}12)$$

The modulation transfer function is always 1 at zero spatial frequency, f, and goes down with increasing spatial frequency depending on the imaging system. The measured modulation transfer function in an experiment includes contribution due to scattering by the sample, defined as MTF_{scatt}, as well as imperfections in the imaging system, MTF_{setup}. In the Fourier domain, the total MTF for a linear system can be calculated simply as[120]

$$MTF_{tot} = MTF_{scatt} \times MTF_{setup}. \qquad (4\text{-}13)$$

In Section 4.2.2.2 MTF_{tot} and MTF_{setup} are measured by post-processing the images captured in the presence and absence of the scattering sample. At that point, we can find the best fit solutions for β_{sca} and Φ that yields the MTF_{scatt} satisfying Eq. (4-11).

Similarly, the EFS measured in the presence of the scattering sample includes contributions from spreading due to imaging setup imperfections as well as the scattering sample itself. The final

edge spread function with a scatterer, ESF_{tot}, is the convolution of that without scatterer, ESF_{setup}, and the scattering LSF,

$$ESF_{tot}(X_s) = \int_{-\infty}^{\infty} ESF_{setup}(X_s') LSF_{scatt}(X_s - X_s') dX_s', \qquad (4\text{-}14)$$

As before, we can fit for values of β_{sca} and Φ, that gives the total ESF upon carrying out the convolution of Eq. (4-14).

4.2.2 Validation Experiments with a Surface Scatterer: Engineered Diffuser

4.2.2.1 *Edge Spread Function Method*

In this section, we demonstrate the above two methods with experiments on an engineered diffuser (Thorlabs part no: ED1-C20). The engineered diffuser is designed to have no significant unscattered transmission which eliminates the first part of Eq. (4-10). The diffuser is specified to uniformly redistribute a fraction of the incident light over a nominally 10°-half-angle cone in the forward direction. Thus the diffuser functions as an infinitesimally thin scattering sheet, and we do not have to consider the effects of refraction in Eq. (4-10). Since the scattering surface of the engineered diffuser is an array of micro-lenses, the Fresnel laws of reflection for a flat slab are not directly applicable. Here, we absorb the effect of reflection into the scattering phase function, and define the PSF as

$$PSF(x, y : X_s, Y_s) = \frac{\Phi(0, \theta_s) \cos^3 \theta_s}{4\pi d^2}, \qquad (4\text{-}15)$$

where we assume the following top hat function for the scattering phase function,

$$\Phi(0, \theta_s) = \left\{ \begin{array}{cc} 1/\Delta\theta_{diff} & \theta_s \le \Delta\theta_{diff} \\ 0 & \theta_s > \Delta\theta_{diff} \end{array} \right\}. \qquad (4\text{-}16)$$

$\Delta\theta_{diff}$ is the cone angle in radians. The aim in this experiment is to characterize the cone angle $\Delta\theta_{diff}$ of the diffuser.

A mounted LED (Thorlabs MWWHL3) with an aspheric lens (Thorlabs ACL5040U-A) and a red filter was used as the collimated light source, while a thin metal sheet functions as a knife edge. While the LED light source itself could have functioned as a collimated source when placed far away from the setup, the collimation adapter can be placed right behind the target, thus resulting in a compact setup. We used a high density paper (card stock) to function as the detector screen, and finally a camera placed behind the detector takes an image of the detector. We used cage setups to hold the detector screen and the scattering diffuser aligned with each other throughout the experiment. If the forward scattering property of the detector screen paper is independent of the incident light angle, then the spatial intensity profile detected by the camera is directly proportional to the total light power incident at the corresponding position on the

detector screen. We verified this by shining a light from a pen laser at various incidence angles to the detector screen. The intensity profile detected by the camera behind the screen was constant for a wide range of incidence angles. This eliminated the need for further calibration.

After calibrating the pixel position in the camera to the physical position on the detector screen itself, an average intensity profile is extracted by taking an average of multiple profiles over a rectangular section of the image (see inset corresponding to d=4mm in Figure 4-3(a)). As described in Section 4.2.1.1, we first measured the edge spread function without any scatterer in between the knife edge and detector screen. This is the baseline measurement, ESF_{setup}, and the corresponding normalized intensity profile is shown by the blue dots in Figure 4-3(a). The normalized intensity is given by

$$I^*(X_s) = \frac{I(X_s) - I_{dark}}{I_{bright} - I_{dark}}, \tag{4-17}$$

where I_{bright} and I_{dark} are the bright and dark intensity values recorded far away from the knife edge. Following this, we carried out successive measurements with the diffuser at multiple distances, d =4mm to 20mm, from the detector screen (red dots in Figure 4-3(a)). As is intuitive, with increasing distance between the diffuser and the detector, the image becomes blurrier and thus the spread in the intensity profiles increases.
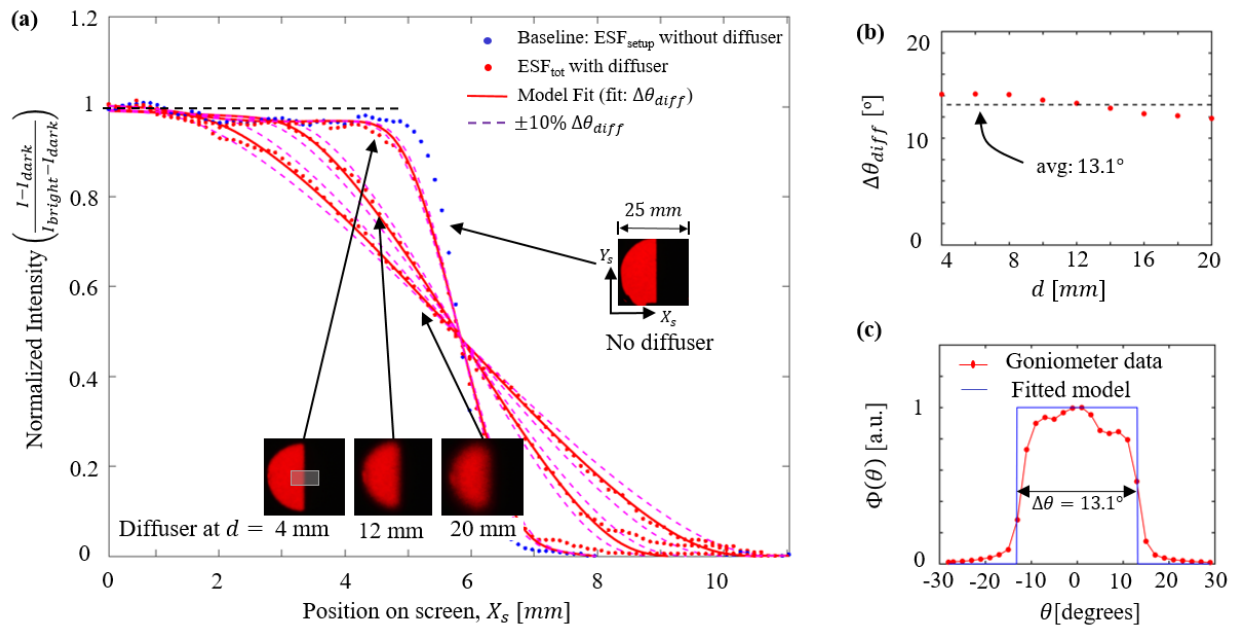
Figure 4-3 (a) Normalized intensity values detected at the image screen without a diffuser and with diffuser at d = **4mm , 12mm, and 20mm from the screen. The model fits the data very well. The 10% uncertainty bounds are found by perturbing the extracted** $\Delta\theta_{diff}$ **by ± 10% for each intensity profile. (b) The fitted value for** $\Delta\theta$ **is repeatable over multiple d values. (c) The top hat profile fit by our model well describes the more featured scatter phase function measured by a goniometer setup, which requires additional equipment such as function generator, laser diode, laser controller, photodetector, and a lock-in amplifier.**

For the ESF method, the normalized intensity profile corresponding to each d value is a different experiment, and $\Delta\theta_{diff}$ was calculated for each of the profiles. The fitted ESF_{total} (solid red lines

in Figure 4-3(a)) match up with the experimental points. We also show in Figure 4-3(b) that the fitted $\Delta\theta_{diff}$ values are repeatable within ±6% (std. dev.) for the range of d values studied.

To confirm the validity of the ESF experiments, we compared the results with that from a more traditional experiment, where a modulated laser light is incident on the sample fixed at the center of a rotation stage. A photodetector is placed on a cantilever beam such that it revolves around the sample when the stage is rotated. A lock-in amplifier synced to the laser modulator is used to measure the angle dependent scatter phase function. The normalized scattering phase function of the diffuser is plotted in Figure 4-3(c). We see that $\Phi(\theta)$ extracted from the rotation stage setup resembles a top-hat function, and agrees well with the normalized profile obtained using Eq. (4-15) with a $\Delta\theta_{diff}$ averaged over all the values shown in Figure 4-3(b).

From the width of the ±10% uncertainty bounds shown in Figure 4-3(a), we can infer that the sensitivity of $I^*(X_s)$ to $\Delta\theta_{diff}$ is much higher at larger distances, d. This can be explained by the larger spatial spread of the point spread function with increasing d. On the other hand, the normalization process of Eq. (4-17) requires the saturated bright and dark intensity information collected far away from the nominal knife edge shadow line, which may not be possible for large d values because of the finite sample size. The measured scatter phase function is most precise when the d values are chosen such that the complete edge spread function is captured while maximizing the spatial spread of the PSF. In addition, it is necessary to ensure the alignment of the center line for each of the captured edge spread functions with and without the scattering sample, so that the convolution of Eq. (4-14) is valid. The involved data analysis and the stringent alignment requirements can be relaxed by using the modulation transfer function method we discuss in the next subsection.

4.2.2.2 *Modulation Transfer Function Method*
In this method, we replace the knife edge of the previous experiment with a USAF 1951 target, a standard for specifying the resolution of imaging systems. In this experiment, we restrict the measurements to group -2, which has lines with spatial frequencies ranging from 0.25 lines/mm to 0.445 lines/mm. The typical image obtained looks like the inset images in Figure 4-4(a). The MTF is calculated by simply applying Eq. (4-1) on line cuts taken across the imaged line pairs (Figure 4-4(b)).
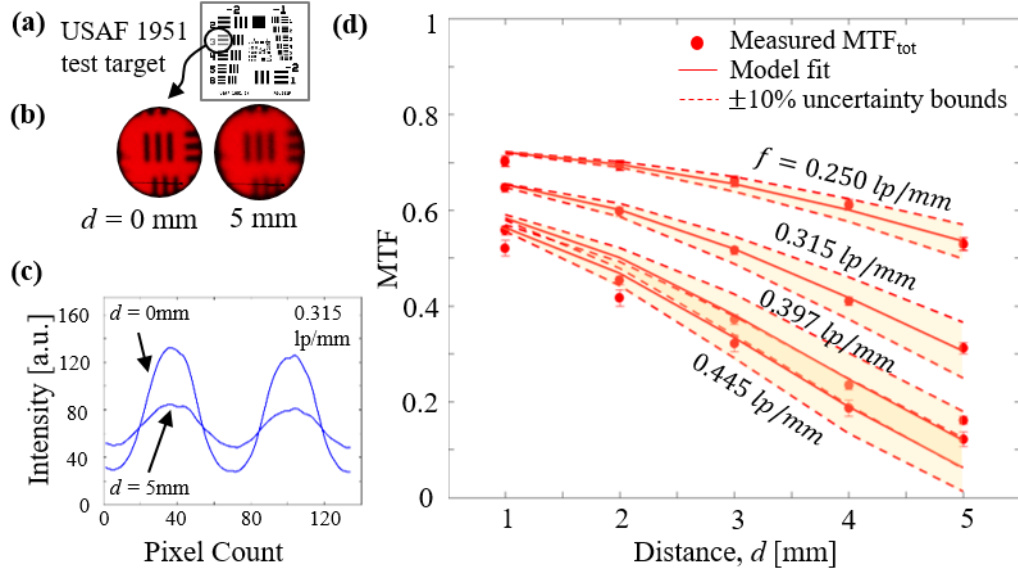
Figure 4-4 (a) For the MTF experiments using collimated light, the knife edge of Figure 4-1 is replaced by a USAF 1951 test target. (b) Captured images for a pattern with spatial frequency 0.315 line pairs per mm (lp/mm) corresponding to Gr-3 El 3 of the target. The images become blurrier as the distance d increases. (c) Average cutline measured across the imaged line pairs corresponding to images from (b). The dark level increases while the bright level decreases with increasing d. (c) Measured and modeled MTF values for line pairs with spatial frequencies 0.250, 0.315, 0.397 and 0.445 lp/mm respectively. The 10% uncertainty bounds are found by perturbing the extracted $\Delta\theta_{diff}$ by ±10%.

For the modulation transfer experiments, the baseline MTF$_{setup}$ is found by processing the image with the scattering diffuser at $d = 0$ mm, i.e. in contact with the detector screen. Following this, successive MTF measurements are carried out for increasing d, as shown in Figure 4-4(c). In this case each series of MTF(d) measurements for a given spatial frequency is considered a separate experiment to extract the scattering phase function. This is in contrast with the ESF method where a single shot edge spread function at a single d is sufficient to extract the scattering properties.

Table 4-1: Fitted values of $\Delta\theta$ for the four spatial frequencies studied in Figure 4-4 above.

Spatial frequency, f [lp/mm]	Fitted $\Delta\theta_{diff}$[°]
0.315	11.0
0.353	13.5
0.397	14.1
0.445	13.6

The fitted lines with ±10% uncertainty bounds shown in Figure 4-4(c) agree well with the measured MTF values, and the corresponding extracted $\Delta\theta_{diff}$ values are listed in Table 4-1. $\Delta\theta_{diff}$ is also close to the average value measured by the ESF method of 13.1°, thus demonstrating the applicability of the MTF method as well. From the width of the 10% bounds, we see that the measurement is again more sensitive to the scatter phase function as d increases. The MTF method, while slightly more expensive than the ESF method due to the need for a USAF test

target, has significant advantages of easier data analysis, and no requirements for alignment between successive measurements.

4.3 Diffuse Light source

Sometimes a large diffuse light source such as a light table is more readily available than a collimated light source. We take advantage of this in the current method, where a diffuse source is placed in physical contact with a USAF 1951 test target as shown in the schematic of Figure 4-5(a). The diffuse source also necessitates the use of focusing to get enough intensity on a screen located far away from the light source. The sample-of-interest is placed between a USAF target back-illuminated by the diffuse light source, and a camera focused on the USAF target. Since the light source is placed in contact with the USAF target, they can be considered one and the same. The distance between the source and sample, d, is much smaller than the distance between the camera and sample, L. Similar to the previous section, the measured MTF in the presence of the scattering sample can be used to extract its scattering properties, and we formalize this relation in the following sub-sections.
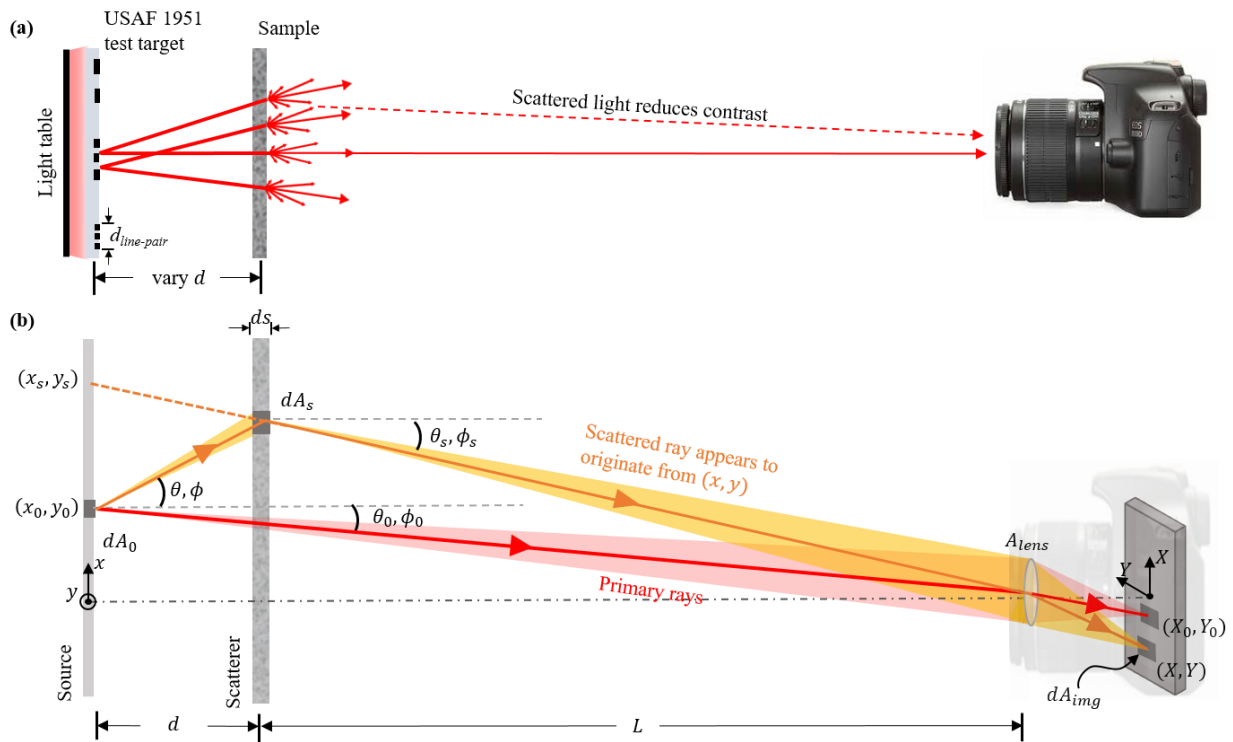
Figure 4-5 MTF method using a diffuse light source. (a) The measurement setup, and (b) Ray schematic. Objective is represented by a single lens in (b). The scattered rays represented by yellow/orange rays appear to come from the point (x_s,y_s) on the source plane as viewed from the lens. (Camera image source: Canon)

4.3.1 Theory

To estimate the MTF due to scattering by the sample, we first have to calculate the point spread function, PSF, for the imaging setup of Figure 4-5. We start by considering the smearing of image in the presence of the scattering sample in response to light emission from an arbitrary point (x_0,y_0) and area, dA_0 on the screen. It is assumed that the light source has a generalized non-

lambertian emission profile, such that the light power emitted into a solid angle, $d\Omega$, in a direction at a polar angle, θ is

$$I_0 \cos^n \theta dA_0 d\Omega,\qquad\qquad(4\text{-}18)$$

where I_0 is a constant carrying the units of intensity [W/(m^{2}sr)] and the exponent n quantifies the spread in the source emission profile. A separate measurement is required to determine n if the value is not provided by the manufacturer.

When the camera objective's aperture is small compared to the distance between the source/scatterer and the camera, i.e. both L and L+d are larger than the aperture size, a small angle approximation can be invoked. Under this assumption, un-scattered light from the source reaching the camera travels effectively in the same direction within an extremely narrow cone (subtended solid angle $\sim A_{lens}\cos^3(\theta_0)/(L+d)^2$). This has been schematically shown by the red cone in Figure 4-5. Using the easily measured magnification, M, of the imaging system, it is known that the unscattered power will be incident on an area, $dA_{img}=M^2 dA_0$ on the image screen, centered around the point,

$$\left(X_0,Y_0\right)= M \times \left(x_0, y_0\right).\qquad\qquad(4\text{-}19)$$

The unscattered power that transmits through the sample and is incident on point (X_0, Y_0) is

$$dP\left(X_0,Y_0\right)= I_0 \cos^n \theta_0 \exp\left(-\frac{(\beta_{sca}+\alpha)ds}{\cos(\theta_0)}\right)dA_0 \frac{A_{lens}\cos^3 \theta_0}{\left(L+d\right)^2}.\qquad(4\text{-}20)$$

In the presence of a scattering sample, a fraction of the light power emitted in a different direction (θ, ϕ), is scattered within the area, dA_s, towards the aperture, as shown by yellow rays in Figure 4-5(b). To the camera, this scattered ray appears to come from the position (x_s, y_s) in the object plane. Again, invoking the small angle approximation, this scattered power is incident around the point (X,Y)=$M(x_s, y_s)$, with magnitude,

$$dP_{scatt}\left(X,Y\right)= I_0 dA_0 \frac{\beta_{sca}}{\beta_{sca}+\alpha}\left(1-\exp\left(-(\beta_{sca}+\alpha)\frac{ds}{\cos\theta}\right)\right)\cos^n \theta$$

$$\frac{dA_s \cos^3 \theta}{d^2}\frac{\Phi(\theta,\theta_s)}{4\pi}\frac{A_{lens}\cos^3 \theta_s}{L^2}.\qquad\qquad(4\text{-}21)$$

To compare the powers of the unscattered and the scattered rays, the respective incident areas on the image screen have to be consistent. To produce an image on an area, $dA_{img}=M^2 dA_0$ in the image plane, the scattered rays must be scattered by area, $dA_s = dA_0/(1+d/L)$ on the sample of interest. The factor of ($1+d/L$) arises because the sample is closer to the camera compared to the screen.

Traditionally, the point spread function is the response on the image X-Y plane to an impulse on the object x-y plane. In this method, we want to calculate the MTF on the image plane, which

implies that the line spread function (Eq. 4-11) on the image plane should be normalized so that the integration of LSF over the image plane is 1. This ensures that the MTF is 1 at spatial frequency f=0. Thus, the PSF we will show next needs to be normalized while carrying out the numerical evaluations from Eqs. 4-12 to 4-13. For this purpsose, it is essential to make sure the ratio of the unscattered and scattered contributions is correct, while the exact magnitude is not required to be known.

With the above discussion in mind, we calculate a PSF by including the scattered and unscattered contributions divided by dA_{img}^2 or $M^2 dA_0^2$, so that the arbitrarily chosen differential areas dA_0 or dA_s in the above equations fall out. The resulting PSF is

$$PSF_{scatt}(x_0, y_0 : X,Y) = \exp\left(-\frac{(\beta_{sca} + \alpha)ds}{\cos(\theta_0)}\right)\frac{\cos^{n+3}\theta_0}{M^2(L+d)^2}\delta(X-X_0)\delta(Y-Y_0)$$
$$+\frac{\beta_{sca}}{\beta_{sca}+\alpha}\left(1-\exp\left(-(\beta_{sca}+\alpha)\frac{ds}{\cos\theta}\right)\right)\frac{\cos^{n+3}\theta}{M^4d^2(1+d/L)}\frac{\cos^3\theta_s}{L^2}\frac{\Phi(\theta,\theta_s)}{4\pi},$$

(4-22)

where, θ_0, θ and θ_s are related to (X_0, Y_0) and (X, Y) by the relations:

$$\theta_0 = \tan^{-1}\left(\frac{\sqrt{X_0^2+Y_0^2}}{M(L+d)}\right),$$
$$\theta = \tan^{-1}\left(\frac{\sqrt{(X/(1+d/L)-X_0)^2+(Y/(1+d/L)-Y_0)^2}}{Md}\right) and$$
$$\theta_s = \tan^{-1}\left(\frac{\sqrt{(X/(1+d/L))^2+(Y/(1+d/L))^2}}{ML}\right)$$

(4-23)

The data analysis is simpler when the PSF is spatially invariant in the x-y directions, and hence, it is sufficient to calculate a single PSF for a source located at the optical axis, (x_0,y_0)=(0,0). We can show that the PSF is spatially invariant when

$$L \gg d \text{ and } L \gg d_{line-pair},$$

(4-24)

holds true. In this limit, from Eqs. 4-23, we know that the angle θ is only a function of relative displacement on the image screen, i.e. $X-X_0$ or $Y-Y_0$, and not the absolute position itself. In addition, when Eq. (4-24) is valid, θ_0 and θ_s both tend to 0. In this limit, with the above approximations, a spatially invariant PSF can be found,

$$PSF_{scatt}(x_0, y_0 : X,Y) = \exp(-(\beta_{sca}+\alpha)ds)\frac{1}{M^2(L+d)^2}\delta(X-X_0)\delta(Y-Y_0)$$
$$+\frac{\beta_{sca}}{\beta_{sca}+\alpha}\left(1-\exp\left(-(\beta_{sca}+\alpha)\frac{ds}{\cos\theta}\right)\right)\frac{\cos^{n+3}\theta}{M^4d^2(1+d/L)}\frac{1}{L^2}\frac{\Phi(\theta,\theta_s=0)}{4\pi}.$$

(4-25)

4.3.1.1 *Effect of Reflection and Refraction*
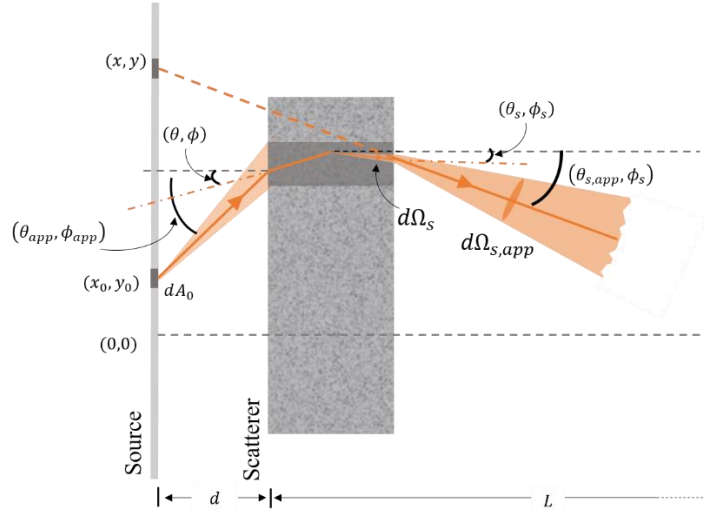
Figure 4-6 Magnified detail of Figure 4-5to exaggerate the effects of refraction. The angle through which light is actually scattered inside the sample, $\theta \rightarrow \theta_s$, is different from the angles through which it appears to scatter, $\theta_{app} \rightarrow \theta_{s,app}$. In addition, the subtended solid angle changes as light travels from one medium to another.

When the refractive index η of the sample is dissimilar from the environment, the effects of forward and backward surface reflection, as well as refraction needs to be taken into account.[29] Two angles, θ_{app} and $\theta_{s,app}$, are introduced which correspond exactly to θ and θ_s in Eq. 4-23. Due to refraction, the corresponding angles within the sample, θ and θ_s, are shallower as shown in Figure 4-6, and can be calculated using Snell's law of refraction. In addition, due to refraction, the solid angle subtended by the lens to the scattered area, in the region within the sample $d\Omega_s$, can be calculated with respect to the solid angle outside the sample, $d\Omega_{s,app}$, by conserving etendue at the backside interface,

$$d\Omega_s = d\Omega_{s,app} \frac{\cos\theta_{s,app}}{\eta^2 \cos\theta_s} . \tag{4-26}$$

This factor is exact under the assumption that $\theta_s\sim 0$, which is valid when $d/L\sim 0$. The final form of the spatially invariant PSF is

$$
\begin{aligned}
PSF_{scatt}\left(X'= X_s - Mx_0, Y'= Y_s - My_0\right) &= \left(1 - R_1(0)\right)\left(1 - R_2(0)\right)\frac{\exp\left(-(\beta_{sca} + \alpha)ds\right)}{M^2(L+d)^2}\delta(X)\delta(Y) \\
&+ \left(1 - R_1(\theta_{app})\right)\left(1 - R_2(0)\right)\frac{\beta_{sca}}{\beta_{sca} + \alpha}\left(1 - \exp\left(-(\beta_{sca} + \alpha)\frac{ds}{\cos\theta}\right)\right)\frac{\cos^{n+3}\theta_{app}}{\eta^2 M^4 d^2 L^2 (1 + d/L)}\frac{\Phi(\theta,0)}{4\pi},
\end{aligned}
\tag{4-27}
$$

where R_1 and R_2 are the front and back Fresnel reflection coefficients with the corresponding incoming angles of incidence in parentheses.

The usual experiment for this method will result in a $MTF_{tot}(d)$ or a $MTF_{tot}(f)$ curve. To infer the scattering phase function, following Section 4.2.1.1, the MTF_{scatt} calculated for a given geometry setup and scattering properties using the PSF of Eq. (4-27) can be compared with experimental

results. As we noted in the previous section, the MTF is obtained as a Fourier transform of the normalized line spread function,

$$LSF_{norm}(X) = \frac{LSF(X)}{\int\limits_{-\infty}^{\infty} LSF(X)}.$$ (4-28)

We did not demonstrate this method with experiments on the diffuser since the diffuser is designed for normal incidence of light. However, since the derivation for the point spread function Eq. 4-27 involved several approximations, we verify its validity in the next sub-section with numerical ray tracing simulations.

4.3.1.2 *Numerical verification with Ray Tracing Simulation*

We used Zemax OpticStudio, a commercial ray tracing software to validate the spatially invariant PSF in Eq. (4-26). A non-sequential model is created to simulate this work's proposed physical setup, where an extremely small circular lambertian (n=1) source acts like a point source for photons emitted from the object plane (x=0,y=0). At a distance d=20mm away from the sample, a 1 mm thick rectangular volume of refractive index η=1.5 encloses a thin scattering sheet at its center. Since the scattering is limited to a sheet, the angle dependent scatter fraction of Eq. (4-27), $\left(1 - \exp\left(-\frac{\beta_{sca}ds}{\cos\theta}\right)\right)$ is replaced by a constant, which is the specified scatter fraction in the simulated setup, here 0.2.

At a distance L+d=1m away from the light source, a thin bi-convex lens is created with refractive index $\eta = 3.5$, radius 200 mm, and a small 2.5 mm aperture, such that the focal length is 40 mm. A detector is placed at the focused location, as determined by the lens equation. The detector has square pixels with size 5μm which is large enough to capture the aberrations in the ray tracing setup. The high refractive index and the small aperture of the lens helps limit lens aberration so that a perfect lens can be simulated. Figure 4-7 shows the simulated PSF for the above setup in the presence of a sample with Gaussian scattering,

$$\Phi(\theta,\theta_s) = \frac{4}{\sigma^2\left(1 - \exp\left(-\frac{1}{\sigma^2}\right)\right)}\exp\left(-\frac{2\sin\left(\frac{|\theta - \theta_s|}{2}\right)}{\sigma^2}\right)$$ (4-27)

for two different values for the coefficient, σ, 0.1 and 1. The simulated PSF is in excellent agreement with the analytical PSF.
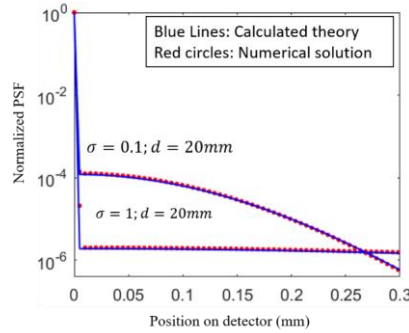
Figure 4-7 Ray tracing validation with Zemax OpticStudio for Eq. (4-27). The figure compares analytical (solid line), and ray tracing results (red dots) for the PSF obtained at the image screen for a sample with refractive index, η=1.5, scatter fraction of 0.2, and a Gaussian scattering phase function with σ= 0.1 and 1.

4.4 Summary

We analyzed two types of light sources, collimated and diffuse, to measure the light scattering properties of thin scatterers using two image resolution techniques, ESF and MTF. For each method, first the PSF was formulated as a function of the setup geometry and the scattering properties of the sample. We carried out experiments with a surface scatterer to demonstrate the methods involving collimated light sources. The results showed good agreement with measurements using the traditional but more complicated goniometer setup involving a laser source. The experimental setup for the case of ESF measurements has more stringent alignment requirements when compared to the MTF approach. In addition, the image processing and subsequent data analysis for the MTF approach is simpler. We also numerically verified the point spread for the geometry setup with a diffuse light source described in Figure 4-5(b), using a commercial ray tracing software, Zemax OpticStudio. In Table 4-2, we list the relative strengths and weakness of each of the discussed methods. Low cost and simple methods such as the ones described above can make light scattering measurements more accessible, thus making it easier to evaluate the optical quality of samples in high throughput.

Method	Theory	Experiments		
		Cost	Setup complexity	Data Analysis
Collimated source				
ESF	Straightforward Eq. 4-14	Cost effective (No USAF target). Requires collimated source (can be LED)	Stringent alignment requirements	Convolution of actual experimental data is required.
MTF	Straightforward Eq. 4-13	Needs USAF target and collimated source	Less stringent alignment requirements	Easy: Each measurement is independent, and simple algebraic division
Diffuse source				
MTF	Light focusing makes it tougher Eq. 4-27	Easier and cost effective to buy diffuse source	Less stringent alignment requirements	Easy: Each measurement is independent, and simple algebraic division.

Table 4-2 Qualities of the methods - Accessibility and expense.

Chapter 5 - Dissertation Summary and Conclusions

In this thesis, I studied several aspects that go into designing and evaluating the performance of active ions doped polycrystalline ceramics as a candidate for high power lasing media. First, in Chapter 2, the various considerations that go into designing the microstructure (grain size and shapes) so that an ideal combination of high thermal conductivity and light transmission can be achieved was discussed. Following this, methods were developed to measure the above two properties for synthesized ceramics. For thermal conductivity, in Chapter 3, a modified version of the well-known 3 omega method was develop to measure the anisotropic thermal conductivity tensor of arbitrarily oriented substrates. Finally, in Chapter 4, easily accessible and cost-effective high throughput methods were developed using image resolution techniques to measure the properties describing light transmission through thin light scattering samples.

In this Chapter, I will reiterate selected highlights for each of the above three topics, and also discuss related implications and future work.

5.1 Chapter 2 - Optimizing Thermal Transport and Light Transmission in Anisotropically Micro-Structured Materials for High Power Laser Applications

In Chapter 2, I used various modeling techniques to design the microstructure of active ion doped polycrystalline ceramics for high power lasing applications. A figure of merit (Sub-section 2.4),

$$FOM_{i,j} = \frac{k_i}{g_{th,j}} = \frac{k_i}{-\frac{1}{2l}\ln(R_1 R_2) + \beta_{sca,j}}, \qquad (5\text{-}1)$$

was introduced. For a given output mirror coupling/reflectivity, R_2 (typically $R_2 \sim 0.9$, $R_1 \sim 1$), to maximize the figure of merit, $FOM_{i,j}$, it is essential to maximize the thermal conductivity in the cooling direction, k_i, while also maintaining a very small extinction coefficient due to scattering in the lasing direction, $\beta_{sca,\,j}$. This is challenging due to the opposite ways in which the grain boundaries, ever-present in the sintered polycrystalline ceramics, affect the desirably high thermal conductivity and the desirably low light scattering coefficient in the high thermal conductivity birefringent materials, AlN and Al_2O_3, under study here. This challenge was tackled in this work by proposing an anisotropic microstructure. I discuss the key highlights for this work under three broad categories: 1) Thermal conductivity, 2) Light scattering, and 3) Figure of Merit.

5.1.1 Thermal Conductivity

I looked at the effect of grain shapes and sizes, and active ions on the thermal conductivity of polycrystalline ceramics. Following are the key conclusions in this work:

1. *Grain boundary scattering*: To calculate the effect of grain boundaries, first a simplified microstructure with columnar rod-like grains are assumed with an anisotropy ratio, *r*, is introduced. This simplification is possible because the grain sizes we study here are much bigger than the typical thermal phonon wavelengths (~<5nm). For this simplified structure, boundary scattering mean free path models were proposed in Table 2-1, which matched within 25% of highly computationally expensive Monte Carlo ray tracing simulations.

2. *Scattering due to active ions*: Active ions, such as transition metals and rare earth elements, is where the lasing action occurs and are hence unavoidable. Unfortunately, these dopants are typically heavy compared to the host lattice elements, and can hence be very strong Rayleigh-like scattering centers. While most of the thermal conductivity calculations were carried out assuming the transition element, Ti, as the active dopant, we also showed in sub-section 2.6.2.1, that heavier elements such as Tb can significantly reduce the thermal conductivity (the calculated thermal conductivity of single crystal 1%Tb:AlN is ~80% lower than that of single crystal 1%Ti:AlN).

3. *Thermal conductivity of doped polycrystalline materials, AlN and Al_2O_3*: Finally, the thermal conductivity is calculated in section 2.2.3 as a function of grain shapes and sizes. Following are the key conclusions:

   a. In the grain boundary scattering dominated regime, the anisotropic microstructure results in an anisotropic thermal conductivity in the polycrystalline material. This anisotropy in thermal conductivity is more pronounced when the grain boundary scattering is stronger. Since the grain boundaries perpendicular to the direction of phonon transport are more effective in scattering phonons, the thermal conductivity is higher in the direction of the longer grains, i.e. in the c-direction for the case of columnar rod-like grains (aspect ratio, *r*>1) and in the ab-direction for disk-like grains (*r*<1).

   b. It is essential to consider the mean free path distribution of the host materials during the material selection process. Since Al_2O_3 has smaller intrinsic mean free paths than AlN, the impact of sub-micron grain sizes on Al_2O_3 is less pronounced.

   c. When the active ions are heavy, e.g. Tb instead of Ti, the effect of grain boundaries are less pronounced since the ions become the dominant scatterers of phonons.

4. *Future work:*

   a. Often the polycrystalline ceramics synthesized by the non-equilibrium methods also have pores and second phase inclusions, such as aluminum oxynitride (AlON) in the case of AlN. Future efforts can be directed towards understanding the effects of the above defects on the thermal conductivity. The effect of dispersed pores can be calculated by carrying out ray tracing simulations on realistic porous structures. Modeling techniques such as molecular dynamics[124] can be used to calculate the phonon transmission probability at the interface between dissimilar phases.

b. To model the effect of rare earth elements, I used Rayleigh-like[56,57] scattering models that take the mass difference into account. Mass defect parameter, A_{MD} calculations in sub-section 2.6.2.1 with Tb as the dopant show that the thermal conductivity should be dramatically reduced. On the other hand, previous calculations with Tb:AlN[41] show a smaller reduction in thermal conductivity. This contradicts with the thermal conductivity predicted in this work. Future efforts need to be directed to fully understand the effect of heavy rare earth dopants on the thermal conductivity of the host material. One such way would be to use density functional theory to calculate the mass defect phonon scattering rates without any free parameters. Such calculations have previously been carried out for Be-VI compounds and GeC,[125] but not yet for rare earth element dopants.

5.1.2 Light Transmission

To calculate light transmission, I assumed that the materials in the study were fully dense, and had negligibly small light absorptivities due to the typically large bandgaps. The primary loss in light energy on top of reflection is due to the scattering of light at grain boundaries caused by the birefringence effect. I used an effective medium model, where the polycrystalline material is assumed to be made up of aligned cylinders uniformly distributed in a matrix of slightly different refractive index. The key points are:

1. *Cause of light scattering*: The light scattering is due to the birefringence effect, and occurs when the crystallographical axes of the grains are misaligned, which we define here with the angle χ.

2. *Light scattering cross-section, C_{sca}*: The light scattering cross-section of each cylinder is calculated under the RGD approximation. The assumption that faceted grains can be approximated as cylinders is verified against COMSOL electromagnetic wave simulations. The scattering cross-section depends on the direction of light incidence.

3. *Extinction coefficient due to scattering, β_{sca}*: Finally, the extinction coefficient is calculated for the effective medium by multiplying C_{sca} with the number density of scatterers.
    a. At this point, it is observed that as expected, even for anisotropically shaped scatterers, β_{sca} is smaller in the direction where the grain sizes are smaller. Thus the smaller grain sizes are preferred for lasing. This is in contrast to the thermal conductivity, where the desirable high k values are achieved in the direction with larger grain sizes.
    b. In addition, it essential to minimize the refractive index contrast, $\Delta\eta$ between grains since β_{sca} scales with $\Delta\eta^2$. This is achieved by maintaining a small misalignment, χ between grains, which becomes especially important in highly birefringent materials such as AlN.

4. *Future Work*: In this thesis, the β_{sca} calculations could not be carried out for the smallest grain sizes because *dependent scattering* becomes an important consideration when the grain sizes are smaller than half the wavelength of light. In sub-section 2.6.4, we started

to address this problem, by laying out the foundation to calculate β_{sca} in such regimes. Since the dependent scattering cross-section is a strong function of the arrangement of the scattering centers, future work can focus on applying the above described techniques to realistic grain structures obtained from high resolution micrographs of the sample.

5.1.3 Figure of Merit

I finally introduced the figure of merit of Eq. (5-1), and showed that indeed there is an advantage to synthesizing polycrystalline materials with an anisotropic microstructure. When the microstructure is made up of aligned columnar grains (aspect ratio, r>1), FOM$_{c,ab}$, i.e. cooling in c-direction and lasing in ab-direction gives the highest values when the column-shaped grains have the smallest diameters and large aspect ratios (Figure 2-6 (c) and (g)). On the other hand, with disk-like grains (aspect ratio, r<1), FOM$_{ab,c}$, i.e. cooling in ab-direction and lasing in c-direction gives the highest values when the disk-shaped grains have the large diameters and small aspect ratios (Figure 2-6 (b) and (f)). With various modeling techniques, I discuss the importance of the strength of grain boundary scattering and misalignment in the chapter. This is the first time that the advantages of an anisotropic mictostructure has been proposed for high power lasing applications. The work has far-reaching potential to direct future research initiatives into using the polycrystalline forms of high thermal conductivity but birefringent materials AlN and Al$_2$O$_3$ as polycrystalline host materials for solid state lasers.

5.2 Chapter 3 - A 3 Omega Method to Measure an Arbitrary Anisotropic Thermal Conductivity Tensor

In this chapter, I implemented the electrothermal 3 omega method for anisotropic materials. While previous works have used numerical integrations to find the solution for the 3 omega heating problem on aligned anisotropic substrates, here I focused on finding a closed form analytical solution for a general case where the principal axes maybe aligned in any arbitrary direction. On top of making the data analysis easier and faster, closed form solutions have the additional advantage of offering more physical intuition. The following are the key takeaway points from this chapter.

1. *The solution to the 3 omega heating problem*: I started with solving for the time periodic temperature profile for an infinitesimally narrow line heater on top of an anisotropic substrate, by applying a series of Fourier transforms and inversions. The average heater line temperature was calculated by convolving the effect of a line heater over the width of the heater line. As is physically intuitive, the isothermal contours within the sample are stretched along the high thermal conductivity direction.

2. *Validation with COMSOL simulation*: I was able to use the coefficient form PDE module of Comsol to numerically carry out high throughput calculation of the heater line temperature in the frequency domain. This modification makes the calculation of the temperature profile in time periodic problems highly accessible. The analytical solutions developed in this chapter agreed very well with the COMSOL calculations.

3. *Demonstration with experiments on mica*: To demonstrate the method, experiments were carried out with mica, which has a moderate anisotropy. I cut mica at 30° and 60° planes to exercise an arbitrary anisotropy, so that the thermal conductivity tensor has off-diagonal terms. Two different methods are used at this point to measure the thermal conductivity tensor. In each method, to calculate the off-diagonal terms, it is essential to use 2 heater lines on two non-coplanar surfaces of the sample. In each method, the traditional slope method gives the determinant of the thermal conductivity tensor in 2D for the plane being probed. The methods are as follows:

   a. *k elements*: In this method, a *separate measurement of the volumetric heat capacity* is used to directly measure the thermal conductivity tensor elements. For aligned uniaxial substrates such as mica, where the anisotropic tensor can be represented with a diagonal matrix comprising 2 unique elements, only one heater line is required to measure the full thermal conductivity tensor. The relatively low sensitivity of this method to the cross-plane thermal conductivity necessitates precise knowledge of the temperature coefficient of resistance of the heater lines, the volumetric heat capacity, and the heater line width.

   b. *k Ratio*: This approach is differential in nature, where at least 2 heater lines are required to identify the thermal conductivity tensor elements even in the case of aligned uniaxial materials. The difference in the temperature rise detected by the 2 heater lines is related to the ratio of the thermal conductivity values cross-plane to the heater lines. The benefit of using this method is that knowledge of the volumetric heat capacity and heater line width is not required, as long as the values are expected to be constant from measurement to measurement.

A combination of the above 2 methods as described in the summary of the Chapter 3 maximizes the sensitivity and the strengths of the two schemes. In thin samples, often heater lines can only be deposited on the larger surfaces. For such samples, only the first method is applicable.

5.3 Chapter 4 - Easily accessible, low cost approaches to measure the scattering phase function of optically thin samples

In this chapter, I described cheap and easily accessible methods to measure the light scattering phase function of *geometrically* and *optically thin samples* using image resolution techniques. The methods were divided into two broad groups determined by the nature of the light source, (1) collimated and (2) diffuse. The effect of the sample on either the edge spread function (ESF) or the modulation transfer function (MTF) is used to quantify its light scattering properties. The first step to calculating the MTF or the ESF involved calculating the point spread function, PSF, which is a function of the source type, geometry and the sample's scattering properties. The salient points and advantages of the two methods are as follows:

1. *Collimated light source*: In this method, a collimated light source is used to illuminate the setup. The big advantage of the method is the relatively easy theory when compared to methods using a diffuse light source. In addition, focusing of light is not required. I looked at two different methods that use a collimated light source

   a. *ESF method*: Here the spread in the edge spread function in the presence of a scattering sample is used to calculate the scattering properties of the sample.

While this method has the advantage of having an easily obtainable edge, there are more stringent alignment requirements so that each successive ESF measurement fall right on top of each other. This decreases the number of free parameters by one, and makes it possible to directly convolve the scattering point spread function, PSF_{scatt} with the ESF for a setup with no scatterer.

b. *MTF method*: The MTF method required an additional USAF 1951 resolution target which has multiple patterns made of alternating opaque and transmitting lines. The rewards gained by the relaxed alignment requirements and the ease of data analysis makes the method attractive.

Both methods were demonstrated with experiments on an engineered diffuser which is designed as a surface scatterer with a top-hat profile. The results agreed very well with measurements taken by a goniometer setup involving specialized equipment such as a modulated laser source, a photodetector, rotation stage, and a lock-in amplifier to measure the intensity.

2. *Diffuse light source*: In this method, a more easily available diffuse light source is used for illumination purposes. Because of the diffuse nature of the light, the setup and requirements for this method are different from collimated light source techniques described above. These differences are:

a. It is now necessary to know the angle dependent emission profile of the diffuse source. This can require an additional measurement if the emission profile is not provided by the manufacturer.

b. To simplify the data analysis (i.e. for small angle scattering to be valid), the detector has to be placed far away from the scattering sample, compared to the distance between the sample and the USAF target. This makes the setup less compact.

c. Because of the large distance between the source and the detector, and the diffuse nature of the light source, an objective is required to focus the light on to a detector. It is necessary for the data analysis to know the magnification of the setup.

The PSF derived for this method was validated with numerical ray tracing techniques.

3. *Considerations and Future work*:

a. A unique feature of the above methods compared to the traditional methods involving collimated lasers, is that the measurements are sensitive to a large area of the sample. Thus, the measurements yield average scattering properties for the sample, thus eliminating the need to take multiple measurements at different spatial positions on the sample.

b. Because of the non-local nature of the measurements, the methods can have limitations due to the finite size of sources and samples, especially in the case of the collimated methods (infinite area is ideal). This can be worked around by choosing the distance between the sample and the detector screen so that most of the scattered rays are captured.

c. The methods can only measure the light transmission properties for light transmission through a large flat surface. It is not possible to measure the light

transmission through the curved circumferential surface of disk-shaped samples. This can be required for edge-pumped lasing configurations.

d. Even though the techniques involving collimated light source have been demonstrated for a surface scatterer, to evaluate lasing media, it is essential to demonstrate the technique for thin volumetric scatterers. To exercise this, well known standard scattering samples such as nearly index matched microsphere films[126] and opal glasses can be used.

References

1. Wisdom, J., Digonnet, M. & Byer, R. L. Ceramic lasers: Ready for action. *Photonics Spectra* **38,** 50–+ (2004).

2. Fan, T. Y. & Byer, R. L. Diode Laser-Pumped Solid-state Lasers. *IEEE J. Quantum Electron.* **10,** 11–17 (1988).

3. Wittrock, B. U. High-Power Nd : YAG Lasers. *Adv. Mater.* 295–297 (1990).

4. Ikesue, A. Polycrystalline Nd:YAG ceramics lasers. *Opt. Mater. (Amst).* **19,** 183–187 (2002).

5. Rutherford, T. S., Tulloch, W. M., Gustafson, E. K. & Byer, R. L. Edge-pumped quasi-three-level slab lasers: Design and power scaling. *IEEE J. Quantum Electron.* **36,** 205–219 (2000).

6. A.Giesen *et al.* Scalable Concept for diode-pumped high power solid-state lasers. *Appl. Opt. B, Phototypes Laser Chem* **58,** 365 (1994).

7. Sanghera, J. *et al.* Ceramic laser materials. *Materials (Basel).* **5,** 258–277 (2012).

8. Akiyama, J., Sato, Y. & Taira, T. Laser demonstration of diode-pumped Nd3+-doped fluorapatite anisotropic ceramics. *Appl. Phys. Express* **4,** (2011).

9. Volodchenkov, A. D. *et al.* Magnetic and thermal transport properties of SrFe12O19 permanent magnets with anisotropic grain structure. *Mater. Des.* **125,** 62–68 (2017).

10. Touloukian, Y. S., Powell, R. W., Ho, C. Y. & Klemens, P. G. Thermophysical Properties of Matter - The TPRC Data Series. Volume 2. Thermal Conductivity - Nonmetallic Solids. (1971).

11. Slack, G. a., Tanzilli, R. a., Pohl, R. O. & Vandersande, J. W. The intrinsic thermal conductivity of AlN. *J. Phys. Chem. Solids* **48,** 641–647 (1987).

12. Wieg, A. T. *et al.* Visible photoluminescence in polycrystalline terbium doped aluminum nitride (Tb:AlN) ceramics with high thermal conductivity. *Appl. Phys. Lett.* **101,** 148–156 (2012).

13. Jiang, L. *et al.* Observation of stimulated emission from a single Fe-doped AlN triangular fiber at room temperature. *Sci. Rep.* **5,** 17979 (2015).

14. Maqbool, M., Main, K. & Kordesch, M. AlN infrared whispering gallery mode microlaser on optical fibers. *Opt. Lett.* **35,** 3637–3639 (2010).

15. Sibbett, W., Lagatsky, A. A. & Brown, C. T. A. The development and application of femtosecond laser systems. *Opt. Express* **20,** 6989 (2012).

16. Malinauskas, M. *et al.* Ultrafast laser processing of materials: from science to industry. *Light Sci. Appl.* **5,** e16133 (2016).

17. Penilla, E. H., Kodera, Y. & Garay, J. E. Blue-green emission in terbium-doped alumina (Tb:Al2O 3) transparent ceramics. *Adv. Funct. Mater.* **23,** 6036–6043 (2013).

18. Wieg, A. T., Grossnickle, M. J., Kodera, Y., Gabor, N. M. & Garay, J. E. Nd:AlN polycrystalline ceramics: A candidate media for tunable, high energy, near IR lasers. *Appl. Phys. Lett.* **109,** 121901 (2016).

19. Wang, Z., Alaniz, J. E., Jang, W., Garay, J. E. & Dames, C. Thermal conductivity of nanocrystalline

silicon: Importance of grain size and frequency-dependent mean free paths. *Nano Lett.* **11,** 2206–2213 (2011).

20. Apetz, R. & van Bruggen, M. P. B. Transparent Alumina: A Light-Scattering Model. *J. Am. Ceram. Soc.* **86,** 480–486 (2003).

21. Onsager, L. Reciprocal relations in irreversible processes. I. *Phys. Rev.* **37,** (1931).

22. Cahill, D. G. Thermal conductivity measurement from 30 to 750 K: the 3ω method. *Rev. Sci. Instrum.* **61,** 802 (1990).

23. Cahill, D. G. Analysis of heat flow in layered structures for time-domain thermoreflectance. *Rev. Sci. Instrum.* **75,** 5119–5122 (2004).

24. Dames, C. Measuring the thermal conductivity of thin films: 3 omega and related electrothermal methods. *Annu. Rev. Heat Transf.* 7–49 (2013). doi:10.1615/AnnualRevHeatTransfer.v16.20

25. Feser, J. P., Liu, J. & Cahill, D. G. Pump-probe measurements of the thermal conductivity tensor for materials lacking in-plane symmetry. *Rev. Sci. Instrum.* **85,** 104903 (2014).

26. Borca-Tasciuc, T., Kumar, a. R. & Chen, G. Data reduction in 3ω method for thin-film thermal conductivity determination. *Rev. Sci. Instrum.* **72,** 2139 (2001).

27. Tong, T. & Majumdar, A. Reexamining the 3-omega technique for thin film thermal characterization. *Rev. Sci. Instrum.* **77,** 104902 (2006).

28. Ramu, A. T. & Bowers, J. E. Analysis of the ' 3-Omega ' method for substrates and thick films of anisotropic thermal conductivity. **43516,** 1–8 (2012).

29. Duncan, D. D., Lange, C. H. & Fischer, D. G. Imaging Performance of Crystalline and Polycrystalline Oxides. *APL Tech. Dig.* **14,** (1993).

30. Bowman, S. R. High-power diode-pumped solid-state lasers. *Opt. Eng.* **52,** 21012 (2012).

31. Ikesue, A., Kinoshita, T., Kamata, K. & Yoshida, K. Fabrication and Optical Properties of High-Performance Polycrystalline Nd:YAG Ceramics for Solid-State Lasers. *Journal of the American Ceramic Society* **78,** 1033–1040 (1995).

32. Yagi, T. *et al.* Thermal rollover around 460 mW observation in single-lateral mode 780 nm laser diodes with window-mirror structure. *Japanese J. Appl. Physics, Part 1 Regul. Pap. Short Notes Rev. Pap.* **42,** 2316–2319 (2003).

33. Kim, D.-L. & Kim, B.-T. Fracture characteristics of ceramic Nd:YAG. *Opt. Express* **22,** 11331–11339 (2014).

34. Schulz, P.A., Henion & S.R. Liquid-nitrogen-cooled Ti:Al2O3 laser. *Quantum Electron. IEEE J.* **27,** 1039–1047 (1991).

35. Klein, P. H. & Croft, W. J. Thermal conductivity, diffusivity, and expansion of Y2O 3, Y3 Al5O12, and LaF3 in the range 77??-300??K. *J. Appl. Phys.* **38,** 1603–1607 (1967).

36. Slack, G. A. Nonmetallic crystals with high thermal conductivity. *J. Phys. Chem. Solids* **34,** 321–335 (1973).

37. Slack, G. A., Tanzilli, R. A., Pohl, R. O. & Vandersande, J. W. The intrinsic thermal conductivity of AlN. *J. Phys. Chem. Solids* **48,** 641–647 (1987).

38. Touloukian, Y. S. S., Powell, R. W., Ho, C. Y. & Klemens, P. G. Thermophysical Properties of Matter: Thermal conductivity : nonmetallic solids. 770 (1970).

39. Wieg, A. T. *et al.* Visible photoluminescence in polycrystalline terbium doped aluminum nitride (Tb:AlN) ceramics with high thermal conductivity. *Appl. Phys. Lett.* **101,** 1–2 (2012).

40. Wang, Z., Alaniz, J. E., Jang, W., Garay, J. E. & Dames, C. Thermal Conductivity of Nanocrystalline Silicon: Importance of Grain Size and Frequency-Dependent Mean Free Paths. *Nano Lett.* null-null (2011). doi:10.1021/nl1045395

41. Wieg, A. T., Kodera, Y., Wang, Z., Dames, C. & Garay, J. E. Thermomechanical properties of rare-earth-doped AlN for laser gain media: The role of grain boundaries and grain size. *Acta Mater.* **86,** 148–156 (2015).

42. Roskovcova, L., Pastrnak, J. & Babuskova, R. The Dispersion of the Refractive Index and the Birefringence of AlN. *Phys. Status Solidi* **20,** 29–31 (1967).

43. Jiji, L. M. *Heat conduction: Third edition*. *Heat Conduction (Third Edition)* (Springer Berlin Heidelberg, 2009). doi:10.1007/978-3-642-01267-9

44. Schelling, P. K., Phillpot, S. R. & Keblinski, P. Kapitza conductance and phonon scattering at grain boundaries by simulation. *J. Appl. Phys.* **95,** 6082–6091 (2004).

45. Sun, L. & Murthy, J. Y. Molecular Dynamics Simulation of Phonon Scattering at Silicon/Germanium Interfaces. *J. Heat Transfer* **132,** 102403 (2010).

46. Zhao, H. & Freund, J. B. Phonon scattering at a rough interface between two fcc lattices. *J. Appl. Phys.* **105,** 13515 (2009).

47. Hua, C. & Minnich, A. J. Importance of frequency-dependent grain boundary scattering in nanocrystalline silicon and silicon-germanium thermoelectrics. 1–17 (2014).

48. Yang, L. & Minnich, A. J. Thermal transport in nanocrystalline Si and SiGe by ab initio based Monte Carlo simulation. *Sci. Rep.* **7,** 44254 (2017).

49. Lee, J. *et al.* Investigation of phonon coherence and backscattering using silicon nanomeshes. *Nat. Commun.* **8,** 14054 (2017).

50. McCurdy, A. K., Maris, H. J. & Elbaum, C. Anisotropic heat conduction in cubic crystals in the boundary scattering regime. *Phys. Rev. B* **2,** 4077–4083 (1970).

51. Ziman, J. M. *Electrons and Phonons*. (1960).

52. Moore, A. L., Saha, S. K., Prasher, R. S. & Shi, L. Phonon backscattering and thermal conductivity suppression in sawtooth nanowires. *Appl. Phys. Lett.* **93,** 1–3 (2008).

53. Hori, T., Shiomi, J. & Dames, C. Effective phonon mean free path in polycrystalline nanostructures. *Appl. Phys. Lett.* **106,** 171901 (2015).

54. Chen, G. Nanoscale Energy Transport and Conversion. *Heat Mass Transf.* 531 (2005).

55. Heron, J. S., Bera, C., Fournier, T., Mingo, N. & Bourgeois, O. Blocking phonons via nanoscale geometrical design. *Phys. Rev. B - Condens. Matter Mater. Phys.* **82,** 1–5 (2010).

56. Klemens, P. G. The Scattering of Low-Frequency Lattice Waves by Static Imperfections. *Proc. Phys. Soc. Sect. A* **68,** 1113–1128 (1955).

57. Abeles, B. Lattice thermal conductivity of disordered semiconductor alloys at high temperatures. *Phys. Rev.* **131,** 1906–1911 (1963).

58. Slack, G. A. Effect of isotopes on low-temperature thermal conductivity. *Phys. Rev.* **105,** 829–831 (1957).

59. Koechner, W. *Solid-State Laser Engineering*. (Springer Science+Bysiness Media, Inc., 2006). doi:10.1007/s13398-014-0173-7.2

60. Sato, Y., Akiyama, J. & Taira, T. Orientation control of micro-domains in anisotropic laser ceramics. *Opt. Mater. Express* **3,** 829 (2013).

61. Pavlin, J., Vaupotic, N. & Cepic, M. Direction dependency of extraordinary refraction index in uniaxial nematic liquid crystals. 1–20 (2012). doi:10.1088/0143-0807/34/2/331

62. van de Hulst, H. C. *Light Scattering by Small Particles*. (Dover Publications, Inc., 1981).

63. Yushanov, S., Crompton, J. & Koppenhoefer, K. Mie Scattering of Electromagnetic Waves. in *COMSOL Conference* (2013).

64. Drolen, B. L. & Tien, C. L. Independent and dependent scattering in packed-sphere systems. *J. Thermophys. Heat Transf.* **1,** 63–68 (1987).

65. Modest, M. F. *Radiative Heat Transfer*. (Elsevier Inc., 2013).

66. Siegel, R. & Howell, J. *Thermal Radiation Heat Transfer*. (Taylor & Francis Group, 2002).

67. Barber, P. W. & Wang, D.-S. Rayleigh-Gans-Debye applicability to scattering by nonspherical particles. *Appl. Opt.* **17,** 797 (1978).

68. Silfvast, W. T. *Laser Fundamentals*. *Cambridge University Press* (Cambridge University Press, 2004).

69. U, J. L. *et al.* High-Power Nd:Y3Al5O12 Ceramic Laser. *Appl. Phys.* **39,** 1048–1050 (2000).

70. Ashoori, V., Shayganmanesh, M. & Radmard, S. Heat Generation and Removal in Solid State Lasers. (2012). doi:10.5772/62102

71. Brown, D. C. & Hoffman, H. J. Thermal, stress, and thermo-optic effects in high average power double-clad silica fiber lasers. *IEEE J. Quantum Electron.* **37,** 207–217 (2001).

72. Koechner, W. Thermal Lensing in a Nd:YAG Laser Rod. *Appl. Opt.* **9,** 2548–53 (1970).

73. Clarkson, W. A. Thermal effects and their mitigation in end-pumped solid-state lasers. *J. Phys. D. Appl. Phys.* **34,** 2381 (2001).

74. Kim, D. L. & Kim, B. T. Laser output power losses in ceramic Nd:YAG lasers due to thermal effects. *Optik (Stuttg).* **127,** 9738–9742 (2016).

75. Ashoori, V., Shayganmanesh, M. & Radmar, S. in *An Overview of Heat Transfer Phenomena* (InTech, 2012). doi:10.5772/52381

76. Yang, F. & Dames, C. Heating-frequency-dependent thermal conductivity: An analytical solution from diffusive to ballistic regime and its relevance to phonon scattering measurements. *Phys. Rev. B* **91,** 1–14 (2015).

77. Mingo, N., Yang, L., Li, D. & Majumdar, A. Predicting the Thermal Conductivity of Si and Ge

Nanowires. *Nano Lett.* **3,** 1713–1716 (2003).

78. Dames, C. & Chen, G. Theoretical phonon thermal conductivity of Si/Ge superlattice nanowires. *J. Appl. Phys.* **95,** 682–693 (2004).

79. Schober, H., Strauch, D. & Dorner, B. Lattice dynamics of sapphire (A1203). *Z. Phys. B* **283,** 273–283 (1993).

80. Kai-Ming, Z. & Xi-de, X. Lattice Dynamics of Wurtzite Semiconductors GaN and AlN. *Acta Phys. Sin.* **8,** 841 (1998).

81. Siegel, R. & Howell, J. *Thermal Radiation Heat Transfer*. (Taylor & Francis Group, 2001).

82. Prasher, R. Thermal transport due to phonons in random nano-particulate media in the multiple and dependent (correlated) elastic scattering regime. *J. Heat Transfer* **128,** 627–637 (2006).

83. Mishra, V., Hardin, C. L., Garay, J. E. & Dames, C. A 3 omega method to measure an arbitrary anisotropic thermal conductivity tensor. *Rev. Sci. Instrum.* **86,** 54902 (2015).

84. Carle, M., Pierrat, P., Lahalle-Gravier, C., Scherrer, S. & Scherrer, H. Transport properties of n-type Bi2(Te1–xSex)3 single crystal solid solutions (x $\leqslant$ 0.05). *J. Phys. Chem. Solids* **56,** 201–209 (1995).

85. Yan, X. *et al.* Experimental studies on anisotropic thermoelectric properties and structures of n-type Bi2Te2.7Se0.3. *Nano Lett.* **10,** 3373–8 (2010).

86. Zhao, L.-D. *et al.* Ultralow thermal conductivity and high thermoelectric figure of merit in SnSe crystals. *Nature* **508,** 373–7 (2014).

87. Morelli, D. *et al.* Anisotropic thermal conductivity of superconducting lanthanum cuprate. *Phys. Rev. B* **41,** 2520–2523 (1990).

88. Shen, S., Henry, A., Tong, J., Zheng, R. & Chen, G. Polyethylene nanofibres with very high thermal conductivities. *Nat. Nanotechnol.* **5,** 251–5 (2010).

89. Glotzer, S. C. & Solomon, M. J. Anisotropy of building blocks and their assembly into complex structures. *Nat. Mater.* **6,** 557–62 (2007).

90. Gaillard, Y., Rico, V. J., Jimenez-Pique, E. & González-Elipe, A. R. Nanoindentation of TiO 2 thin films with different microstructures. *J. Phys. D. Appl. Phys.* **42,** 145305 (2009).

91. Robbie, K. Sculptured thin films and glancing angle deposition: Growth mechanics and applications. *J. Vac. Sci. Technol. A Vacuum, Surfaces, Film.* **15,** 1460 (1997).

92. Janning, J. L. Thin film surface orientation for liquid crystals. *Appl. Phys. Lett.* **21,** 173 (1972).

93. Dames, C. & Chen, G. 1Ω, 2Ω, and 3Ω Methods for Measurements of Thermal Properties. *Rev. Sci. Instrum.* **76,** 124902 (2005).

94. Cahill, D., Katiyar, M. & Abelson, J. Thermal conductivity of a-Si:H thin films. *Phys. Rev. B* **50,** 6077–6081 (1994).

95. Kim, J. H., Feldman, A. & Novotny, D. Application of the three omega thermal conductivity measurement method to a film on a substrate of finite thickness. *J. Appl. Phys.* **86,** 3959 (1999).

96. Feldman, A. Algorithm for solutions of the thermal diffusion equation in a stratified medium with a modulated heating source. *High Temp. - High Press.* **31,** 293–296 (1999).

97. Kim, J. H., Feldman, A. & Novotny, D. Application of the three omega thermal conductivity measurement method to a film on a substrate of finite thickness. *J. Appl. Phys.* **86,** 3959 (1999).

98. Tong, T. & Majumdar, A. Reexamining the 3-omega technique for thin film thermal characterization. *Rev. Sci. Instrum.* **77,** 104902 (2006).

99. Ramu, A. T. & Bowers, J. E. Analysis of the '3-Omega' method for substrates and thick films of anisotropic thermal conductivity. *J. Appl. Phys.* **112,** 43516 (2012).

100. Ramu, A. T. & Bowers, J. E. A '2-omega' technique for measuring anisotropy of thermal conductivity. *Rev. Sci. Instrum.* **83,** 124903 (2012).

101. Newnham, R. E. *Properties of Materials: Anisotropy, Symmetry, Structure*. (Oxford University Press Inc., New York, 2005).

102. Carslaw, H. S. & Jaeger, J. C. *Conduction of Heat in SOlids*. (Oxford University Press, 1959).

103. Hahn, D. W. & Özişik, M. N. Heat Conduction, Third Edition. *John Wiley & Sons, Inc.* 614 (2012).

104. Duquesne, J.-Y., Fournier, D. & Fretigny, C. Analytical solutions of the heat diffusion equation for 3 omega method geometry. *J. Appl. Phys.* **108,** 86103–86104 (2010).

105. Milton, A. & Stegun, I. A. *Handbook of Mathematical Functions with Formulas, Graphs, and Mathematical Tables*. (Dover Publications, Inc., 1970).

106. *The Meijer-G function can be evaluated in Matlab using the meijerG function in the Mupad Notebook Interface*.

107. Gray, A. S. & Uher, C. Thermal conductivity of mica at low temperatures. *J. Mater. Sci.* **12,** 959–965 (1977).

108. Cermark, V. & Rybach, L. in *Physical Properties of Rocks* (ed. Angenheister, G.) 314 (Springer-Verlag GmbH, 1982). doi:10.1007/10201894_62

109. Newnham, R. E. Elastic Anisotropy in Minerals. *Mineral. Mag.* **39,** 78–84 (1973).

110. Vaughan, M. T. & Guggenheim, S. Elasticity of muscovite and its relationship to crystal structure. *J. Geophys. Res.* **91,** 4657 (1986).

111. Cholach, P. Y. & Schmitt, D. R. Intrinsic elasticity of a textured transversely isotropic muscovite aggregate: Comparisons to the seismic anisotrophy of schists and shales. *J. Geophys. Res. Solid Earth* **111,** 1–18 (2006).

112. Faust, J. & Knittle, E. The equation of state, amorphization, and high-pressure phase diagram of muscovite. *J. Geophys. Res.* **99,** 19785 (1994).

113. Krupka, K. M., Robie, R. A. & Hemingway, B. S. High-temperature heat capacities of corundum, periclase, anortite, CaAl2Si2O8 glass, muscovite, prophyllite, KalSi3O8 glass, grossular, and NaAlSi3O8 glass. *Am. Mineral.* **64,** 86–101 (1979).

114. Hsieh, W.-P., Chen, B., Li, J., Keblinski, P. & Cahill, D. G. Pressure tuning of the thermal conductivity of the layered muscovite crystal. *Phys. Rev. B* **80,** 180302 (2009).

115. Gundrum, B., Cahill, D. & Averback, R. Thermal conductance of metal-metal interfaces. *Phys. Rev. B* **72,** 245426 (2005).

116. Nye, J. F. *Physical Properties of Crystals Their representations by tensors and Matrices*. (Oxford

University Press, 1985).

117. Benke, K. K. & Mckellar, B. H. J. Modulation transfer function of photographic emulsion: the small-angle approximation in radiative transport theory. **29,** 151–156 (1990).

118. Hou, W., Lee, Z. & Weidemann, A. D. Why does the Secchi disk disappear? An imaging perspective. *Opt. Express* **15,** 2791–802 (2007).

119. Coppel, L. G., Neuman, M. & Edström, P. Lateral light scattering in paper - MTF simulation and measurement. *Opt. Express* **19,** 25181–25187 (2011).

120. Hou, W., Weidemann, A. D., Gray, D. J. & Fournier, G. R. Imagery-derived modulation transfer function and its applications for underwater imaging. *Proc. SPIE, Appl. Digit. Image Process.* **6696,** 669622-669622–8 (2007).

121. Cooper, V. N., Boone, J. M., Seibert, J. a & Pellot-Barakat, C. J. An edge spread technique for measurement of the scatter-to-primary ratio in mammography. *Med. Phys.* **27,** 845–853 (2000).

122. Boone, J. M. & Cooper, V. N. Scatter/primary in mammography: Monte Carlo validation. *Med. Phys.* **27,** 1818–31 (2000).

123. Salvagnini, E., Bosmans, H., Struelens, L. & Marshall, N. W. Quantification of scattered radiation in projection mammography: Four practical methods compared. *Med. Phys.* **39,** 3167 (2012).

124. Landry, E. S. & McGaughey, A. J. H. Thermal boundary resistance predictions from molecular dynamics simulations and theoretical calculations. *Phys. Rev. B - Condens. Matter Mater. Phys.* **80,** 1–11 (2009).

125. Lindsay, L., Broido, D. a & Reinecke, T. L. Phonon-isotope scattering and thermal conductivity in materials with a large isotope effect: A first-principles study. *Phys. Rev. B* **88,** 144306 (2013).

126. Oberdisse, J. *et al.* Structure of Latex-Silica Nanocomposite Films : A Small Angle Neutron Scattering Study To cite this version : HAL Id : hal-00003641 Structure of Latex-Silica Nanocomposite Films : A Small Angle Neutron. *Am. Chem. Soc.* **35,** 4397 (2002).